



UNIVERSIDAD
DE GRANADA

Ultra-fast time-resolved spectroscopy of lightning-like discharges with

GALIUS

Thi Ny Kieu



Science and Innovation With Thunderstorms



INSTITUTO DE
ASTROFÍSICA DE
ANDALUCÍA



EXCELENCIA
SEVERO
OCHOA



H2020 Marie Skłodowska-Curie Initial Training Network

Ultra-fast time-resolved spectroscopy of lightning-like discharges with GALIUS



Universidad de Granada

THI NY KIEU

Departamento de Sistema Solar

Instituto de Astrofísica de Andalucía

Programa de Doctorado en Física y Ciencias del Espacio

A thesis submitted for the degree of

Philosophiæ Doctor (PhD)

September 2021

Examination date:

Thesis supervisors:

Dr. Francisco J. Gordillo Vázquez

Dr. Alejandro Luque Estepa

©Thi Ny Kieu

Cover design: Thi Ny Kieu

Cover picture: Cloud-to-cloud and cloud-to-ground lightning,

Oscar Van der Velde, taken on May 16th, 2020

1. Reviewer:

2. Reviewer:

Day of the defense:

Signature from the head of the PhD committee:

This thesis is presented with the following structure

The contents required in a doctoral thesis at the University of Granada for doctoral programs regulated by RD99/2021 are found in this report structured in the following sections:

Title (Cover page)

Abstract

Resumen

Acknowledgements

Introduction

Chapter 1

Objective

Chapter 2

Methodology

Chapter 3

Results

Chapter 4: 1st publication

Chapter 5: 2nd publication

Chapter 6: 3rd publication

Conclusions

Chapter 7

Bibliography

List of publications

The research reported in this thesis has resulted in the following articles:

1. **Kieu, T.N.**, Gordillo-Vázquez, F.J., Passas, M., Sánchez, J., Pérez-Invernón, **2021**. ‘High-speed spectroscopy of lightning-like discharges: evidence of molecular optical emissions’. *Journal of Geophysical Research: Atmospheres*.
2. **Kieu, T. N.**, Gordillo-Vázquez, F.J., Passas, M., Sánchez, J., Pérez-Invernón, F.J., Luque, A., Montanyá, J. and Christian, H., **2020**. ‘Submicrosecond spectroscopy of lightning-like discharges: Exploring new time regimes’. *Geophysical Research Letters*, 47(15), p.e2020GL088755
3. Passas, M., Sánchez, J., **Kieu, T.N.**, Sánchez-Blanco, E. and Gordillo-Vázquez, F.J., **2019**. ‘GALIUS: an ultrafast imaging spectrograph for the study of lightning’. *Applied Optics*, 58(29), pp.8002-8006.

El doctorando / The *doctoral candidate* [**Thi Ny Kieu**] y los directores de la tesis / and the thesis supervisor/s: [**Dr. Francisco J. Gordillo Vazquez and Dr. Alejandro Luque Estepa**]

Garantizamos, al firmar esta tesis doctoral, que el trabajo ha sido realizado por el doctorando bajo la dirección de los directores de la tesis y hasta donde nuestro conocimiento alcanza, en la realización del trabajo, se han respetado los derechos de otros autores a ser citados, cuando se han utilizado sus resultados o publicaciones.

/

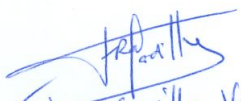
Guarantee, by signing this doctoral thesis, that the work has been done by the doctoral candidate under the direction of the thesis supervisor/s and, as far as our knowledge reaches, in the performance of the work, the rights of other authors to be cited (when their results or publications have been used) have been respected.


Lugar y fecha / Place and date:


31st July 2021

Director/es de la Tesis / *Thesis supervisor/s*;

Doctorando / *Doctoral candidate*:


Francisco J. Gordillo Vazquez


Thi Ny Kieu


Alejandro Luque Estepa

Firma / Signed

Firma / Signed

Abstract

On 17th August 1961, the first time-resolved spectra of an individual lightning flash was obtained (Salanave, 1961). This opened a new era of time-resolved lightning spectroscopy. A few years later, Orville (1968a,b,c,d) recorded the first time-resolved spectra of individual lightning strokes between the cloud and the ground with a time resolution of $5 \mu\text{s}$ (a lightning flash is formed by several strokes). These spectra showed the dynamics of temperature and electron density up to $50 \mu\text{s}$. Recently, doubly ionized nitrogen were first found in spectra of triggered lightning return strokes with time resolution of $1.5 \mu\text{s}$ (Walker and Christian, 2017, 2019). Quantifications from these spectra also revealed high temperatures up to 40000 K and high electron densities up to 10^{19} cm^{-3} . These high values could be explained by the short exposure time ($1.44 \mu\text{s}$) of the instrument and its ability to record in the early time of the discharges. This moves us to explore lightning spectra within even shorter timescale and higher recording speeds. In this thesis, we will present *a study on time-resolved spectroscopy at micro and sub-microsecond timescales of lightning-like discharges* with a new instrument developed in our group at IAA-CSIC, named GALIUS.

GALIUS - **Gr**Anada **L**ightning **U**ltrafast **S**pectrograph - is a portable, ground-based spectrograph intended to carry out spectral analysis of natural lightning or artificial lightning. GALIUS can record spectra up to 2.1 million frame-per-second

(Mfps), from the near-ultraviolet to the near-infrared thanks to four interchangeable gratings - a grating is a combination of a prism and a grating arranged in such a way that light at a chosen central wavelength passes straight through. Each grating is customized and designed to record spectra at certain spectral ranges with different speeds: grating R1 allows to record spectra in the near ultraviolet-blue (380 - 450 nm) at 672000 fps; grating R2 allows recording at the same speed but in the visible-near infrared (475 - 795 nm); grating R3 allows images at 2.1 Mfps in a short visible region (645 - 665 nm), centered in the H_α line (656.5 nm). Finally, grating R4 allows to record spectra within the near-infrared (770 - 805 nm) at 1.4 Mfps. Details of the configurations and characteristics of each grating were described in the article published in *Applied Optics* with title “*GALIUS: an ultrafast imaging spectrograph for the study of lightning*” (Passas et al., 2019).

In total, GALIUS has 22 configurations which we designed for the different experimental setups both in the laboratory and in the field. Initially, GALIUS was tested with small (4 cm) sparks generated by an electrostatic generator at IAA-CSIC, Granada. After that, GALIUS was moved to Tarrasa (Barcelona) to work with relatively long (1 m) electrical discharges produced by a 2.0 MV Marx generator in the Switching and Lightning modes operated at 800 kV. Spectra of these sparks were carefully analyzed to identify optical signatures of chemical species and to quantify key magnitudes (temperature, electron density, electrical conductivity ...). Results of these studies will be presented in different chapters of the thesis corresponding to each of the papers published.

Our first results are about the analysis of optical emission spectra from lightning-like electrical discharges recorded at 2.1 Mfps with grating R3. These are the first time-resolved spectra obtained with high-speed framing cameras at *sub-microsecond* timescales. Quantifications from these spectra revealed evidences of

non-LTE conditions right behind the shock front in posttrigger sub-microsecond times. We published these results in a paper in *Geophysical Research Letters* with title “*Sub-microsecond Spectroscopy of Lightning-Like Discharges: Exploring New Time Regimes*” (Kieu et al., 2020).

At lower recording speeds, GALIUS was capable of filming lightning-like discharges from the near ultraviolet-blue to the near-infrared with gratings R1, R2, R4. We found evidences of molecular optical emissions from CO, CN, C₂, N₂, and N₂⁺. This finding may open the door to identify and quantify lightning NO production by using high-speed optical emission spectroscopy. From the emissions of different spectral lines, electron concentrations and gas temperatures were estimated by different methods and compared with each other. These results were published in a paper in *Journal of Geophysical Research Atmospheres* with title “*High-speed spectroscopy lightning-like discharges: evidence of molecular optical emissions*” (Kieu et al., 2021).

Resumen

El 17 de agosto de 1961 se obtuvieron los primeros espectros de emisión óptica resueltos en tiempo de un destello o ‘flash’ individual de un rayo (Salanave, 1961). Este hecho fue el punto de inicio de una nueva era en la investigación sobre rayos mediante técnicas de espectroscopía óptica de emisión resuelta en tiempo. Unos pocos años después, en 1968, Orville (1968a,b,c,d) logró captar los primeros espectros resueltos en tiempo (con $5 \mu\text{s}$ de resolución temporal) de “*strokes*” individuales de rayos nube-suelo (cada destello o “*flash*” de un rayo está formado por varios “*strokes*” separados entre sí por entre algunas decenas y algunos centenares de milisegundos). Estos espectros permitieron acceder por primera vez a la dinámica temporal de la temperatura y de la densidad electrónica en un punto del canal de un “*stroke*” de un rayo durante los primeros $50 \mu\text{s}$ de su propagación.

Más recientemente, en 2017 y 2019, se logró identificar por primera vez la presencia de especies doblemente ionizadas en espectros ópticos de rayos producidos de manera artificial (Walker and Christian, 2017, 2019). El análisis de los espectros ópticos de rayos artificiales reveló valores de hasta 40000 K para la temperatura y de hasta 10^{19} cm^{-3} para la densidad electrónica. La obtención de valores tan elevados se explica por los muy cortos tiempos de exposición ($1.44 \mu\text{s}$) del instrumento utilizado, lo cual hace posible el acceso a las primeros instantes de la descarga eléctrica.

Los descubrimientos arriba comentados son una fuerte motivación para seguir explorando y analizando las emisiones ópticas de rayos. En esta tesis presento resultados pormenorizados de investigaciones llevadas a cabo con espectroscopía de emisión óptica resuelta en tiempo de descarga eléctricas tipo rayo en escalas de tiempo poco o nada exploradas (rango del microsegundo y por debajo del microsegundo). Estos estudios han sido realizados con el instrumento *GrAnada LIghtning Ultrafast Spectrograph* (GALIUS) recientemente desarrollado en nuestro grupo de electricidad atmosférica del Instituto de Astrofísica de Andalucía (IAA - CSIC).

GALIUS es un espectrógrafo portátil desarrollado con el fin de poder llevar a cabo campañas de espectroscopía de emisión óptica ultrarrápida de rayos naturales y artificiales así como de descargas tipo rayo en el laboratorio. GALIUS dispone de una cámara capaz de grabar a una velocidad de hasta 2.1 millones de imágenes por segundo (2.1 Mfps) con altísima sensibilidad óptica entre el ultravioleta cercano (380 nm) y el infrarrojo cercano (795 nm). El acceso por trozos a este amplio rango espectral es posible gracias a cuatro “*grismas*” (elemento óptico resultante de la combinación de una red de difracción encapsulada entre dos prismas). Cada “*grisma*” se ha diseñado y fabricado expresamente con las características necesarias para GALIUS. El “*grisma*” R1 permite obtener espectros en el rango ultravioleta cercano-azul (380 nm - 450 nm) a 672000 imágenes por segundos (fps); el “*grisma*” R2 permite grabar a la misma velocidad que el R1 pero en el rango visible-infrarrojo cercano (475 nm - 795 nm); el “*grisma*” R3 permite grabaciones a 2.1 Mfps en un rango espectral estrecho (645 nm - 665 nm) centrado en la línea H_{α} (656.5 nm). Finalmente, el “*grisma*” R4 permite disponer de espectros en el rango infrarrojo cercano (770 - 805 nm) obtenidos a 1.4 Mfps. Los detalles de las diferentes configuraciones de GALIUS así como de

las características ópticas de cada “*grisma*” se incluyen en un artículo de título “*GALIUS: an ultrafast imaging spectrograph for the study of lightning*” publicado en la revista *Applied Optics* (Passas et al., 2019), con N. Kieu como tercera autora.

GALIUS dispone de un total de 22 configuraciones ópticas que han sido diseñadas teniendo en cuenta los diferentes escenarios de trabajo esperables tanto en el laboratorio como en campo. GALIUS fue inicialmente probado y calibrado usando pequeños (4 cm) arcos eléctricos producidos por un generador electrostático disponible en el laboratorio de electricidad atmosférica del IAA-CSIC en Granada. Posteriormente GALIUS fue trasladado a Tarrasa (Barcelona) para realizar experimentos con arcos eléctricos de aproximadamente 1 metro de longitud producidos con un generador eléctrico tipo Marx (capaz de producir hasta 2 MV) usado en modo interruptor (“*Switching*”) y en modo rayo (“*Lightning*”) con voltajes pico de 800 kV. Los espectros de emisión ópticas de todas estas descargas fueron cuidadosamente analizados con el fin de: (1) identificar líneas y bandas espectrales típicas de diferentes especies químicas y de (2) cuantificar, a partir de los espectros obtenidos, magnitudes importantes como la temperatura, densidad electrónica, conductividad eléctrica, etc en la descarga. Los resultados de estos análisis e investigaciones se presentan en varios capítulos de la tesis, correspondiendo cada capítulo a los tres trabajos publicados en el transcurso de la tesis doctoral.

Los primeros resultados de la tesis provienen del análisis de los espectros ópticos resueltos en tiempo de descargas eléctricas tipo rayo obtenido a 2.1 Mfps con el “*grisma*” R3. Hasta la fecha son los primeros y únicos espectros de descargas eléctricas tipo rayo obtenidos con un espectrógrafo de imagen con resolución temporal inferior al microsegundo (y con tiempos de exposición de 160 nanosegundos). Los análisis de los espectros sugieren un posible alejamiento de las condi-

ciones de equilibrio termodinámico local (LTE) justo detrás del frente de propagación de la onda de choque asociada a la expansión del canal de la descarga en los instantes inmediatamente posteriores al comienzo de la misma y en una escala de tiempo inferior al microsegundo. Estos resultados se incluyen en un artículo de título “*Sub-microsecond Spectroscopy of Lightning-Like Discharges: Exploring New Time Regimes*” publicado en la revista de alto impacto *Geophysical Research Letters* (Kieu et al., 2020).

Al usar GALIUS con velocidades de grabación inferior a los 2.1 Mfps hemos podido disponer también de espectros ópticos desde el rango ultravioleta cercano hasta el infrarrojo cercano usando los “*grismas*” R1, R2 y R4. En este estudio se han encontrado evidencias de emisiones ópticas moleculares asociadas a las especies CO, CN, C₂, N₂ y N₂⁺, algunas de las cuales (CO y C₂) se han detectado por primera vez en el canal de descargas eléctricas tipo rayo. Estos hallazgos hacen pensar en la posibilidad futura de detectar, en el rango espectral entre 140 nm y 340 nm, emisiones ópticas asociadas al óxido de nitrógeno (NO) producido por los rayos y descargas tipo rayo (GALIUS sólo es sensible hasta los 380 nm). A partir del análisis de diferentes líneas espectrales se han cuantificado por diferentes métodos (que se han comparado entre sí) temperaturas y concentración de electrones en el canal de las descargas tipo rayo investigadas. Estos resultados se incluyen en un artículo de título “*High-speed spectroscopy of lightning-like discharges: evidence of molecular optical emissions*” publicado en la revista de alto impacto *Journal of Geophysical Research - Atmospheres* (Kieu et al., 2021).

Acknowledgements

For the long journey I have been going through, the thesis would have not been finished without the support of many people around me.

First of all, I would like to thank my supervisors Dr. Francisco J. Gordillo Vázquez and Dr. Alejandro Luque Estepa for giving me a great opportunity to work on this project. Thank you very much for your time, your patience, and your immense knowledge during these years. I also want to express my thanks to Dr. María Passas and Justo Sánchez, my two closest colleagues, for their invaluable help and constant support. Such a great pleasure to work with you guys.

Secondly, I would like to express my deepest gratefulness to my family, especially my mother, who can't read these words but her life has always been an inspiration for me. She is the greatest woman in my world. Thank you for your unconditional love, your encouragement, and for being there whenever I am in trouble.

I also want to thank my colleagues in the TRAPPA group: Dongshuai, Alejandro, Sergio, Anthony. We had so much fun together during many trips for conferences, schools and sharing the same office. I especially want to thank Dr. Francisco Javier Pérez Invernón and Miguel Gomes for your constant support to help me with computer problems and paperworks at the beginning of my thesis.

It is very important for me to thank all my friends at IAA: Manuel, Mike,

Matilde, Florian, Azaymi, Ricardo, Bannashef, Youdong . . . for organizing a lot of outdoor activities to help me get familiar with a new culture and balance in my life after work. I especially want to express my thanks to Estefania Casal and Alice Deconto who were always available when I was in trouble with health problems or whenever I need a translator. Their help is more than what I could say.

I would also want to thank the team in DENA company Prof. Joan Montanyá, Dr. Victor Lorenzo, Guillem Tobella, Enric Pons, Marcelo Arcanjo, Michele Urbani for their support and their help during my stay there. Thank you for creating a warm and friendly working environment, and giving me instant support.

I want to thank all the people in the SAINT network, where I have learned many useful lessons and social skills with lots of fun. I especially want to thank Dr. Christoph Kohn and Dr. Oscar van der Velde for your help and good advice.

This work has been made possible with the financial assistance of the European Union Horizon 2020 Framework Programme under the Marie Skłodowska-Curie Grant Agreement SAINT 722337 and the Spanish Ministry of Science and Innovation, under Projects ESP2017-86263-C4-4-R and PID2019-109269RB-C43 and FEDER program.

Finally, I would like to acknowledge the University of Granada for allowing me to get a Ph.D. degree in the Physics and Space Science Program.

Kieu Ny

Granada, 22nd July 2021

Contents

List of Figures	xix
List of Tables	xxxv
1 Introduction	1
1.1 Lightning	1
1.2 Lightning-like discharges	5
1.3 Time-resolved lightning spectroscopy	9
2 Motivation, Objectives and Thesis structure	13
2.1 Motivation	13
2.2 Objectives	15
2.3 Thesis structure	16
3 Methodology	18
3.1 Experimental setup	18
3.2 Instrument calibration	23
3.3 Theoretical considerations	28
4 Instrumentation	40
4.1 Introduction	41

4.2	GALIUS	42
4.3	Conclusions	52
5	Sub-microsecond time-resolved spectroscopy	53
5.1	Introduction	55
5.2	Instrumentation	58
5.3	Experimental Setup	59
5.4	Time Resolved Spectra	60
5.5	Electron Density and Temperature	64
5.6	Exploring Overpressure and Equilibrium Conditions in the Lightning-like Channel	66
5.7	Summary and Conclusions	69
5.8	Supporting Information	74
6	Evidence of molecular optical emissions	105
6.1	Introduction	107
6.2	Instrumentation and Experimental Setup	111
6.3	GALIUS time-resolved spectra	113
6.4	Quantitative analysis: Electron density, Temperature and Electrical conductivity	123
6.5	Conclusions	129
7	Conclusions	139
	Bibliography	142

List of Figures

1.1	The charge structure of two isolated thunderclouds including locations where lightning can occur.	2
1.2	Drawing depicting the development of a negative cloud-to-ground lightning flash. Adapted from Uman (2001)	3
1.3	The attachment processes, the transition from lightning leader to return stroke, of a triggered lightning and high voltage laboratory sparks captured by high speed cameras. Panel (a) is the original and inverted-intensity images of a negative triggered lightning; Panels (b) and (c) show images of negative polarity laboratory produced sparks (4.5 m & 5.5 m long). The common streamer zones between the downward and upward leaders are all seen in the three images. Adapted from Tran and Rakov (2015)	4
1.4	Different kinds of lightning-like discharges. Panel (a) shows the Wimshurst machine generating small sparks at IAA-CSIC, Granada. Panel (b) shows a model of a Marx generator consisting of multiple capacitors and the spark gap. Panel (c) shows the 2.0 MV Marx generator (at DENA's company) capable of producing sparks at 800 kV within the 1 m gap that we used in our experiments.	6

1.5	Different discharge features generated by an electrostatic generator at IAA - CSIC captured with a camera using 1 ms integration time recorded by Oscar van del Velde (2019).	7
1.6	The voltage charging process of the Switching Impulse (SI) and Lightning Impulse (LI) operation modes of the 2.0 Marx generator at DENA, Barcelona. Panel (a) shows the slow rising voltage of the Switching mode and Panel (b) shows the sudden rising voltage of the Lightning mode. The inset images in each figure show the appearance of the sparks produced by each operation mode while using the same voltage (800 kV) and spark-gap (1 m).	8
1.7	(a) Salanave in August 1961 using his spectrograph to record the first time-resolved lightning flash (Salanave, 1961). (b) Time-resolved spectra of a return stroke obtained by Orville using a slitless spectrograph (Orville, 1968a).	11
2.1	A simple scheme to highlight noticeable results in lightning spectroscopy research from the 1960s to early XXI century.	14
3.1	GALIUS configuration at IAA (a) and several calibration devices: (b) Compact Mercury lamp; (c) Deuterium lamp; (d) Quartz Tungsten Halogen (QTH) lamp; (e) Neon lamp.	21
3.2	GALIUS in DENA working high voltage laboratory discharges.(a) GALIUS was turned horizontally and placed 8.5 m away from the sparks. (b) 1 m long - 800 kV spark generated with the Lightning Impulse mode. (c) 1 m long - 800 kV spark generated with the Switching Impulse mode.	22

3.3 Wavelength identification process: (a) Neon lamp image of emitted wavelengths recorded by GALIUS with grating R3. We trimmed the image so that it fits into the figure, the black box is the trimming section; (b) Spectral lines of the Neon lamp extracted from one row; (c) Wavelength assignment: red dots are assigned wavelengths and the blue line is the fitting of the red dots; (d) A plot of a row in the Neon lamp image corresponding to the same row of the wavelength matrix L_{cali} 26

3.4 Wavelength calibration of grism R1 through a home made Graphical User Interface program. (a) Calibration images of Deuterium and Mercury lamps; (b) Selected wavelengths for the calibration; (c) Identification of peaks corresponding to the chosen wavelengths; (d) Wavelength assignments and fitting. 27

3.5 Flux calibration process: (a) QTH lamp recorded by a Jobin Yvon HORIBA FHR100 spectrometer; (b) QTH lamp recorded by our system with grism R3; (c) Instrument function resulting from the ratio of Jobin's response to GALIUS's response. 29

3.6 Temperature calculated from different ratios of line intensities: (a) Temperature vs ratio of two nitrogen ion lines ($I_{444.7}/I_{399.5}$); (b) Temperature vs ratio of two nitrogen ion lines (I_{661}/I_{648}); (c) Temperature vs ratio of two neutral oxygen lines (I_{715}/I_{777}); (d) Temperature vs ratio of two neutral oxygen lines (I_{795}/I_{777}). 34

3.7	Electron density diagnostics using the Full Width Half Area (FWHA): (a) Dependence of the FWHM and the FWHA of the Balmer alpha vs electron density, calculated with different temperatures (1000 - 175000 K) and ionic perturbers with reduced mass μ (0.5 - 10); (b) Example of the calculation of the FWHA for a given spectral line. In the upper figure, the stripe area is equal to half of the area, the width of that area is the FWHA. In the lower figure, the FWHA is defined as a distance between two points that give areas 1/4 and 3/4 of the total area below the spectral line (Gigosos et al., 2003).	38
3.8	Temperature and electron density quantifications: (a) Integrated areas below two nitrogen ion lines at 648.2 nm and 661.0 nm needed for tem- perature calculations. (b) Full Width at Half Area of a H_α line for electron density calculation: the shaded area is equal to half of the total area below the green dots.	38
4.1	Optical scheme of the GALIUS CMOS imaging spectrograph.	42
4.2	GALIUS mechanical housing	45
4.3	Spectral image of a deuterium lamp recorded with GALIUS for grism R1 using the collector lens D (50 mm focal length).	47
4.4	Spectral sensitivity of GALIUS for grism R1 using the collector lens D (50 mm focal length) for CMOS row number 16.	48
4.5	Spectrum of a spark produced by a Whimshurst machine measured with GALIUS (blue) R1 grism (0.29 nm spectral resolution). Spectrum of a spark produced by a small Van der Graaf generator measured with a VPH-VIS spectrograph (orange) using a 1257 lines/ mm grating with 0.75 nm of spectral resolution (Walker, 2015).	51

- 5.1 Time resolved spectra of meter long lightning-like discharges produced with the Switching Impulse (SI) mode (a) - (b) and Lightning Impulse (LI) mode (c) - (d) of a Marx generator. Panels (e) - (f) show time resolved spectra of a 4 cm long spark produced with a small electrostatic generator. The peak intensities and voltages reached in these discharges are 0.125 kA and 0.8 MV for SI mode, 3 kA and 0.8 MV for LI mode and 0.350 kA and -55.0 kV for the electrostatic spark, respectively. The strong intensities shown correspond to two singly ionized N II lines at 648.20 nm and 661.05 nm and to the H $_{\alpha}$ line at 656.27 nm. The panels in the right column show the six initial times for the SI (b) and electrostatic discharges (f), and six selected (not consecutive) instants in the temporal evolution of LI mode discharges (d). The weak doubly ionized N III emission lines at 645.41 nm and 646.70 nm marked with arrows can be seen in the very early (sub- μ s) times of spectra in panels (b) and (f). The weak N I neutral line at 648.27 nm is seen (as a soft hump) in the late times of panels (a), (c) and (e). 71
- 5.2 Temporal evolution of the measured electron density in logarithmic (a) and linear (b) scale, and temperature (c) for meter long lightning-like discharges (SI, red dots and LI, green dots), and small spark (blue dots) discharges. Due to very weak H $_{\alpha}$ signal, the electron density could not be measured at -0.120 μ s (for the SI mode discharge) and at 0.000 μ s (for the LI mode discharge). Note that the measured electron (gas) temperature values and time scale for the LI mode discharge (green dots in panel (c)) are very similar to those reported in natural lightning return strokes (Orville, 1968b) and to those recently reported by Walker and Christian (2019) in triggered lightning return strokes with peak currents of 8.1 kA. 72

5.3 Time dependence of the measured electron density (green, red and blue dots), calculated equilibrium electron densities (pink solid line) at 1 atm using the measured temperatures and δ_p (square, triangles and diamond symbols) to quantify overpressure in the discharge channel with respect to ambient pressure ($\delta_p = 1$) for (a) LI mode and (b) SI mode of meter long lightning-like discharges, and for (c) a small spark discharge. Note that the measured electron density and the channel overpressure for the LI mode discharge (panel (a)) exhibit very similar values to those reported in natural lightning return strokes (Orville, 1968b) and to those recently reported by Walker and Christian (2019) in triggered lightning return strokes with peak currents of 8.1 kA. Regarding panel (b) time -0.120 μ s (electron density could not be measured by spectroscopic means at this particular time), note that the SI measured and synthetic spectra agree very well at -0.120 μ s (see Figure 5.14 at 27000 K and Figures 5.17 in supporting information 5.8). This suggests an equilibrium (at 1 atm) electron density at the pre-trigger time of -0.120 μ s for the SI discharge shown in (b), which explains why we have included a symbol (diamond) at -0.120 μ s for the electron density corresponding to equilibrium air at 1 atm. 73

5.4 Measured voltage (blue line) and current (red line) during the generation of the Switching Impulse (SI) mode discharge of the Marx generator. (a) Complete time evolution of the voltage and current. (b) Zoom in for a close view of the rise / decay region around $100 \mu\text{s}$ with an image showing the typical appearance of the SI discharge. The green line in (b) indicates the time of the first recorded spectrum. The black dot in (b) indicates the triggering time. The injected electric energy is 81 J or 81 J/m (since the discharge length is $\simeq 1$ m). 86

5.5 Measured voltage (blue line) and current (red line) during the generation of the Lightning Impulse (LI) mode discharge of the Marx generator. Panels (a), (b) and (c) show time intervals between, respectively, $-20 \mu\text{s}$ and $100 \mu\text{s}$, $-5 \mu\text{s}$ and $20 \mu\text{s}$, and $1.5 \mu\text{s}$ and $5 \mu\text{s}$. The inset image in (a) shows the typical appearance of the LI discharge. The green line in (c) indicates the time of the first recorded spectrum. The black dot in (c) indicates the triggering time. The injected electric energy is 684 J or 684 J/m (since the discharge length is $\simeq 1$ m). 87

5.6 Measured voltage (blue line) and current (red line) during the generation of the small (4 cm long) spark discharge. (a) Complete time evolution of the voltage and current with an inset image showing the typical appearance of the small spark discharge. (b) Zoom in for a close view of the rise / decay region around $0.0 \mu\text{s}$. The green line indicates the time of the first recorded spectrum. The black dot in (b) indicates the triggering time. The injected electric energy is 1.2 J or 30 J/m (since the discharge length is $\simeq 0.04$ m). 88

5.7 Measured electron density (red dots) in the SI lightning-like discharge and the equilibrium composition in a thermal plasma of humid (50 % RH) air at 1 atm (ambient pressure in Tarrasa, Spain). The figure shows the concentrations for a selection of neutral (atoms and molecules) and ionic (atomic and molecular) species as a function of time (bottom axis) and measured temperatures (top axis). The displayed times correspond to the different SI recorded spectra. The temperatures derived from each measured spectra are shown in the top axis. The measured electron densities can be recovered by multiplying the equilibrium electron densities at 1 atm by the δ_p factor for each time (see Figure 5.3). 89

5.8 Measured electron density (green dots) in the LI lightning-like discharge and the equilibrium composition in a thermal plasma of humid (50 % RH) air at 1 atm (ambient pressure in Tarrasa, Spain). The figure shows the concentrations for a selection of neutral (atoms and molecules) and ionic (atomic and molecular) species as a function of time (bottom axis) and measured temperatures (top axis). The displayed times correspond to the different LI recorded spectra. The temperatures derived from each measured spectra are shown in the top axis. The measured electron densities can be recovered by multiplying the equilibrium electron densities at 1 atm by the δ_p factor for each time (see Figure 5.3). 90

5.9 Measured electron density (blue dots) in the small spark discharge and the equilibrium composition in a thermal plasma of humid (50 % RH) air at 0.93 atm (ambient pressure in Granada, Spain). The figure shows the concentrations for a selection of neutral (atoms and molecules) and ionic (atomic and molecular) species as a function of time (bottom axis) and measured temperatures (top axis). The displayed times correspond to the different small spark measured spectra. The temperatures derived from each recorded spectra are shown in the top axis. The measured electron densities can be recovered by multiplying the equilibrium electron densities at 0.93 atm by the δ_p factor for each time (see Figure 5.3). 91

5.10 Equilibrium composition in an atmospheric pressure plasma of humid (50 % RH) air for gas temperatures between 1000 K and 35000 K. The figure displays the concentrations of the same species shown in Figures 5.7, 5.8, and 5.9. The bluish shadowed region indicates the variation of equilibrium densities within the approximate range of measured temperatures including temperatures above measured values due to possible underestimated temperature measurements. 92

5.11 Synthetic spectra (645 nm - 665 nm) for an atmospheric pressure thermal plasma of humid (50 % RH) air for gas temperatures between 35000 K (top left) and 30000 K (bottom right). The figure illustrates the case of the meter long Switching Impulse (SI) discharge. 93

5.12 Synthetic spectra (645 nm - 665 nm) for an atmospheric pressure thermal plasma of humid (50 % RH) air for gas temperatures between 29000 K (top left) and 18000 K (bottom right). The figure illustrates the case of the meter long Switching Impulse (SI) discharge. Note that the case of 27000 K is shown with and without black body (continuum) radiation since no black body is seen in the measured spectra at $-0.120 \mu\text{s}$ (see Fig 5.14). 94

5.13 Synthetic spectra (645 nm - 665 nm) for an atmospheric pressure thermal plasma of humid (50 % RH) air for gas temperatures between 16000 K (top left) and 8000 K (bottom right). The figure illustrates the case of the meter long Switching Impulse (SI) discharge. 95

5.14 Comparison between calculated synthetic spectra (grey line) and measured spectra corresponding to the early times (from pre-trigger sub- μs to $\simeq 2.5 \mu\text{s}$ after triggering) of a meter long Switching Impulse (SI) discharge. Note that no black body emission is detected at $-0.120 \mu\text{s}$ with 27000 K (see Figure 5.2(b) for the time evolution of the measured temperatures). 96

5.15 Comparison between calculated synthetic spectra (grey line) and measured spectra corresponding to the early times (from sub- μs to $\simeq 10 \mu\text{s}$) of a meter long Lightning Impulse (LI) discharge. Weak black body emission is visible in the measured spectra at $0.0 \mu\text{s}$ with a measured temperature of 31000 K. 97

5.16 Comparison between calculated synthetic spectra (grey line) and measured spectra corresponding to the early times (from sub- μs to $\simeq 3 \mu\text{s}$) of a small spark discharge. 98

- 5.17 The factor δ_p , total pressure and partial pressures due to electrons, ions and neutrals as a function of time (left axis) in linear scale (top panel) and logarithmic scale (bottom panel). The right axis of the top and bottom panels include an estimation of the shock front speed (top panel) and shock front position (bottom panel) for the meter long SI discharge. Note that the pressure for $-0.12 \mu\text{s}$ was represented assuming an equilibrium (at 1 atm) electron density as it is suggested from Figure 5.14 at $-0.12 \mu\text{s}$ with 27000 K. Note also that the first value of the shock front position and speed are shown 240 ns after the pre-trigger time ($-0.12 \mu\text{s}$) for which the first image was recorded. 99
- 5.18 The factor δ_p , total pressure and partial pressures due to electrons, ions and neutrals as a function of time (left axis) in linear scale (top panel) and logarithmic scale (bottom panel). The right axis of the top and bottom panels include an estimation of the shock front speed (top panel) and shock front position (bottom panel) for the meter long LI discharge. . . . 100
- 5.19 The factor δ_p , total pressure and partial pressures due to electrons, ions and neutrals as a function of time (left axis) in linear scale (top panel) and logarithmic scale (bottom panel). The right axis of the top and bottom panels include an estimation of the shock front speed (top panel) and shock front position (bottom panel) for a small (4 cm long) spark discharge. 101
- 5.20 Self-absorption (SA) coefficient ($0 \leq SA \leq 1$) of the 647 nm and 661 nm singly ionized N II lines as a function of time for meter long discharges SI (top panel) and LI (middle panel), and for a small (4 cm long) spark discharge (bottom panel). A $SA = 1$ indicates a complete optically thin line emission while $SA = 0$ applies for a complete optically thick line. The signal of the 661 nm ion line was not considered reliable after $2 \mu\text{s}$ 102

5.21 Illustration of the method followed to derive the electron density. The black body background is first subtrated. Due to the large electron density the broadening of the H_α line is large and it should be considered that it extends over the entire ($\simeq 20$ nm) spectral range covered in our ultra high speed observations at 2.1 Mfps. Once the shape of the H_α (green dotted line) is determined, we compute the full width at half area (FWHA) (see grey shadow) under the green dotted line used to derived the measured electron density. The FWHA for the H_α is much less influenced by ion dynamics than the full width at half maximum (FWHM) and, consequently, it is a more reliable procedure (than using the FWHM) to obtain the electron density from the H_α line. 103

5.22 Illustration of the method followed to derive the electron temperature. To evaluate the electron temperature we only consider the intensity signal above the background (see red dots). We consider the total area (not the peak maximum) under the intensities of the 647 nm and 661 nm singly ionized N II lines. 104

5.23 Raw spectral image of the LI mode discharge generated with the Marx generator. This spectral image is 8 pixels height and 1024 pixels wide and was recorded at 2.1 Mfps. The diffraction grating used has 1855 lines per mm and a spectral resolution of 0.38 nm. 104

6.1 Time resolved R1 (380 - 450 nm) spectra of a meter long lightning-like discharge produced with the LI mode of a Marx generator with 800 kV. Panel (a) shows the entire spectral range. Panel (b) displays a zoom of the 400 - 425 spectral gap. The spectrum was recorded at 672000 fps (160 ns exposure time) with spectral and time resolutions of 0.29 nm and 1.488 μ s, respectively. Spectral lines of singly ionized atomic nitrogen and oxygen, doubly ionized atomic nitrogen and several molecular species (N_2 , N_2^+ , C_2 , CN, and CO) are visible and marked with green, purple, blue and black labels, respectively. 114

6.2 Comparison between calculated synthetic spectra (black dashed dotted line) of heated humid (80 % RH) air and measured R1 (380 - 450 nm) spectra (color line) of a meter long Lightning Impulse (LI) discharge produced with a peak voltage of 800 kV. Note that synthetic spectra do not include molecular species except for the Lyman Birge Hopfield (LBH), Second Positive System (SPS) and First Positive System (FPS) bands of N_2 132

- 6.3 Time resolved R2 (475 - 793 nm) spectra of a meter long lightning-like discharge produced with the SI mode (panel (a)) and LI mode (panels (b) and (c)) of a Marx generator with 800 kV. For easier comparison between SI and LI mode spectra, panels (a) and (b) show similar time range (but not exactly the same). Panel (c) for LI mode show spectra for times starting in 10.178 μ s. The spectra were recorded at 672000 fps (160 ns exposure time) with spectral and time resolutions of 0.75 nm and 1.488 μ s, respectively. Spectral lines of neutrals (O I, N I, H I), singly ionized atoms (N II, O II) and the C₂ Swan band head at 516.5 nm are visible. Note that the numbers stand for: (1) 485.8 - 486.7 N II, (2) 500.1 - 500.5 nm N II, (3) 516.5 nm C₂ / O II, (4) 553.5 nm N II, (5) 567.9 - 571.0 N II, (6) 592.7 - 594.1 N II, (7) 616.8 nm N II, (8) 648.2 nm N II, (9) 656.3 nm H I, (10) 661.0 N II, (11) 715.6 O I, (12) 742.4-744.3-746.8 nm N I, (13) 777.4 nm O I. 133
- 6.4 Comparison between calculated synthetic spectra (black dashed dotted line) of heated humid (80 % RH) air and measured R2 (475 - 793 nm) spectra (color line) of a meter long Lightning Impulse (LI) discharge produced with a peak voltage of 800 kV. Note that synthetic spectra do not include molecular species except for the Lyman Birge Hopfield (LBH), Second Positive System (SPS) and First Positive System (FPS) bands of N₂. The peak associated to the C₂ Swan band is visible at 516.5 nm. . . 134

- 6.5 Time resolved R4 (770 - 805 nm) spectra of a meter long lightning-like discharge produced with the SI mode (panels (a, b)) and LI mode (panels (c, d)) of a Marx generator with 800 kV. The spectra were recorded at 1400000 fps (160 ns exposure time) with spectral and time resolutions of 0.34 nm and 0.714 μ s, respectively. Triplets of oxygen neutrals (O I) at 777 nm and 795 nm are clearly visible. 135
- 6.6 Electron densities and temperatures in a meter long lightning-like discharge produced with 800 kV in the SI (panels (a, c) and LI (panels (b, d)) modes. Temperatures are quantified using different combinations of neutral (O I 777 nm and O I 795 nm with R4) and ion lines (NII 648 nm and NII 661 nm with R2, and N II 399.50 nm and N II 444.70 nm with R1). Electron densities are obtained from the Stark broadening of the 777 nm O I triplet and from the full width at half area (FWHA) of the H_{α} line at 656.30 nm. We have included for comparison electron densities and temperatures reported in a previous paper (see yellowish line) using grism R3 (645 nm - 665 nm) recorded at 2.1 Mfps for the same discharge and setup (Kieu et al., 2020). Note that the inset marked with (e) in panel (d) is a zoom out of the first time steps (up to 12 μ s) in panel (d). 136
- 6.7 Lorentzian fit of the OI 777 nm triplet in the Switching (SI) mode (a) at 0.964 μ s and in the Lightning (LI) mode (b) at 4.12 μ s recorded with grism R4 (\sim 0.34 nm spectral resolution). The red line is the triplet Lorentzian fit (sum) to the measured (grey dots) intensity of the O I 777 nm triplet. The blue, orange and green lines are the resulting single Lorentzians fits for each line component of the O I 777 nm triplet. . . . 137

6.8 Time evolution of the electrical conductivity of a point in a heated ~ 1 m long lightning-like discharge channel produced with 800 kV in the LI mode. The electrical conductivity was computed using values of N_e (see Figure 6.6(b)) and T (see Figure 6.6(d)) derived from the FWHM of the O I 777.4 nm line, and the O I line ratios 777/715 and 777/795 obtained from spectra recorded with gratings R2 and R4, respectively. The solid lines are a guide for the eye. 138

List of Tables

3.1	GALIUS recording speeds with different gratings.	21
3.2	Coefficients to calculate temperatures with different spectral lines. Note that $1 \text{ eV} = 8065.6 \text{ cm}^{-1}$	33
3.3	Wavelength broadening of the H_α line due to different mechanisms. Adapted from Walker (2015)	36
3.4	Calculated Stark-broadening parameters for the 777.1 nm atomic oxygen line as given by Griem (1964)	39
4.1	GALIUS interchangeable collimator lenses.	42
4.2	GALIUS configurations	43
4.3	GALIUS interchangeable collector lenses	44
4.4	Photron Fastcam SA-Z	44
4.5	GALIUS spectral features	49
4.6	GALIUS spatial features	50

6.1 Molecular species and vibro-electronic optical transitions detected in the present study. N₂ Second Positive System (SPS) and N₂⁺ First Negative System (FNS) transitions were taken from [Gilmore et al. \(1992\)](#) and [Camacho et al. \(2007\)](#). Transitions of CO were taken from [Czech et al. \(2013\)](#) and [Al-Tuwirqi et al. \(2012\)](#). Transitions from C₂ and CN were taken from [Wallace \(1960, 1964\)](#), and [Czech et al. \(2012\)](#) 115

Chapter 1

Introduction

1.1 Lightning

Lightning is one of the most impressive and common geophysical phenomenon on Earth which is usually generated in thunderstorms. Observations from the space-based instrument OTD (Optical Transient Detector) have reported that nearly 1.4 billion flashes occur annually over the entire Earth. This counts for an average of 44 ± 5 flashes in each second ([Christian et al., 2003](#)). These observations also confirmed that lightning occurs mainly over land areas, with an average ratio of $\sim 10:1$ in comparison to their occurrence over the ocean. Due to its high frequent occurrence and high temperature, lightning is considered to be a major direct source of nitrogen oxides NO_x (i.e. nitric oxide NO and nitrogen dioxide NO_2) that significantly affect upper troposphere ozone distributions ([Schumann and Huntrieser, 2007](#)).

Even though lightning are common, they are not well understood. For instance many unknowns remain regarding their inception mechanisms and full chemical influence in the atmosphere. In general, they can be classified into 2 main groups:

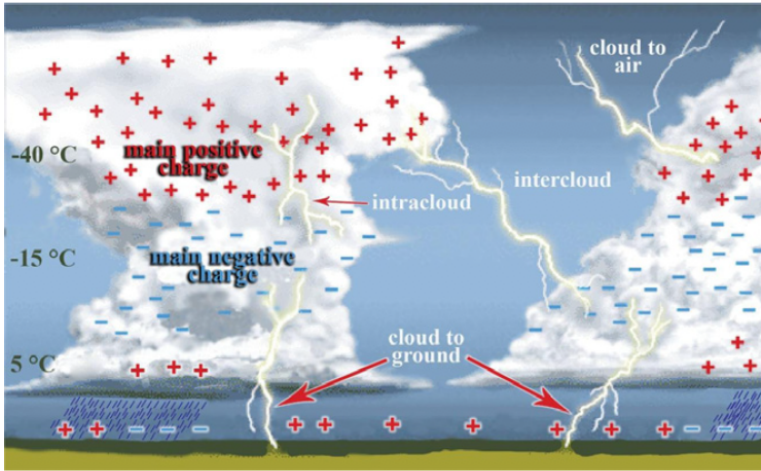


Figure 1.1: The charge structure of two isolated thunderclouds including locations where lightning can occur.

cloud-to-cloud and cloud-to-ground. The cloud-to-cloud discharges account for the majority of lightning and include three different types: intracloud (the discharges occur totally within a single cloud), intercloud (those that occur between clouds), and cloud-to-air (occurring between one cloud and the surrounding air). Cloud-to-ground lightning are the most commonly investigated. Details of different lightning discharges are shown in Figure 1.1.

A typical cloud-to-ground lightning flash develops in three stages (Rakov and Uman, 2003): First, the collisions between ice particles and water droplets together with gravity separate positive and negative charges inside the thundercloud and *build up a voltage*. Then a discharge grows, forming a faint leader - called *stepped-leader* - which proceeds slowly from cloud to ground forming a conducting path. When this stepped leader contacts the ground, a very energetic and bright stroke propagates rapidly up the ionized path; this is the *first return stroke*. After a pause of 30 to 50 ms, a new leader - called *dart-leader*, proceeds uniformly from cloud to ground and is followed by another bright return stroke

propagating upward; this is the *second return stroke*. A cloud-to-ground flash is made up of several leaders and return-strokes. First strokes are initiated by *stepped-leaders* while subsequent strokes are initiated by *dart-leaders*. Figure 1.2 sketches this process with different time steps (Uman, 2001).

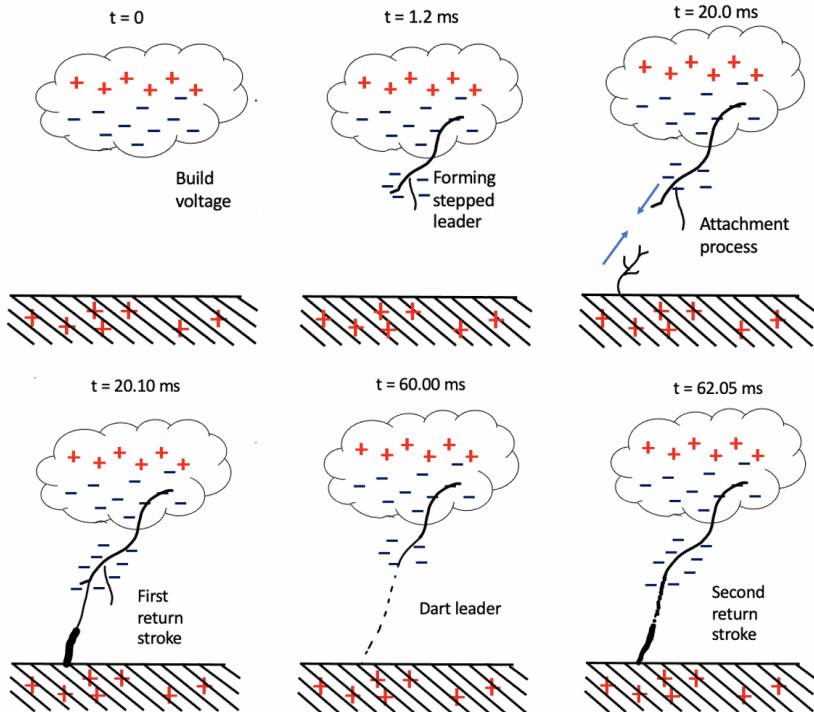


Figure 1.2: Drawing depicting the development of a negative cloud-to-ground lightning flash. Adapted from Uman (2001).

It can be considered that lightning research begins in 1746 when Benjamin Franklin set up experiments in his laboratory to study atmospheric electricity phenomena. He generated electricity by rubbing together two dissimilar materials and charging Leyden jars in series. In 1749, he described the similarities between lightning and the laboratory sparks he had created. In 1750 he published the design of an experiment involving vertical metal rods insulated from the Earth

intended to prove that lightning was an electrical phenomenon. The experiment was first performed successfully in France in May 1752 (Dwyer and Uman, 2014).

In 1916, Wilson received a Nobel Prize for his invention of the cloud chamber to estimate the charge structure in thunderstorms and the individual charge involved in a lightning discharge (Dwyer and Uman, 2014).

From 1970 until now, lightning research has been very active and productive due to the need to prevent damages caused by lightning to properties, aircraft, spacecraft and sensitive ground-based installations. After 1975, the use of rocket and wire-triggered lightning from natural thunderstorms became a relatively widespread technique since one can control the occurrence of lightning in time and space.

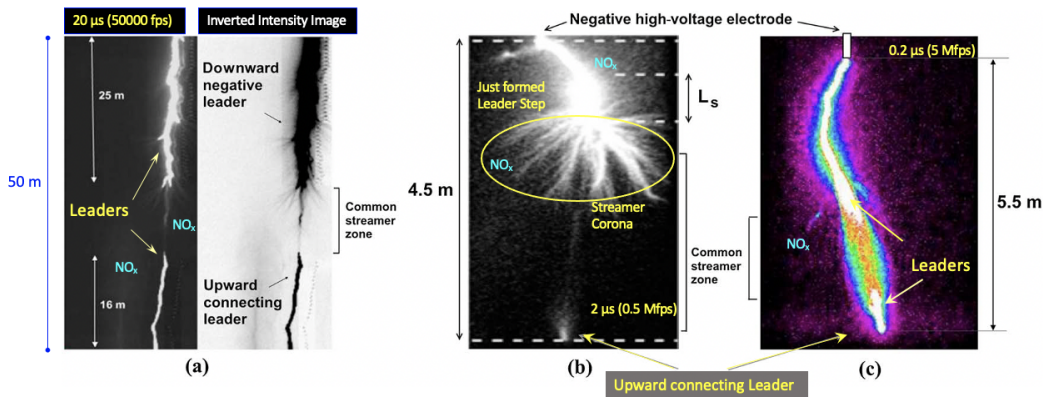


Figure 1.3: The attachment processes, the transition from lightning leader to return stroke, of a triggered lightning and high voltage laboratory sparks captured by high speed cameras. Panel (a) is the original and inverted-intensity images of a negative triggered lightning; Panels (b) and (c) show images of negative polarity laboratory produced sparks (4.5 m & 5.5 m long). The common streamer zones between the downward and upward leaders are all seen in the three images. Adapted from Tran and Rakov (2015).

High voltage laboratory discharges is another option one can use to study lightning discharges with the possibility to control the discharge gap (length), current and voltage. An example illustrating the similarity between triggered

lightning and laboratory discharges is shown in Figure 1.3. These images were captured with high speed cameras at the break-through phase of the attachment process and the transition from leader to return stroke. Figure 1.3(a) shows the original and inverted-intensity images of a negative triggered lightning just prior to the return stroke frame, recorded at 50000 fps ($20 \mu\text{s}$ integration time); Figure 1.3(b) shows an image of laboratory produced negative sparks (4.5 m long) captured by an image converter camera at 0.5 Mfps ($2 \mu\text{s}$ integration time); Figure 1.3(c) is a color coded image captured at 5 Mfps ($0.2 \mu\text{s}$ integration time) of a 5.5 m long laboratory produced negative spark. The common streamer zone between the downward leader and the upward connecting leader channel are all seen in the three images.

1.2 Lightning-like discharges

There are different types of electrical generators that can be used to produce sparks. In this section, we introduce two main types of generators we used to produce laboratory electrical discharges at different high voltages and currents which we call *lightning-like discharges*.

After the building process, GALIUS was tested with small sparks created by a small electrostatic generator (a Wimshurst Machine). The Wimshurst machine is able to generate high voltages up to 30 kV depending on the disc radius and low continuous current sparks. This device was developed between 1880 and 1883 by the British inventor James Wimshurst (1832 - 1903). It has a distinctive appearance with two large contra-rotating discs mounted in a vertical plane, two crossed bars with metallic brushes, and a spark gap between two metal spheres, as shown in Figure 1.4(a).

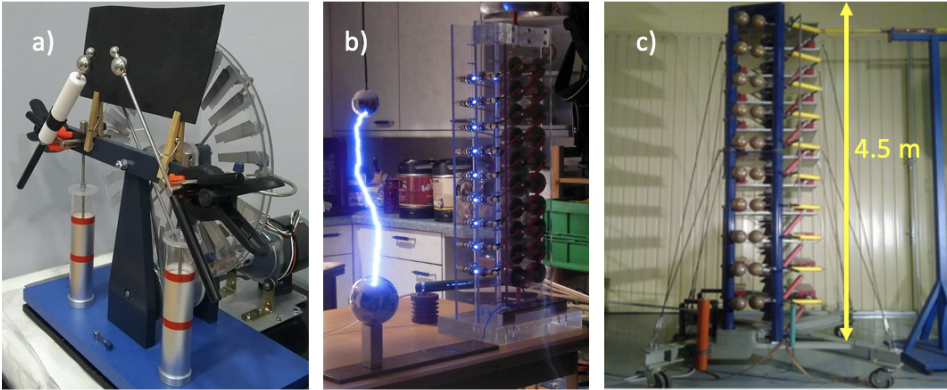


Figure 1.4: Different kinds of lightning-like discharges. Panel (a) shows the Wimshurst machine generating small sparks at IAA-CSIC, Granada. Panel (b) shows a model of a Marx generator consisting of multiple capacitors and the spark gap. Panel (c) shows the 2.0 MV Marx generator (at DENA’s company) capable of producing sparks at 800 kV within the 1 m gap that we used in our experiments.

The Wimshurst machine was originally operated only by hand. However, in order to save time for our experiments, we motorized it so that with just one click the machine generates single or consecutive sparks. Figure 1.5 shows distinct features of different discharges generated by the electrostatic machine at the IAA. These features are similar to those seen in real lightning discharges. We can see in Figure 1.5: streamer-like (a), corona-like (b), leader-like (c) and return stroke-like (c and d) structures. These images were taken by Oscar Van De Velde with his camera operated with 1 ms integration time. The sparks shown in panels (c) and (d) are 4 cm long which is the standard inter-electrode gap used with this machine in our experiments at the IAA.

After a testing period at the IAA, GALIUS was moved to Tarrasa (Barcelona), at DENA’s company high voltage facility to work with electrical discharges produced by a 2.0 MV Marx generator. A Marx generator is a type of electric impulse generator, named after Erwin Otto Marx who first proposed it in 1923, which produces very short high-voltage or high-current surges from a low-voltage

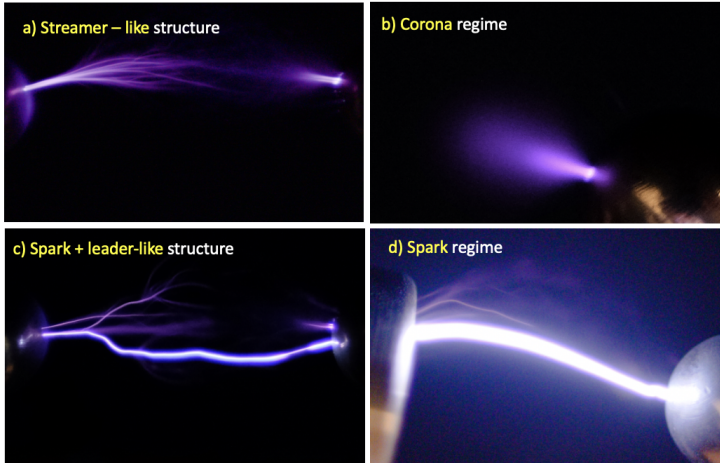


Figure 1.5: Different discharge features generated by an electrostatic generator at IAA - CSIC captured with a camera using 1 ms integration time recorded by Oscar van del Velde (2019).

DC supply.

There are two types of Marx generators: impulse voltage and impulse current. The impulse voltage generators consist of multiple capacitors that are first charged in parallel through charging resistors by a high-voltage, direct-current source and then connected in series and discharged through a test object by a spark gap. The impulse current generators comprise many capacitors that are also charged in parallel by a high-voltage, low-current, direct-current source, but it is discharged in parallel through resistances, inductances, and a test object by a spark gap. Figure 1.4(b) shows an example of a model of Marx generator consisting of multiple capacitors and its spark gap.

The configuration of the Marx generator at Tarrasa (Barcelona) that we used is of the impulse voltage type, which can produce sparks of up to 1 MV, as shown in Figure 1.4(c). The machine can produce sparks in two modes: Lightning Impulse (LI) and Switching Impulse (SI). The difference in the voltage charging dynamics of the two modes lead to the differences in currents, luminosity, lifetimes,

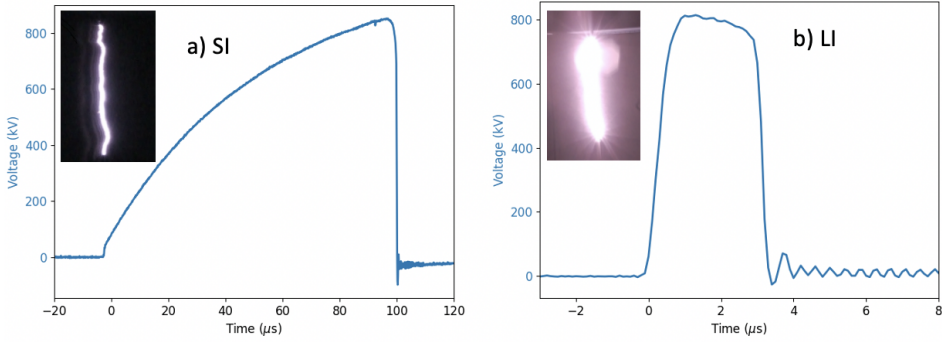


Figure 1.6: The voltage charging process of the Switching Impulse (SI) and Lightning Impulse (LI) operation modes of the 2.0 Marx generator at DENA, Barcelona. Panel (a) shows the slow rising voltage of the Switching mode and Panel (b) shows the sudden rising voltage of the Lightning mode. The inset images in each figure show the appearance of the sparks produced by each operation mode while using the same voltage (800 kV) and spark-gap (1 m).

brightness and noises. An example of the voltage charging in LI and SI modes are shown in Figure 1.6, both sparks were set up at the same voltages (800 kV) and lengths (1 m).

- **Switching Impulse** (SI) sparks: The voltage slowly rises to its maximum value (800 kV) in 100 μs and then discharge. The generated sparks have currents with around 125 A with enough luminosity for observations, low noise and small radius sizes, as shown in Figure 1.6(a).
- **Lightning Impulse** (LI) sparks: The voltage immediately rises up to its maximum in 0.5 μs and stay at the peak during 2-3 μs , and then it suddenly discharges. The measured currents were around 3 kA, the sparks produced were extremely bright and noisy as shown in Figure 1.6(b).

1.3 Time-resolved lightning spectroscopy

Lightning flashes have been investigated with spectroscopy since the nineteenth century but those initial analyses did not give much information due to the limitations of the instruments at that time. These original instruments were usually adapted from pre-existing instruments which astronomers used to study auroras, nebulae, and other faint sources. The adapted instruments were constructed with a slit and were operated to record lightning flashes reflected from clouds (Salanave, 1961).

It would be very difficult to image a lightning flash into a conventional slit spectrograph since lightning itself is a thin, fast and luminous source. Therefore, slitless spectrographs were developed together with diffraction gratings, which produce instruments with high spectral dispersion and good spectral resolution. The disadvantage of slitless spectrographs is the difficulty for wavelength identification and instrument calibration since we can not control the spectral ranges. Contrary, a slit spectrograph allows easy wavelength identification and flux calibration but it is more difficult to catch a flash of thin luminous channel which occur randomly and far away. Despite the disadvantages, slit and slitless spectrographs are the two main spectroscopic techniques employed for lightning spectroscopy.

Some of the milestones of lightning slit and slitless spectroscopy at the beginning of the twentieth century were: First slitless spectra recorded by Pickering (1901) and Fox (1903); First slit spectra captured by Slipher (1917); 14 slit spectra (280-656 nm) obtained by Dufay (1926). These spectra included features from atomic nitrogen and oxygen and molecular species like N_2 . Israel and Wurm (1941) estimated the energy level of nitrogen ion N II lines and first reported that the degree of excitation depends on the altitude of the optical emission in the

lightning channel. In 1949, Dufay continued studying lightning spectra towards the UV bands (290-380 nm). His slitless spectra showed the emissions of OH and the most intense bands from the second positive system (SPS) of N_2 and N_2^+ (Dufay, 1949). From 1950, extended observations were made into the near infrared. Those spectra showed that lightning optical emissions are mainly due to neutral oxygen, nitrogen, and argon (Offroy et al., 2015).

Since 1960, chemical species identification in lightning spectra had reached a step further when Wallace (1960) indicated the presence of CN violet bands, the N_2 second positive system, and the N_2^+ first negative system in a near-ultraviolet (367-428 nm) lightning slit spectrum. He also estimated that the temperature in the lightning channel is in the range from 6000 K to 30000 K (Wallace, 1960). Zhivlyuk and Mandel'shtam (1961) also derived temperature values in the lightning channel of around 20000 ± 5000 K. In 1963, Wallace identified optical emissions of singly-ionized oxygen and nitrogen, and the presence of Stark-broadened neutral oxygen and nitrogen species when examining lightning spectra in the range 315-980 nm (Wallace, 1964). Until the early 1960s lightning spectra were *time-averaged* since they were the temporal average of several lightning flashes.

On 17th August 1961, the first *time-resolved* spectra of lightning flashes were obtained in Tucson (Arizona) by Salanave (1961) (see Figure 1.7). He used a slitless spectrograph with time and spectral resolutions of about 20 ms and 0.2 nm, respectively. He recorded spectra from 385 nm to 690 nm for each flash (Salanave, 1961). From these spectra, a series of quantitative analysis on lightning spectra came out (Prueitt, 1963), (Uman, 1963, 1964), (Uman and Orville, 1964, 1965), (Uman et al., 1964), (Orville and Uman, 1965). For example, Prueitt (1963) calculated the temperature in 5 different lightning flashes; Uman, Orville and Salanave

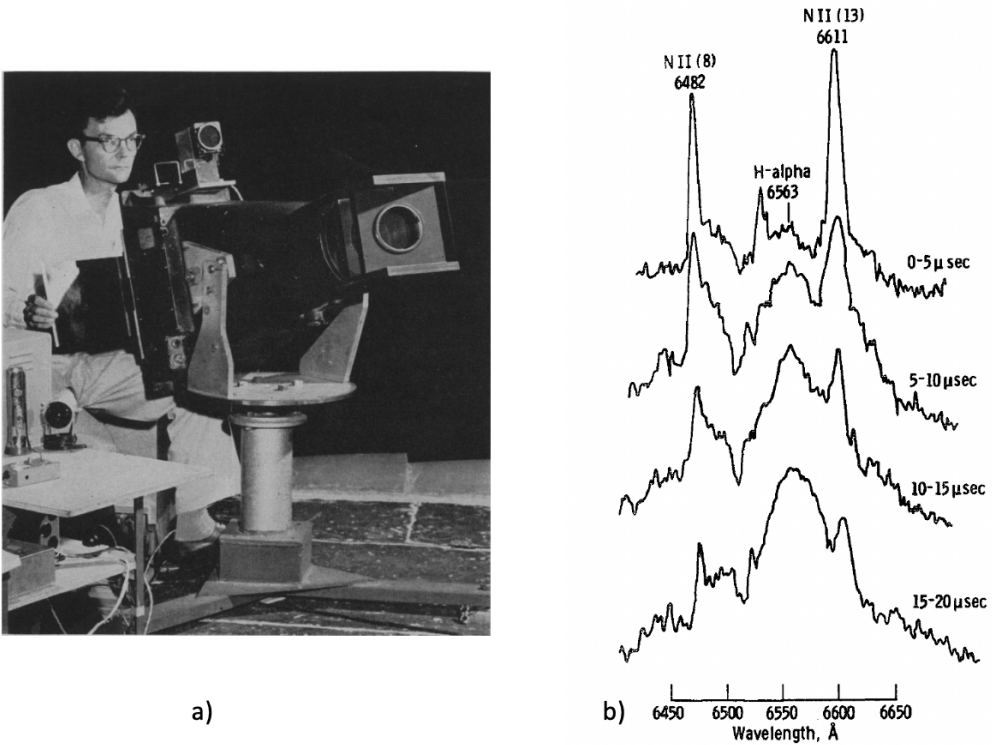


Figure 1.7: (a) Salanave in August 1961 using his spectrograph to record the first time-resolved lightning flash (Salanave, 1961). (b) Time-resolved spectra of a return stroke obtained by Orville using a slitless spectrograph (Orville, 1968a).

studied the maximum temperature, electron density, mass density of air and pressure in the heated lightning channel. The continuum spectra, the opacity and the optical thickness were also discussed in these studies. These quantitative analyses laid a firm foundation for the time-resolved lightning spectroscopic diagnostics.

In 1968, the first time-resolved spectra of lightning strokes between cloud and ground were recorded on film by Orville (1968a). These spectra were obtained in the range 400 - 660 nm by a slitless spectrograph, with a time resolution of 2 - 5 μ s and 1 nm wavelength resolution. They showed the optical emissions of neutral hydrogen, neutral and singly ionized atoms of nitrogen and oxygen. No molecular or doubly ionized optical emissions were identified. The peak temperature in

five of the ten spectra was in the range 28000 K - 31000 K. The highest peak temperature was calculated to be 36000 K. The time dynamics of the electron density derived from Stark-broadened H_{α} lines presented a decrease from 10^{18} cm^{-3} to 10^{17} cm^{-3} in about 25 μs (Orville, 1968b).

During the summer of 2012 and 2013, Walker and Christian obtained the first high-speed spectra of a triggered lightning recorded at 673000 fps (Walker and Christian, 2017). These spectra were recorded with 1.5 μs of time resolution showing the evolution in each phase of the flash: the initial stage, dart leader, return stroke and continuing current. Spectra of return stroke contained optical emissions of neutral, singly and doubly ionized nitrogen and oxygen, neutral argon and neutral hydrogen. It was also the first time that doubly ionized nitrogen lines were identified. Their estimations of the temperature and electron density in the lightning channel were far higher than in the previous results: the temperature exceeded 40000 K and the electron density reached up to $\sim 10^{19} \text{ cm}^{-3}$ due to their high-speed recording (Walker and Christian, 2019).

As the recording speed increases, lightning spectra have progressively shown the transition phases in the early time and optical emissions of highly excited species including ion emissions. This motivates us to work on these topics using faster recording speeds, higher sensitivity sensors and wider spectral ranges so that we can deepen our knowledge on lightning dynamics and chemistry.

Chapter 2

Motivation, Objectives and Thesis structure

2.1 Motivation

The scheme in Figure 2.1 summarizes important results in lightning spectroscopy from the 1960s up to 2019. The upper side of the arrow indicates the accessible time regimes of the instruments and the lower side highlights some results connected to the identification of species and the quantification of key magnitudes from lightning spectra.

Regarding chemical identification, Wallace (1960) identified the existence of molecules, neutral and ionized atoms in time-averaged lightning spectra. Salanave et al. (1962) also confirmed their existence in his first time-resolved spectra of a lightning flash since these emissions may correspond to long-lasting species which may be created during the cooling down process of atoms and ions in a lightning channel. The time-resolved spectra of Orville (1968a) and Walker and Christian (2017) showed strong optical emissions of singly ionized and even double ionized

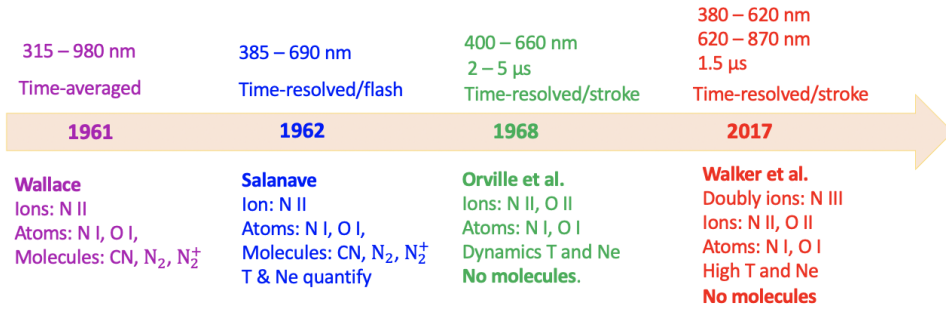


Figure 2.1: A simple scheme to highlight noticeable results in lightning spectroscopy research from the 1960s to early XXI century.

species because their instruments were able to access into the early time of species evolution and record optical emissions of highly excited atomic states. However, these spectra were slitless and the recorded spectral range depended on the distance from the lightning channel to the instrument. Most of these spectra were recorded from the visible to the near-infrared (400 - 880 nm), and there were no molecular optical emissions reported in them.

Regarding quantification, [Wallace \(1964\)](#) estimated the average temperature of lightning flashes varying from 6000 K to 30000 K. This was achieved by using the rotational vibration bands of CN emissions. Previously, [Zhivlyuk and Mandel'shtam \(1961\)](#) had calculated temperatures around 20000 ± 5000 K by using the assumption that lightning emit like a black body. As mentioned before, the first time-resolved spectra were achieved by [Salanave \(1961\)](#). In 1961 and soon afterwards, quantification from lightning spectra began: temperatures were calculated from intensities of atomic lines; electron density, mass density and pressure in the lightning channel were also estimated from Boltzmann's and Saha's equations. Other authors also discussed about the continuous lightning spectra, opacity, optical thickness, equilibrium as well as on a number of assumptions being used in their estimations ([Prueitt, 1963](#); [Uman, 1964](#); [Uman et al., 1964](#);

Uman and Orville, 1964; Uman, 1963; Orville and Uman, 1965; Uman and Orville, 1965). The time-resolved spectra by Orville (1968b) showed the dynamics of the above mentioned magnitudes in time, especially the rising of the temperature in the early time of some lightning strokes. More recently, the triggered lightning spectra reported by Walker and Christian (2019) revealed very high temperatures and electron densities thanks to its fast recording speed, short integration times and sensor sensitivity.

Together with these achievements, there are some questions that remains:

- Will we get higher temperatures and electron densities with higher time resolutions?
- Can we better understand molecular optical emissions from lightning spectra using GALIUS?

2.2 Objectives

The goals of this thesis are to carry out novel time-resolved imaging and spectroscopy campaigns of lightning and lightning-like discharges with a high speed camera and an ultra-fast spectrograph. The purpose of these studies is to dig into the temporal dynamics and the chemical influence of lightning in the atmosphere.

These goals will be achieved by following a number of steps:

- Building up and characterizing the instrument GALIUS
- Recording spectra of laboratory discharges with different GALIUS configurations
- Study of chemical identification and quantitative estimations from recorded spectra: temperature, electron density, overpressure, electrical conductivity,

etc.

- Preparing the system for real lightning campaigns

2.3 Thesis structure

To make it clear and not to rewrite what we have already published, the thesis will be structured into 4 main chapters, not including the introduction, motivation and conclusions.

- **Chapter 3: Methodology**

In this chapter, we describe the experimental set up, calibration processes and data analysis for quantifications of key magnitudes. We describe here details of the assumptions, methods, parameters and fitting models which we used to quantify the temperature, electron density, overpressure and electrical conductivity of the lightning-like channel together with radial position and velocity of the lightning-like shockwave front.

- **Chapter 4: Instrumentation**

We describe here the results obtained from the characterization of the system. In this chapter, we present the main optical parameters, design features and all possible GALIUS configurations. The calibration processes were also performed including wavelength identification and flux corrections for all configurations. We published these results in *Applied Optics* ([Passas et al., 2019](#)).

- **Chapter 5: Sub-microsecond time-resolved spectroscopy**

These are the results of different laboratory discharges recorded at 2.1 Mfps. Three different discharges were recorded: 4 cm sparks generated

by a Wimshurst machine and two 1 m long high-voltage laboratory sparks generated by a Marx generator in Switching and Lightning modes operated at 800 kV. This was the first time that time-resolved lightning-like spectra was recorded at sub-microsecond ($0.476 \mu\text{s}$ time resolution) timescale. We explored the time-dependent behavior of these discharges, computed time-dependent temperatures and electron densities in the heated channel and compared them with those previously obtained in real lightning by other authors. These results were published in *Geophysical Research Letters* (Kieu et al., 2020).

- **Chapter 6: Evidence of molecular optical emissions**

Evidences of optical emissions from different molecular species were found in GALIUS spectra from the near ultraviolet-blue to the visible spectral ranges. We not only detected molecular emissions previously reported, but also optical emissions from new species such as CO and C₂ not seen before in lightning spectra. Also we applied different methods to derive time-dependent temperatures, electron densities and electrical conductivity in the heated channel. These results were published in *Journal of Geophysical Research: Atmospheres* (Kieu et al., 2021).

Chapter 3

Methodology

3.1 Experimental setup

3.1.1 GALIUS configurations

GALIUS is a spectroscopic system using a slit ($50\ \mu\text{m} \times 3\ \text{mm}$) and a high-speed camera. As shown in Figure 3.1(a), the instrument includes:

- A *collective lens* in front of the system: to focus the incident light from observed objects on a *slit*. If the observed objects are far away (greater than 15 m), then the distance from the collective lens to the slit is equal to its focal length.
- A *slit*, next to the collective lens: to allow only a portion of the incident light to pass through the system. Only a portion of the observed objects which are imaged on the centre of the CMOS (Complementary Metal Oxide Semiconductor) are recorded. The use of a slit allows the system to control spectral ranges of the recorded images. Regardless of the locations of the discharges, we will always record their images with the same spectral range

provided we use the same grism.

- *Collimated lens*, after the slit: to create collimated beams and direct them to the diffraction grating.
- *Volume Phase Holographic (VPH)*: to control spectral range and spectral resolution of the system. A VPH diffracts light by refractive index modulations within a thin layer of material sandwiched between two glass substrates. It can achieve higher diffractive efficiencies in many applications than conventional gratings. GALIUS is configured with 4 different VPHs, we usually refer to them with short names such as *grisms* or *gratings*: R1, R2, R3, R4.
- *Camera lens of the camera*: to focus the collimated beams from the VPH on the CMOS of the camera.
- *High sensitivity camera*: to record images of the observed objects. GALIUS is based on a Photron FASTCAM SA-Z type 2100K with maximum recording speed up to 2100000 frame-per-second (fps).

With four interchangeable gratings (VPHs), four collimated lenses and several collective lenses, GALIUS has in total 22 configurations. Details of these parameters will be described in chapter 4. We designed all these configurations to record sparks in the laboratory and real lightning in the field. In this chapter, we present the configurations for the recording of 4 cm sparks, and 1 m long sparks at DENA.

3.1.2 Experimental setup at the IAA-CSIC, Granada

GALIUS was initially set up horizontally on an optical table so that we can change its configuration easily. We recorded spectra of 4 cm sparks generated by a

Wimshurst machine located 2 m away from the collective lens. The configurations of GALIUS for the different spectral ranges were:

- Near-ultraviolet: FASTCAM - Camera lens 50 mm, F#1.2 - VPH **R1** - Collimated lens 105 mm, F#4.5 - Slit - Collective lens 50 mm - Distance to spark 60 cm.
- Visible range: FASTCAM - Camera lens 50 mm, F#1.2 - VPH **R2** - Collimated lens 50 mm, F#1.2 - Slit - Collective lens 200 mm - Distance to spark 2 m.
- Visible range: FASTCAM - Camera lens 50 mm, F#1.2 - VPH **R3** - Collimated lens 50 mm, F#1.2 - Slit - Collective lens 200 mm - Distance to spark 2 m.
- Near-infrared: FASTCAM - Camera lens 50 mm, F#1.2 - VPH **R4** - Collimated lens 50 mm, F#1.2 - Slit - Collective lens 200 mm - Distance to spark 2 m.

For each configuration, we calibrated the system using calibration lamps (see Figure 3.1): the Mercury lamp (b) and Deuterium lamp (c) were used to calibrate the system in the near-ultraviolet with grism R1; the Quartz Tungsten Halogen (QTH) (d) and Neon lamps (e) were used to calibrate the system from the visible to the near-infrared range with gratings R2, R3, R4. These lamps were usually located 60 cm away from the system, except the Mercury lamp which was placed around 10-20 cm away due to its small intensity.

The Photron FASTCAM in our system can record images from 50 fps up to 2.1 Mfps. The full size of the sensor is 1024×1024 pixels, but if we increase the recording speeds, we have to sacrifice the size of the images. For the calibration,

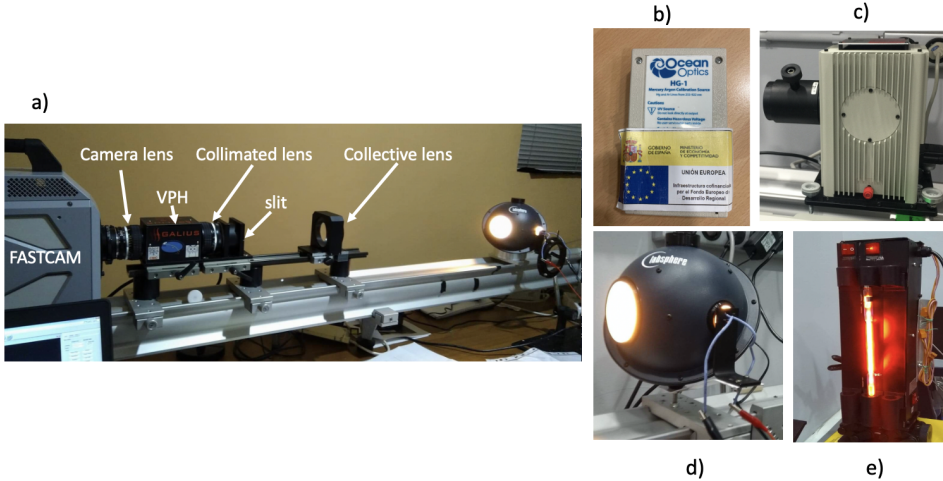


Figure 3.1: GALIUS configuration at IAA (a) and several calibration devices: (b) Compact Mercury lamp; (c) Deuterium lamp; (d) Quartz Tungsten Halogen (QTH) lamp; (e) Neon lamp.

we recorded calibrated images at 50 fps for the different gratings corresponding to different spectral ranges. Table 3.1 shows recording speeds corresponding to different gratings and camera sensor's size.

Table 3.1: GALIUS recording speeds with different grisms.

Grism (VPH)	Spectral range (nm)	Speed (fps)	Camera sensor (pixel)
R1	380 - 450	672000	1024×16
R2	475 - 795	672000	1024×16
R3	645 - 665	2100000	128×8
R4	770 - 850	1440000	256×8

3.1.3 Experimental setup at DENA, Tarrasa

After the testing period at the IAA, GALIUS was moved to Tarrasa (Barcelona) to work with vertically oriented sparks. We fixed the system into an aluminum box which can be rotated both horizontally and vertically. Figure 3.2(a) shows

3.1. EXPERIMENTAL SETUP

the setup in Tarrasa, the system was rotated horizontally by 90 degrees. Figures 3.2(b) and 3.2(c) show the 1 m long high voltage discharges produced by the 2.0 MV Marx generator with 800 kV in Lightning and Switching Impulse modes, respectively. The sparks were 8.5 m away from the system. The experiments were set up with 4 different VPHs with sparks produced in the LI and SI modes. Details of each configuration are:

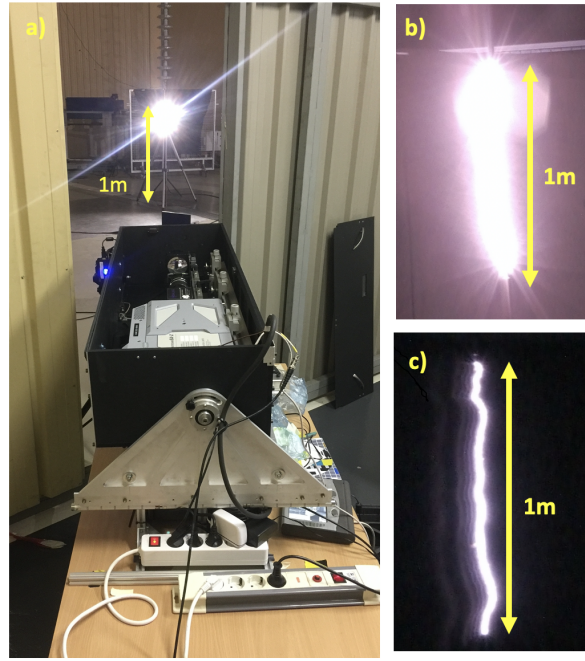


Figure 3.2: GALIUS in DENA working high voltage laboratory discharges.(a) GALIUS was turned horizontally and placed 8.5 m away from the sparks. (b) 1 m long - 800 kV spark generated with the Lightning Impulse mode. (c) 1 m long - 800 kV spark generated with the Switching Impulse mode.

- Near-ultraviolet: FASTCAM - Camera lens 50 mm, F#1.2 - VPH **R1** - Collimated lens 105 mm, F#4.5 - Slit - Collective lens 50 mm - Distance to spark 8.5 m.
- Visible range: FASTCAM - Camera lens 50 mm, F#1.2 - VPH **R2** - Colli-

mated lens 50 mm, F#1.2 - Slit - Collective lens 30 mm - Distance to spark 8.5 m.

- Visible range: FASTCAM - Camera lens 50 mm, F#1.2 - VPH **R3** - Collimated lens 50 mm, F#1.2 - Slit - Collective lens 30 mm - Distance to spark 8.5 m.
- Near-infrared: FASTCAM - Camera lens 50 mm, F#1.2 - VPH **R4** - Collimated lens 50 mm, F#1.2 - Slit - Collective lens 30 mm - Distance to spark 8.5 m.

3.2 Instrument calibration

Before doing any data analysis, we need to calibrate the system so that we can avoid errors caused by the optical elements of our systems. We followed the steps which were already implemented to calibrate the GRANada Sprite Spectrograph and Polarimeter (GRASSP) developed in our group ([Passas et al., 2016b](#)):

- *Wavelength calibration*: Assign wavelengths to certain pixels and correct the curvature of the CMOS.
- *Flux calibration*: Correct the inhomogeneous response of the camera sensor to a certain spectral range.

3.2.1 Wavelength calibration

The wavelength calibration process includes *wavelength identification* and *distortion correction*. This task can be done by recording images of calibration lamps which we know their emitted wavelengths. Normally, we recorded calibration images at 50 fps with sensor size 1024×1024 pixels. Figure 3.3 shows an example

of wavelength identification for a Neon lamp image. These steps were done by following the sequence:

- *Step 1:* Trim (cut) the calibration images. As shown in Figure 3.3(a) the Neon images fit in 256 vertical pixels. We also trimmed horizontal pixels just to make the image fit into the figure. The black box in Figure 3.3(b) represents the Neon images after trimming.
- *Step 2:* Plot and identify spectral lines of Neon lamps for each row of the image, as shown in Figure 3.3(b). We don't have to choose all emitted lines, we just choose the good ones and avoid the saturated and small intensity lines. This task is called *wavelength assignment*.
- *Step 3:* Fit wavelength assignment of step 2 by using a polyfit function. The blue line, as shown in Figure 3.3(c), is the fitting line of all red dots. If the fitting is not good, we have to check again the wavelength assignments.
- *Step 4:* Create a wavelength matrix with the same size of the Neon lamp image and then fill this matrix with assigned wavelengths by repeating the wavelength assignment for all rows of the image. This matrix is named L_{cali} .

We finish the wavelength identification with a wavelength matrix L_{cali} which is the wavelength assignments of the Neon lamp image. However, this matrix and the Neon lamp image may include the curvature of the CMOS. The process of correcting this curvature is called *distortion correction* which can be done by:

- *Step 5:* Correct the curvature in the wavelength matrix L_{cali} requires: (1) create a new matrix with the same size of the wavelength matrix L_{cali} ; (2) assign a new range (wavelength or pixel) for all columns of the new matrix; (3) interpolate each row in the old matrix; (4) fill the interpolated values

into the new matrix. We also repeated the curvature correction for the Neon lamp image and the wavelength matrix L_{cali} .

The steps above are needed for the calibrations of Neon images. For images of the sparks (spectral images), we need to repeat the calibrations but the spark images are not of the same sizes as the calibration images. Therefore, we need to add a few more steps:

- *Step 6:* Remove background noise by subtracting spark images to a median background image which is the mean of black images we recorded during the experiments. Notice that the background images were recorded at the same speed of the spectral images.
- *Step 7:* Trim the L_{cali} matrix to the size of the spark images from the center of the CMOS. We call the new matrix L_{trim} which represents the wavelength and the curvature of the spark images in the CMOS.
- *Step 8:* Repeat the distortion correction described in *Step 5* but using the new matrix L_{trim} and spark images. Usually, the curvature is not important if we use only 8 or 16 vertical pixels of the CMOS.

For each configuration of GALIUS, we need to use a suitable calibration lamp. Basically, we used a Neon lamp (Figure 3.1(e)), to calibrate spectra in the visible range (grism R2, R3); an Argon lamp to calibrate spectra in the near-infrared (grism R4); Deuterium lamp and a compact Mercury lamp (see Figure 3.1(b)-(c)) to calibrate the system in the near-ultraviolet (grism R1).

To save time for the calibration process, we used Python to build a Graphical User Interface (GUI) program that makes easier to interact with the underlying calibration code through its graphical icons. An example of the calibration with grism R1 is shown in Figure 3.4 which was done following the sequence:

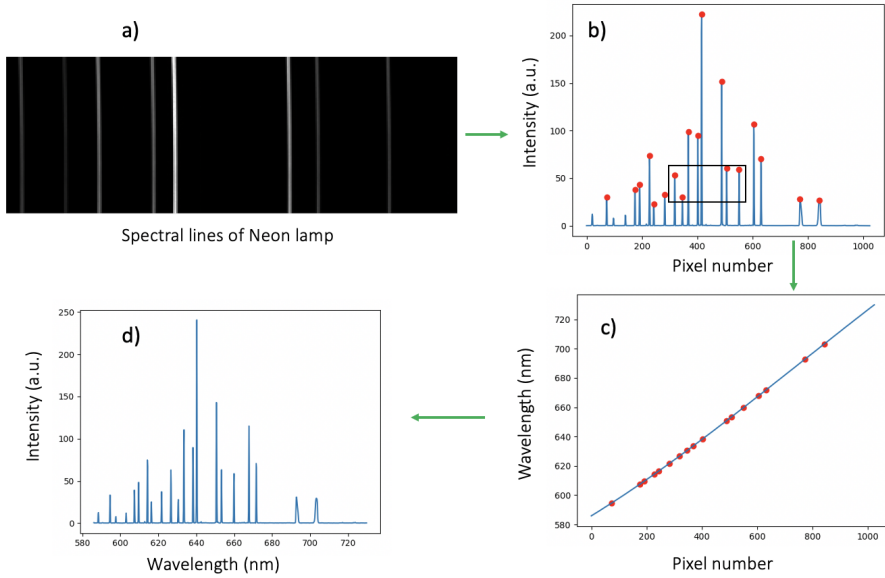


Figure 3.3: Wavelength identification process: (a) Neon lamp image of emitted wavelengths recorded by GALIUS with grating R3. We trimmed the image so that it fits into the figure, the black box is the trimming section; (b) Spectral lines of the Neon lamp extracted from one row; (c) Wavelength assignment: red dots are assigned wavelengths and the blue line is the fitting of the red dots; (d) A plot of a row in the Neon lamp image corresponding to the same row of the wavelength matrix L_{cali} .

- Load the calibration images including the Deuterium and Mercury lamp images, as shown in panel (a)
- Choose wavelengths for the calibration, then click on the ‘Load D’ button, the code will show a plot of the calibration images as shown in panel (c)
- Click on the peaks which correspond to the wavelengths we chose in panel (b)
- Check wavelength assignments in the figure shown in panel (d). If the fitting is not good, the blue line will not fit well the red dots. We can recalibrate again by changing wavelengths in panel (b) and click on the ‘ReFIT’ button.
- Click on the ‘OK’ button if the wavelength calibration is fine. Save the

wavelength matrix and continue to the flux calibration process.

As can be seen in panel (d) of Figure 3.4, even using the full horizontal size (1024 pixels) of the sensor, we only use effectively half of the sensor size from 380 nm. The system is hardly sensitive below 380 nm.

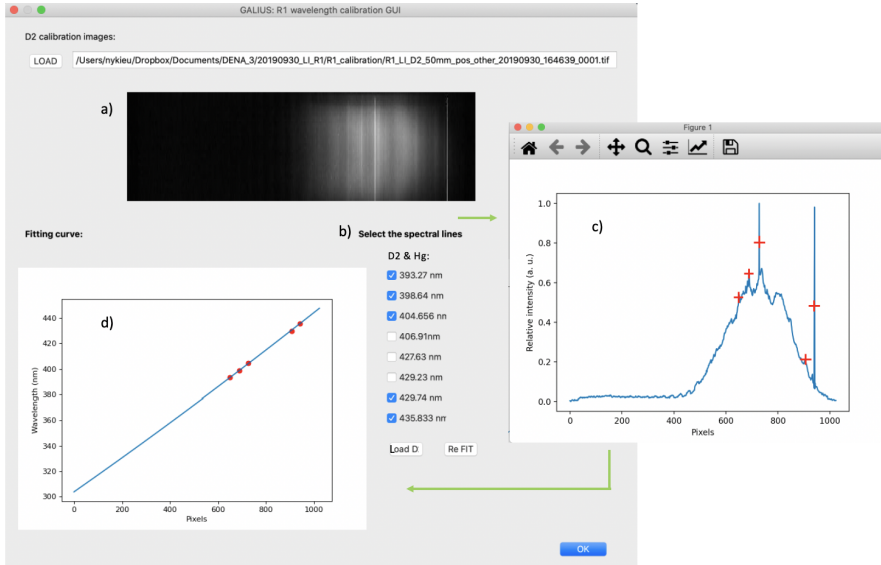


Figure 3.4: Wavelength calibration of grism R1 through a home made Graphical User Interface program. (a) Calibration images of Deuterium and Mercury lamps; (b) Selected wavelengths for the calibration; (c) Identification of peaks corresponding to the chosen wavelengths; (d) Wavelength assignments and fitting.

3.2.2 Flux calibration

Flux calibration is a procedure to correct the inhomogeneities of the system in a certain spectral range. These inhomogeneities can be seen by the response of the sensor within a certain spectral range recorded by a standard spectrometer. In our case we used a Jobin Yvon HORIBA FHR100 spectrometer, and the response recorded by our system. To correct it, we define a function named Instrument Function, IF, which is the ratio of the response recorded by the Jobin Yvon

HORIBA FHR100 spectrometer, S_{Jobin} , to the response recorded by GALIUS, S_{GALIUS} .

$$IF = \frac{S_{Jobin}}{S_{GALIUS}}. \quad (3.1)$$

Figure 3.5(a - b) show the responses of both spectrometers (Jobin Yvon and GALIUS with grism R3) to a continuous light source (600 - 730 nm). An example of an Instrument Function (IF) is shown in Figure 3.5(c). To finish the flux calibration process, we just need to multiply the image obtained after wavelength calibration, I_{wcali} , by the Instrument Function as:

$$I_{final} = I_{wcali} \times IF. \quad (3.2)$$

In the visible and near-infrared (grisms R2, R3, R4) spectral ranges GALIUS is calibrated with a QTH, as shown in Figure 3.1(d). However, in the near-ultraviolet (grism R1), the system was calibrated with a Deuterium lamp (see Figure 3.1(c)). The spectral response of the Deuterium lamp in the near-ultraviolet will be presented in the chapter 4.

3.3 Theoretical considerations

3.3.1 Assumptions

In the transition from a leader to a return stroke, a lightning channel changes quickly from a relatively cold plasma to a very hot plasma when many species emit light at the same time in a short period. The quantification of the temperature and electron density in this period needs to consider some assumptions. These assumptions were used and discussed in detail by Prueitt (1963), Uman (1969b)

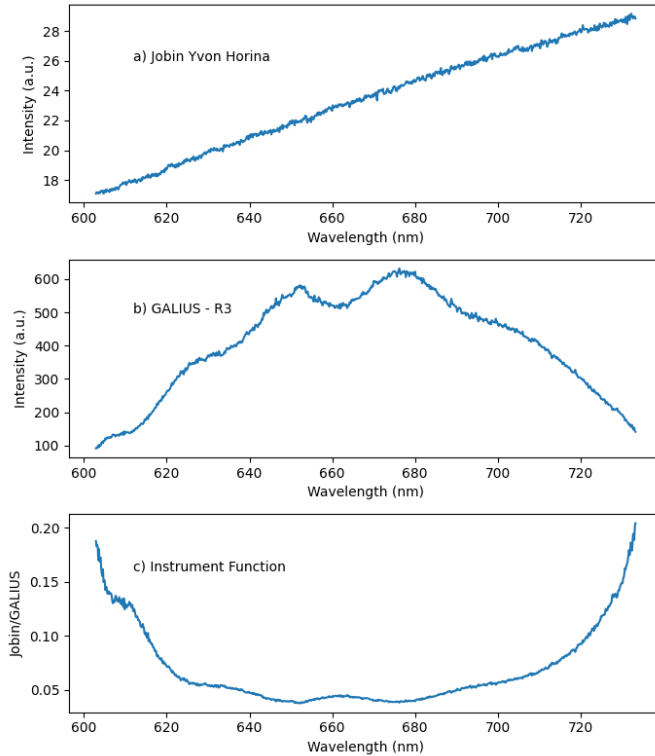


Figure 3.5: Flux calibration process: (a) QTH lamp recorded by a Jobin Yvon HORIBA FHR100 spectrometer; (b) QTH lamp recorded by our system with grism R3; (c) Instrument function resulting from the ratio of Jobin’s response to GALIUS’s response.

and [Walker and Christian \(2019\)](#). We present here their general ideas:

- **Optically thin plasma**

The plasma channel of a lightning stroke must be optically thin which means that atomic optical emissions occurring within the heated lightning channel will propagate through the plasma without being absorbed. This means that the measured temperatures come directly from where the emitter is located.

If the channel is not optically thin, the optical emissions from the center would be absorbed and reemitted by the atoms resulting in blackbody radi-

ation. In such a case the temperature measurements would correspond to a surface temperature.

- **Channel Uniformity**

The channel must have a relatively uniform temperature, i.e. the temperature at the edge is similar to that at the center. Considering that at the beginning of the discharge, the channel reaches high temperature and pressure, the plasma channel rapidly expands behind a shock wave and the radiation mechanism is the dominant loss mechanism. This would imply that the measured radiation comes from a narrow temperature distribution. If this was not true, then the temperature would decrease with the increase of the radius.

- **Boltzman distribution and local thermodynamic equilibrium (LTE)**

The assumption of local thermodynamic equilibrium requires that the velocity distribution of electrons is Maxwellian and that the energy levels of the atoms and ions are populated according to the Maxwell-Boltzmann statistics. This is frequently the situation in high density plasmas where collisional effects completely dominate the radiative ones. This is the most arguably assumption since the energy is continuously supplied during the return stroke phase of lightning and an intense luminosity is observed. The channel can nevertheless be considered to be in a quasi-equilibrium state relative to the time that the physical parameters of the stroke change. In other words, the observed times (exposure time of the instrument) are short compared to the time it takes for the temperature to change.

3.3.2 Temperature

Under the conditions of LTE the population of a particular excited level N_n is given by:

$$N_n = N_0 \frac{g_n}{B(T)} \exp\left[-\frac{\epsilon_n}{kT}\right] \quad (3.3)$$

where N_n is the number density (cm^{-3}) of atoms or ions in the energy level n , N_0 is the total number density (cm^{-3}) of atoms or ions, ϵ_n is the excitation energy (eV) of the n th level, k is the Boltzmann constant (eVK^{-1}), T is the electron or gas temperature (K), g_n is the statistical weight of the level, and $B(T)$ is the partition function. The partition function describes the statistical properties of a system in thermodynamics equilibrium. On the other hand, the statistical weight of an energy level is an indication of its degeneracy. Once the partition function is known one can derive important state functions of the system such as the internal energy, free energy, entropy, etc.

The line intensity (Wm^{-3}) due to transitions from level n to level r in an optically thin gas kept at uniform temperature and density is:

$$I_{nr} = CN_n A_{nr} h\nu_{nr}, \quad (3.4)$$

where A_{nr} is the Einstein emission coefficient (s^{-1}), which is the probability per unit time that an atom or ion in an energy state n will spontaneously emit light and transition to a lower energy state r , ν_{nr} is the frequency (s^{-1}) of the emitted photon, h is Planck's constant (eVs), and C is a geometric factor. Combining

3.3. THEORETICAL CONSIDERATIONS

equations (3.3) and (3.4), the line intensity can be written as:

$$I_{nr} = \frac{CN_0 g_n A_{nr} h \nu_{nr}}{B(T)} \exp\left[-\frac{\epsilon_n}{kT}\right]. \quad (3.5)$$

For a different transition within the same atomic or ionic species, i.e. from level m to level p , in the same ionization state, the intensity is given by:

$$I_{mp} = \frac{CN_0 g_m A_{mp} h \nu_{mp}}{B(T)} \exp\left[-\frac{\epsilon_m}{kT}\right]. \quad (3.6)$$

By combining equations (3.5) and (3.6) the ratio of the line intensity of the transition from n to r to the line intensity of the transition from m to p is:

$$\frac{I_{nr}}{I_{mp}} = \frac{g_n A_{nr} \nu_{nr}}{g_m A_{mp} \nu_{mp}} \exp\left[-\frac{\epsilon_n - \epsilon_m}{kT}\right]. \quad (3.7)$$

Rearranging terms in equation (3.7), the temperature can be calculated as:

$$T = \frac{\epsilon_n - \epsilon_m}{k \ln(I_{nr} g_m A_{mp} \nu_{mp} / I_{mp} g_n A_{nr} \nu_{nr})}. \quad (3.8)$$

In our analysis, we calculated the temperatures of the discharges with different emission lines: two pairs of nitrogen ion lines (444.7 nm and 399.5 nm, 648.2 nm and 661.05 nm), two pairs of neutral oxygen lines (777 nm and 715 nm, and 777 nm and 795 nm) in the near-infrared. Details of the coefficients needed to calculate temperatures are shown in Table 3.2. These coefficients are obtained from the NIST database. The energy levels, $\epsilon_i - \epsilon_k$, are shown in cm^{-1} . One can easily convert to eV by noting that $1 eV = 8065.6 \text{ cm}^{-1}$. Figure 3.6 shows four plots of the temperature vs ratio of different intensities. In the interval from 10000

Table 3.2: Coefficients to calculate temperatures with different spectral lines. Note that $1 \text{ eV} = 8065.6 \text{ cm}^{-1}$.

Atom/Ion (Grism)	$\lambda(\text{nm})$	g_{ik}	$A_{ik} \text{ (s}^{-1}\text{)}$	$\epsilon_i - \epsilon_k \text{ (cm}^{-1}\text{)}$
N II (R1)	444.730	5	1.12e+08	187091.37 - 164610.76
	399.500	3	1.22e+08	174212.03 - 149187.80
N II (R3, R2)	661	7	6.01e+07	189335.16 - 174212.03
	648	3	2.58e+07	164610.76 - 149187.80
O I (R2)	777	15	3.69e+07	86627.778 - 73768.200
	715	5	5.05e+07	116631.094 - 102662.026
O I (R4)	777	15	3.69e+07	86627.778 - 73768.200
	795	21	3.62e+07	113719.80 - 101143.45

K to 40000 K, the temperature seems to exhibit a close to linear behaviour with the line ratios 715/777, 795/777 and 661/648.

The error in the temperature is estimated as:

$$\frac{\delta T}{T} = \frac{1}{\ln(Rg_m\nu_{mp}A_{mp}/g_n\nu_{nr}A_{nr})} \left[\left(\frac{\delta R}{R} \right)^2 + \left(\frac{\delta A_{mp}}{A_{mp}} \right)^2 + \left(\frac{\delta A_{nr}}{A_{nr}} \right)^2 \right]^{1/2} \quad (3.9)$$

where $R = I_{nr}/I_{mp}$ is the ratio of the intensities from two emission lines. Normally, δR is considered equal to the signal-to-noise ratio since it depends on the experimental data. Another way to calculate this value is to use *bootstrap method*. The key feature of the bootstrap method is subsampling the data with replacement (i.e., if we have N data points, we select among them N points allowing for repetition) (Efron and Tibshirani, 1985).

3.3.3 Electron density

There are several mechanisms that control the broadening of a spectral line. In general, they are classified into four main mechanisms: natural broadening,

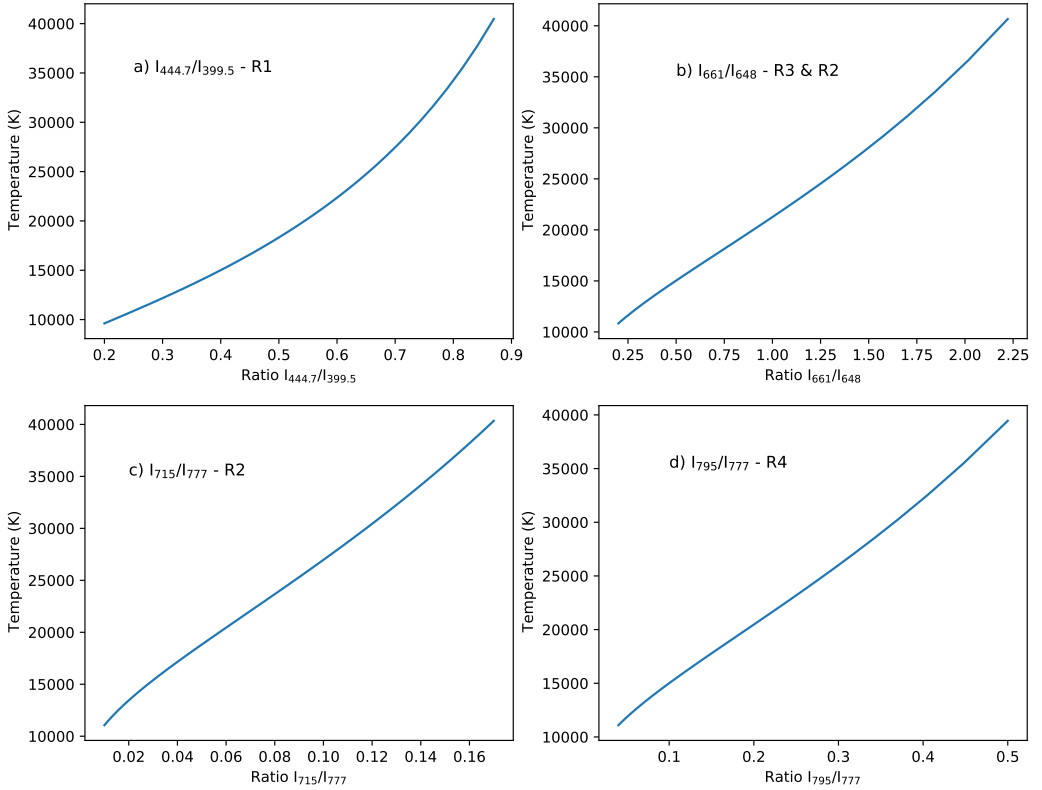


Figure 3.6: Temperature calculated from different ratios of line intensities: (a) Temperature vs ratio of two nitrogen ion lines ($I_{444.7}/I_{399.5}$); (b) Temperature vs ratio of two nitrogen ion lines (I_{661}/I_{648}); (c) Temperature vs ratio of two neutral oxygen lines (I_{715}/I_{777}); (d) Temperature vs ratio of two neutral oxygen lines (I_{795}/I_{777}).

Doppler broadening, collisional broadening and pressure broadening.

- *Natural broadening* is caused by the uncertainty principle that connects the uncertainty of the lifetime of an excited state with the uncertainty of its energy.
- The *Doppler broadening* is caused by the distribution of velocities of the species relative to the observer. The higher the temperature of the gas species, the wider the distribution of velocities in the gas.

- *Collisional broadening* is caused by the interaction of the emitting atoms with surrounding particles. Collisions interrupt radiative emission processes and increase the uncertainty in the energy emitted. This effect depends on the density and the temperature of the gas.
- *Pressure broadening* is caused by the interaction of emitting atoms with charged particles within the plasma. The electric microfields of neighboring charged particles break the degeneracy of energy levels of the emitting atom. All the transitions of new energy levels create a continuum of Stark effects which results in a broadened emission line. This broadening is also called Stark broadening.

In addition to these mechanisms, the line broadening is also affected by the instrument. This broadening can be measured with a calibration lamp. It is limited by the spectral resolution of the instrument usually determined by the slit and the grisms used. Table 3.3 summarizes the effects of these broadenings on the H_α line. As we can see, the Stark broadening and the instrument broadening are the two dominant effects. When neglecting other mechanisms, the total broadening of a line can be calculated by:

$$\Delta\lambda_{total} = 0.5 \times \Delta\lambda_S + \sqrt{0.5\Delta\lambda_S^2 + \Delta\lambda_I^2}, \quad (3.10)$$

where $\Delta\lambda_{total}$ is the total broadening, $\Delta\lambda_S$ is the Stark broadening and $\Delta\lambda_I$ is the instrument broadening. However, for sufficiently high electron density ($\geq 10^{16}$ cm⁻³), Stark broadening dominates and the electron densities are proportional to the width of the broadening. Griem and Barr (1975) calculated the relationship between Stark broadenings and electron density by considering how the quasistatic

ion electric field influences the species energy levels:

$$N_e = 8.02 \times 10^{18} \left(\frac{\Delta\lambda_{1/2}}{\alpha_{1/2}} \right), \quad (3.11)$$

where $\Delta\lambda_{1/2}$ is the Full Width Half Maximum of the emission line and $\alpha_{1/2}$ is the reduced wavelength from Griem's calculation of Stark broadening (Griem and Barr, 1975).

Table 3.3: Wavelength broadening of the H $_{\alpha}$ line due to different mechanisms. Adapted from Walker (2015).

Broadening mechanism	Wavelength broadening (Å)
Natural	0.00046
Doppler	0.71
Collisional	0.004
Stark Broadening	5 - 300
Instrument (GALIUS)	3 - 7.5

The Full Width at Half Maximum (FWHM) is widely used in plasma diagnostics and therefore it can also be used to derive the electron density from lightning spectra (Uman and Orville, 1964; Orville, 1968b; Walker and Christian, 2019). However, it is well known that ion dynamics can significantly modify both the lines width and the lines shape, especially in the case of lines with a non-shifted central Stark component (Gigosos et al., 2003). These effects are caused by the kinetics of the emitter and the surrounding environment, resulting in the dependence on the emitter's mass, temperature and kinetic equilibrium between emitters and electrons that have greater mobility.

Taking into account the ion dynamic effects, Gigosos et al. (2003) calculated the dependence of the FWHM on temperatures and reduced masses of the electron-ion system as a function of electron density for the first three lines of the

hydrogen Balmer series (H_α , H_β , H_γ). These calculations were done for a wide range of electron densities (10^{14} - 10^{19} cm^{-3}), temperatures (1000 K - 175000 K) and ionic perturbers reduced mass values μ (0.5 - 10) with the plasma in equilibrium or out of equilibrium. Figure 3.7(a) shows the dependence of the FWHM, represented by long black bars, and of the Full Width at Half Area (FWHA), represented by short black bars, as a function of the electron density with different temperatures and reduced masses. From these plots, they obtained a useful linear fitting function to calculate the electron density from the broadening of H_α that is independent of T and μ :

$$N_e = 10^{17} \times \left(\frac{\text{FWHA}}{1.098} \right)^{1.47135} \text{cm}^{-3}, \quad (3.12)$$

where FWHA is the distance between two points where the integrated area below them is equal to half of the total area, as shown in Figure 3.7(b). To quantify the variability of their calculations, five groups of 5000 simulations were run and the final line shapes were averaged over 25000 samples. These calculations also showed that the dependence of the FWHM on the temperature and reduced masses are strong for the H_α and H_γ lines but not for the H_β line.

In our estimations, we used the FWHA of the H_α broadening to estimate the electron density. The advantage of this method is that we can estimate the electron density even when the plasma channel is far from thermodynamic equilibrium. Theoretically, the total integrated area below a spectral line is the integral to infinity but when dealing with experimental results, the integration limits are the limits of the H_α line broadening. Figure 3.8(b) shows an example of the FWHA calculated from the H_α broadening. The integration limits to derive the total area go from 645 nm to 663 nm.

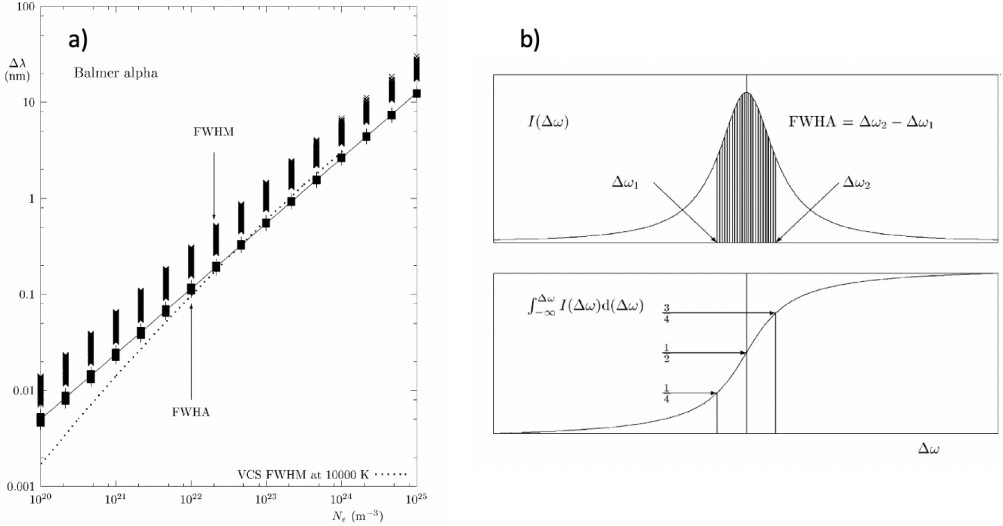


Figure 3.7: Electron density diagnostics using the Full Width Half Area (FWHA): (a) Dependence of the FWHM and the FWHA of the Balmer alpha vs electron density, calculated with different temperatures (1000 - 175000 K) and ionic perturbers with reduced mass μ (0.5 - 10); (b) Example of the calculation of the FWHA for a given spectral line. In the upper figure, the stripe area is equal to half of the area, the width of that area is the FWHA. In the lower figure, the FWHA is defined as a distance between two points that give areas $1/4$ and $3/4$ of the total area below the spectral line (Gigosos et al., 2003).

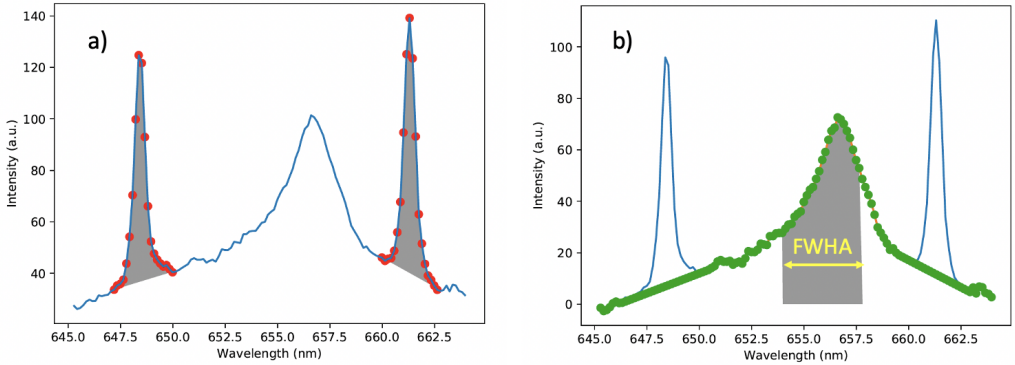


Figure 3.8: Temperature and electron density quantifications: (a) Integrated areas below two nitrogen ion lines at 648.2 nm and 661.0 nm needed for temperature calculations. (b) Full Width at Half Area of a H_α line for electron density calculation: the shaded area is equal to half of the total area below the green dots.

Stark broadening can also be present in spectral lines of many neutral and ionized species other than the H_α line. [Griem \(1964\)](#) calculated Stark broadening for a number of atoms and ions and derived equation (3.13). From this equation, we can estimate the electron density from the broadening of the neutral oxygen line 777 nm assuming that $\Delta\lambda_S \gg \Delta\lambda_I$. For that we need to compare the measured Stark broadening and the calculated broadening,

$$\Delta\lambda_{Stark}[\text{\AA}] = 2\omega(T) \frac{n_e[\text{cm}^{-3}]}{10^{16}}, \quad (3.13)$$

where $\Delta\lambda_{Stark}$ is the measured Stark broadening evaluated with the FWHM. $\omega(T)$ is a Stark broadening parameter calculated by [Griem \(1964\)](#) and shown in Table 3.4 for the O I 777 nm line. In our calculations $\omega(T)$ was obtained by graphical interpolation for different calculated temperatures.

Table 3.4: Calculated Stark-broadening parameters for the 777.1 nm atomic oxygen line as given by [Griem \(1964\)](#).

T(K)	2500	5000	10000	20000	40000	80000
$\omega(T)$	0.0199	0.0248	0.0327	0.0443	0.0566	0.0649

The Stark effect not only broadens the spectral lines but also causes a shift in their maximum. However, additional shifts can also be caused by the instrument performance, the calibration process and possible background corrections which make it more difficult to determine the contribution of the Stark shift to the possible total shift of a spectral line. The values of $\omega(T)$ given in Table 3.4 can be used only to provide a first rough estimation of the electron density.

Note that [Griem \(1964\)](#) also pointed out that only the strongest line of each multiplet was calculated because the other sublines would have the same Stark profiles within the expected precision of the calculations.

Chapter 4

Instrumentation

The content in this chapter was published in *Applied Optics* with title ‘**GALIUS: an ultrafast imaging spectrograph for the study of lightning**’.

Authors: Passas, M., Sánchez, J., **Kieu, T. N.**, Sánchez-Blanco, E. and Gordillo-Vázquez, F. J.

Volume **58**, Issue **29**, pp. 8002-8006

First published: 16 September 2019

<https://doi.org/10.1364/AO.58.008002>

Abstract

We present the main parameters, design features and optical characterization of the GrAnada LIghtning Ultrafast Spectrograph (GALIUS): a portable, ground-based spectrographic system intended for the analysis of the spectroscopic signature of lightning. It has been designed to measure the spectra of the light emitted from natural and triggered lightning and artificial electrostatic discharges at recording speeds up to 2.1 Mfps. It includes a set of four interchangeable gratings

covering different spectral ranges (from 375 nm to 854.5 nm) with spectral resolutions from 0.29 to 0.76 nm. A set of ten collector lenses allows to record the spectrum of electrostatic discharges and lightning in different scenarios.

4.1 Introduction

Lightning spectroscopy is a matter of interest to the atmospheric research community since midnineteenth century. Specially nowadays, when the progress of technology makes possible the improvement of both temporal and spatial resolution (XR) of the measurement of lightning spectrum thanks to the incipient development of CCD and CMOS ultra-high speed cameras and volume phase holographic (VPH, hereinafter) diffraction gratings.

The fastest spectrograph to date designed to record lightning spectrum was developed by the Department of Atmospheric Science of the University of Alabama in Huntsville, with a maximum recording speed of 1 Mfps ([Walker and Christian, 2017, 2019](#)). They recorded the first high-speed slit less spectra of triggered lightning at 660000 fps, distinguishing its different phases and identifying neutral, singly and doubly ionized nitrogen, oxygen and some neutral argon lines, with a lack of any traces of molecular emissions ([Walker and Christian, 2017](#)).

Higher speed measurements would give an idea of the initial temporal stages of, for instance, lightning leaders or how high can become the temperature in lightning return stroke channels. In this sense, we have designed, developed and calibrated the GrAnada LIghtning Ultrafast Spectrograph (GALIUS), the first portable ultra high speed spectrograph designed to analyze key properties such as electron density and gas temperature of lightning and high voltage (HV) electrostatic discharges up to 2.1 Mfps.

4.2 GALIUS

4.2.1 Experimental device

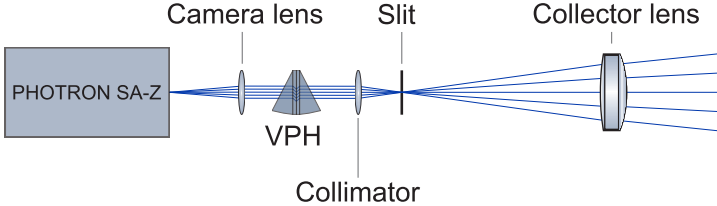


Figure 4.1: Optical scheme of the GALIUS CMOS imaging spectrograph.

Figure 4.1 shows the optical scheme of GALIUS. A total of 22 configurations can be set up, combining ten interchangeable collector lenses with four interchangeable gratings. The collimator characteristics also vary, depending on the spectral range we want to measure (see Table 4.1). Table 4.2 shows the characteristics of the four different VPHs: R1 to measure the UV spectral range and R2, R3 and R4 to measure the visible–NIR spectral range. Let us call the UV setup to the configuration resulting from combining R1 with collector lenses A, B, C or D. And let us call the Visible-NIR setup to the possible configuration resulting from combining R2, R3 or R4 with collector lenses E, F, G, H, I or J.

Table 4.1: GALIUS interchangeable collimator lenses.

Spectral range	Focal length	F#
UV	105 mm	4.5
Visible-NIR	50 mm	1.2

The optical scheme of GALIUS, following the light path, consists of a collector lens (see Table 4.3), an optional slit of $50 \mu\text{m} \times 3 \text{ mm}$, a collimator (see Table 4.1), a grism (see Table 4.2), a camera lens of 50 mm focal length and F#1.2 and a PHOTRON SA-Z CMOS ultrahigh speed camera. Optical rails and holders

Table 4.2: GALIUS configurations

Grism	Lines/mm	Spectral resolution	Spectral range	Collector lenses
R1	2086	0.2945 nm	380 nm - 450 nm	A, B, C, D
R2	1015	0.7530 nm	464 nm - 794 nm	E, F, G, H, I, J
R3	1855	0.3831 nm	587.7 nm - 737.8 nm	E, F, G, H, I, J
R4	1727	0.3456 nm	706.7 nm - 854.5 nm	E, F, G, H, I, J

set all the components inside a portable housing (see Figure 4.2). In the UV scenario, we place a 345 nm high pass filter between the collimator and the VPH to avoid second order spectra between 200 and 400 nm in the spectral response of a commercial spectrograph that we used to calculate GALIUS instrument function. GALIUS also includes a photometer that triggers the Photron SA-Z camera when a threshold of photons is detected, and a WATEC WAT-902H2 ultimate with a 3005VX4 sensor wide-field camera, to discern the origin of the recorded spectra.

4.2.1.1 Housing

GALIUS is housed in a portable aluminum box of 1100 mm x 380 mm x 230 mm, which can be bent in elevation from 0° until 50° thanks to a linear actuator and a telescopic mechanism attached on its fixed base (see Figure 4.2).

4.2.1.2 Grisms

We have designed four interchangeable grisms. They consist of an embedded VPH transmission grating between two prisms so the path of the light keeps straight. Table 4.2 summarizes the specifications of the grisms R1 (UV), R2 (Visible-NIR), R3 (Visible-NIR) and R4 (Visible-NIR).

Table 4.3: GALIUS interchangeable collector lenses

Lens	Focal length	F#	Spectral range
A	25 mm	1	250 - 425 nm
B	30 mm	1.50	250 - 425 nm
C	38 mm	1.52	250 - 425 nm
D	50 mm	1.50	250 - 425 nm
E	25 mm	1.67	400 - 1000 nm
F	30 mm	1.50	400 - 1000 nm
G	40 mm	1.60	400 - 1000 nm
H	50 mm	1.67	400 - 1000 nm
I	60 mm	1.50	400 - 1000 nm
J	200 mm	2.70	400 - 1000 nm

4.2.1.3 Sensor

The ultra-high speed Photron FASTCAM SA-Z includes a highly light sensitive image sensor (monochrome ISO 50,000) of 1024 x 1024 20 μm square pixels, with 12-bit ADC pixel depth. It provides frame rates up to 2.1 million frames per second (fps) at reduced image resolution. Table 4.4 summarizes the maximum resolution of the Photron FASTCAM SA-Z sensor, depending on the frame rate.

Table 4.4: Photron Fastcam SA-Z

Frame rate	Sensor size ($\mathbf{H} \times \mathbf{V}$)
20000 fps	1024 \times 1024
40000 fps	1024 \times 512
700000 fps	256 \times 56
1000000 fps	256 \times 24
2100000 fps	128 \times 8

4.2.1.4 Photometer and triggering system

The photometer is based on a fast photodiode working under photoconductive mode. It amplifies the optical signal and launches a Transistor - Transistor Logic (TTL) synchronism pulse that triggers the Photron SA-Z camera whenever a



Figure 4.2: GALIUS mechanical housing

threshold in a number of photons is reached. The photometer can either launch a positive or negative TTL pulse with a typical delay of 20 ns. The photometer is very useful to synchronize the Photron SA-Z recording with the initial stage of a spark or lightning and to avoid collapsing the internal buffer of the camera with empty images.

4.2.2 Spectrograph calibration

In order to calibrate GALIUS we followed the steps previously described for calibrating the GRAnada Sprite Spectrograph and Polarimeter (GRASSP) (Passas et al., 2016b) presently in operation for high spectral resolution TLE spectroscopy (Parra-Rojas et al., 2013), (Passas et al., 2014), (Passas et al., 2016a), (Gordillo-Vázquez et al., 2018). The detailed steps followed to calibrate GALIUS are: (1) a distortion correction, to straighten the curved raw spectrum; (2) a wavelength calibration, to assign an absolute wavelength to each pixel of the CMOS; and (3) a flux calibration, to provide the spectral sensitivity of the spectrograph. Distortion correction and wavelength calibration are done whenever a spectrum is recorded; the 22 different instrument functions (one per each configuration of GALIUS) are calculated once a year.

4.2.2.1 Distortion Correction and Wavelength Calibration

We have implemented a software in Python to correct the curvature of the spectrum due to the aberration introduced by the optical elements of GALIUS. We recorded the spectrum of deuterium (for the UV setup) and neon and argon (for the Visible-NIR setup) spectral lamps. Then, we trimmed them so all spectral lines appeared in every row of the spectrum. Then, we identified the corresponding wavelengths by comparing the distances between the spectral lines to the gaps that deuterium, neon and argon spectra show. We measured the deuterium spectrum with a commercial Jobin Yvon Horiba FHR1000 spectrograph and we obtained the Ne and Ar spectral lines from (Kramida et al., 2015). Finally, to straighten the spectrum, we assigned the central pixel of each spectral line to a single wavelength for every row of the spectral image. This software generates a calibration matrix that will be used to correct the distorted spectra recorded

with GALIUS, associating every pixel coordinate of the CMOS to an absolute wavelength. This calibration matrix is calculated every time we perform a new set of measurements.

4.2.2.2 Flux Calibration

We measured the spectral response of the 22 different GALIUS setups.

For the UV setup, we measured with GALIUS the spectral radiance of a deuterium lamp (see Figure 4.3) directly from the bulb at 50 frames per second located at 24.5 cm from the collector lens, measuring in 3 different regions of the beam, and combining these measurements by terms of the median value of images. We repeated the setup and measured the spectral radiance of the same deuterium lamp with a calibrated Jobin Yvon HORIBA FHR1000 spectrometer. In this case we located the optic fiber over 9 different regions of the deuterium beam with a micrometric regulation screw, and we combined these measurements as their median value. Then we proceeded as in (Fantz, 2006). It is worth highlighting that we could not use an integrating sphere since the radiance from the lamp is very weak for the UV spectral range, and the system sensitivity is also very low at these wavelengths. From these calculations we got 4 different instrumental functions.



Figure 4.3: Spectral image of a deuterium lamp recorded with GALIUS for grism R1 using the collector lens D (50 mm focal length).

For the Visible-NIR setups, we repeated the steps defined in (Passas et al., 2016b). We recorded the spectral radiance of a halogen tungsten spectral lamp (QTH) at 50 frames per second located at 60 cm from the collector lens, and

repeated these measurements with the calibrated Jobin Yvon HORIBA FHR1000 spectrometer using the same calibration setup. From these calculations we got 18 different instrumental functions.

Equation 4.1 provides the instrument function of GALIUS for row i of the CMOS, according to the steps defined in Fantz (2006):

$$IF(\lambda, i) = \frac{S_{FHR1000}(\lambda)}{S_{GALIUS}(\lambda, i)} \quad (4.1)$$

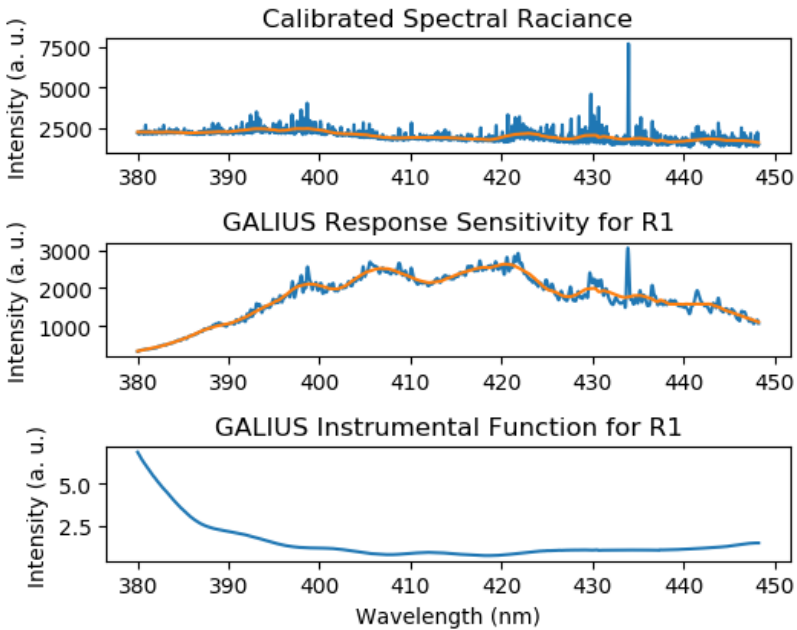


Figure 4.4: Spectral sensitivity of GALIUS for grism R1 using the collector lens D (50 mm focal length) for CMOS row number 16.

As the spectral resolutions of the FHR1000 and GALIUS are different, we could not divide them directly to calculate the spectral sensitivity. To correct this issue we convolved both responses with a gaussian curve so the resulting signals had the same spectral resolution. Figure 4.4 shows the spectral sensitivity of row number 16 for grating R1 with a collector lens of 200 mm focal length.

4.2.3 Spectral resolution

We have estimated the spectral resolution of GALIUS by measuring the full width at half-maximum (FWHM) of different spectral emission lines for each VPH. We also estimated the mean resolving power of the spectrograph as $R = \lambda/\delta\lambda$, with $\delta\lambda$ as the FWHM of a certain spectral emission line. The spectral dispersion (D) and FWHM and R mean values are shown in Table 4.5. The current resolution element is contained in 2.17 to 2.6 pixels average (it changes across field, due to anamorphics and aberrations), which is very close to the Nyquist limit (2 to 2.4 pixels).

Table 4.5: GALIUS spectral features

VPH	D (nm/px)	FWHM (nm)	R
R1	0.1354	0.2945	1409.17
R2	0.3306	0.7530	835.36
R3	0.1483	0.3831	1729.97
R4	0.1481	0.3456	2258.68

4.2.4 Spatial dispersion

We measured the spatial dispersion (XD) of the GALIUS spectrograph for settings F, G, H and J by measuring the spectrum of the Sun reflected on a full Moon, which subtends about 32 ± 3 min of arc from Earth. The number of pixels of this spectrum on the CMOS vary in the spatial dimension depending on the collector lens, being linear the ratio between this number of pixels and the collector lens focal length. We were unable to measure the spectrum the Sun reflected on the Moon with the UV setup due to the weakness of the spectrum at these wavelengths, so we estimated the spatial dispersion assuming linearity.

According to Nyquist criterion, the spatial resolution (XR) is three times the

spectral dispersion. Table 4.6 shows the spatial dispersion (second column) and spatial resolution (third column) for each collector lens (first column).

4.2.5 Stability

We have checked the stability of GALIUS in our laboratory for every VPH by recording the spectrum of the calibration lamps within a time interval of seven hours, and we did not detect any drift in the wavelength. However, we will calibrate in wavelength at the beginning and at the end of a working session to check the stability of the system due to movements during the observation night.

Table 4.6: GALIUS spatial features

Lens	XD (arc sec/px)	XR (arc min)
A	279.91 ± 26.24	14.00 ± 1.31
B	236.84 ± 22.205	11.84 ± 1.11
C	190.06 ± 17.82	9.50 ± 0.89
D	146.62 ± 13.75	7.33 ± 0.69
E	133.29 ± 12.50	6.66 ± 0.62
F	112.78 ± 10.57	5.64 ± 0.53
G	86.25 ± 8.09	4.31 ± 0.4
H	69.82 ± 6.55	3.49 ± 0.33
I	58.65 ± 5.50	2.93 ± 0.27
J	18.10 ± 1.70	0.91 ± 0.08

4.2.6 Spectrograph reliability

In Figure 4.5 we compare two sparks spectra. The blue one is the calibrated spectrum of the light emitted by a 5 cm spark generated with a Whimshurst machine. It was recorded in our laboratory at 84 kfps and 10 μ s exposure time with GALIUS setting of grism R1 combined with lens D. The orange graph corresponds to the calibrated spectrum of the light emitted by a spark produced by a Van der Graaff generator. It was recorded at 100 kfps and approximately 10 μ s exposure

time with a VPH-VIS spectrograph with 0.75 nm spectral resolution and a grating of 1257 lines/mm (Walker, 2015).

Since we are comparing the spectra of two different electrostatic discharges recorded both with two different spectrographs at two different spectral and temporal resolutions, these spectra are, hence, different. Nevertheless, both spectra are coincident in peaks, and their background level seems to follow the same slope, so this comparison confirms the reliability of the wavelength and flux calibration of GALIUS between 380 and 450 nm.

We have confirmed the same reliability for gratings R2, R3 and R4.

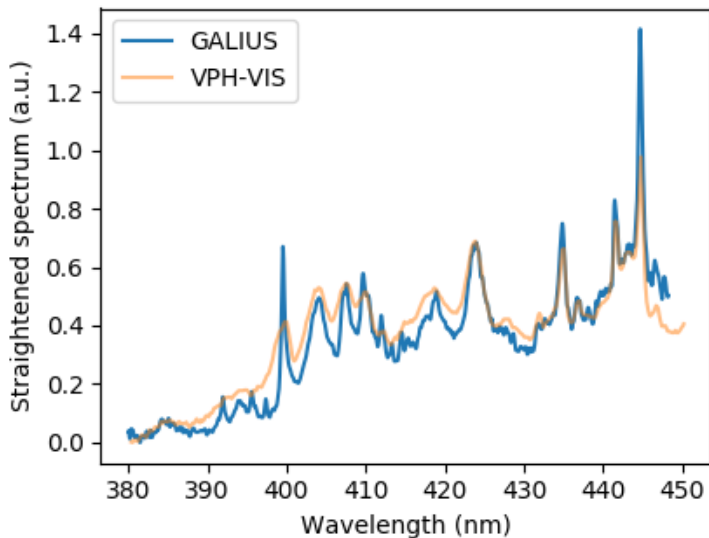


Figure 4.5: Spectrum of a spark produced by a Whimshurst machine measured with GALIUS (blue) R1 grism (0.29 nm spectral resolution). Spectrum of a spark produced by a small Van der Graaf generator measured with a VPH-VIS spectrograph (orange) using a 1257 lines/mm grating with 0.75 nm of spectral resolution (Walker, 2015).

4.3 Conclusions

In this paper we have described the design and development as well as the complete optical characterization of GALIUS, a portable, ground-based ultra fast spectrographic system for the analysis of the spectroscopic signature of lightning and artificial electrostatic discharges at recording speeds up to 2.1 Mfps with spectral resolutions varying from 0.29 nm to 0.76 nm. GALIUS would allow us to remotely estimate physical parameters of the lightning channel, such as the electron density or the gas temperature, among others. It is worth highlighting that GALIUS is currently the fastest spectrograph intended to analyze lightning spectra, improving the temporal resolution of former lightning slit spectrographs by more than 3 times ([Walker and Christian, 2017, 2019](#); [Walker, 2015](#)).

Chapter 5

Sub-microsecond time-resolved spectroscopy

The content in this chapter was published in *Geophysical Research Letters* with title ‘**Submicrosecond spectroscopy of lightning-like discharges: Exploring new time regimes**’.

Authors: **Kieu, T. N.**, Gordillo-Vázquez, F. J., Passas, M., Sánchez, J., Pérez-Invernón, F. J., Luque, A., Montanyá, J. and Christian, H.

Volume **47**, Issue **15**, e2020GL088755

First Published: 29 July 2020

<https://doi.org/10.1029/2020GL088755>

Abstract

Sub-microsecond ($0.476 \mu\text{s}$ per frame with an exposure time of 160 ns) high resolution (0.38 nm) time resolved spectra of laboratory produced lightning-like electrical discharges have been recorded for the first time within the visible spectral

range (645 nm - 665 nm). The spectra were recorded with the GrAnada LIghtning Ultrafast Spectrograph (GALIUS), a high speed imaging spectrograph recently developed for lightning research in the IAA-CSIC. Unprecedented spectral time-dynamics are explored for meter long laboratory electrical discharges produced with a 2.0 MV Marx generator. The maximum electron density and gas temperature measured in a time scale of $\leq 0.50 \mu\text{s}$ (160 ns) were, respectively, $\simeq 10^{18} \text{ cm}^{-3}$ and $\simeq 32000 \text{ K}$. Over pressure in the lightning-like plasma channel, black body dynamics and self-absorption in spectral lines were investigated.

Plain Language Summary

Lightning are extremely rapid and violent atmospheric electricity events taking place inside thunderclouds and between thunderclouds and the ground. Investigation of the fundamental properties of different types of lightning and lightning leaders can help to deepen our understanding on lightning propagation dynamics (stepping) and how lightning can produce high energy pulses of X-ray or pulses of even higher energy (the so-called Terrestrial Gamma-ray Flashes). Time resolved optical emission spectroscopy is an ideal diagnostic technique to remotely study the fast temporal dynamics of lightning. The fastest spectroscopic techniques used to date were able to achieve microsecond time scales. We present the first study exploring sub-microsecond time regimes using the GrAnada LIghtning Ultrafast Spectrograph (GALIUS), a high speed imaging spectrograph recently developed for lightning research at the IAA-CSIC.

5.1 Introduction

Time resolved lightning spectroscopy started in 1962 when [Salanave et al. \(1962\)](#) first developed slitless spectroscopic techniques (time resolved flash spectra) to investigate time-integrated spectra of individual strokes within a lightning flash with time and spectral resolutions of, respectively, 20 ms and about 0.2 nm. The millisecond time scale of Salanave's technique allowed for the first time to spectroscopically monitor return stroke continuing currents ([Salanave, 1971](#)) that were earlier proposed ([McEachron and Hagenguth, 1942](#)) to produce forest fires, which was confirmed in 1967 ([Fuquay et al., 1967](#)).

The first successful attempt to time resolve the spectra of individual return strokes in cloud to ground (CG) lightning was not performed with spectrometers but with a set of narrow band interference filters (of selected wavelengths) and photomultiplier tubes with 5 μs time resolution ([Kridler, 1965a,b](#)). [Kridler \(1974\)](#) carried out, using a silicon photodiode (with flat spectral response between 400 nm and 1000 nm), the highest time resolution (0.2 μs) study to date of the relative light intensities of five leader steps immediately before a return stroke in CG lightning. [Kridler \(1974\)](#) was able to capture the leader stepping time dynamics observing that a typical step rises from zero to peak in about 1 μs , falls to half peak in 1 to 2 μs , and then decays slowly until next step occurs ([Kridler, 1974](#)), ([Orville, 1977](#)).

In a series of papers published between 1966 ([Orville, 1966a,b](#)) and 1968 ([Orville, 1968a,b,c,d](#)), Orville introduced high speed slitless spectroscopic techniques based on photographic recordings able to achieve time resolutions between 2 μs and 5 μs with good spectral resolution (1 nm). This technique allowed time resolved spectroscopic investigations of return strokes ([Orville, 1968a,b](#)) and

stepped leaders (Orville, 1968d) - in the range 560 nm to 660 nm - including a quantitative analysis to derive the electron temperature and electron density by methods first proposed in 1963 (Prueitt, 1963) and 1964 (Uman and Orville, 1964), respectively. Later in 1975, dart leaders preceding subsequent return strokes were also spectroscopically investigated with a time resolution of 10 μ s (with exposure time of $\simeq 9 \mu$ s) in the range from 395 to 510 nm (Orville, 1975). Both the return stroke and stepped leader spectra exhibited neutral and singly ionized atom optical emissions but neither molecular emissions nor doubly ionized atom emissions were detected (Orville, 1968a,d). The characteristic stepping in the leader was only exhibited in singly ionized emissions within the 528 nm to 680 nm range of spectra recorded with 20 μ s resolution (Orville, 1968d). Time-resolved (10 μ s resolution) spectra of dart leaders were found to be dominated by singly ionized emissions within the 399 nm to 501 nm spectral range (Orville, 1975).

After the introduction of CCD and CMOS technology in, respectively, the 1980s and 1990s, a new generation of fast and very sensitive camera sensors became available. The availability of new fast and reliable sensors, together with the perfection of artificial initiation of lightning, first demonstrated in 1967 (Newman et al., 1967), led to a renovated interest for lightning spectroscopy research. High time resolution lightning spectroscopy investigations carried out during the second decade of the XXI century have explored spectral features of lightning return strokes (Wang et al., 2014), stepped leaders (Warner et al., 2011) and dart lightning leaders (Cen et al., 2015) within a time scale of 100 μ s or longer. It is interesting to note that the modern works by Warner et al. (2011) and Cen et al. (2015) - with expanded spectral ranges of, respectively, 600 nm - 1050 nm and 400 nm - 1000 nm - were only the second ones on high speed spectroscopy of stepped and dart leaders after Orville's 1968 and 1975 papers with narrower

spectral ranges.

Two recent papers (Walker and Christian, 2017, 2019) discussed the first time resolved spectra of triggered lightning including high speed spectroscopic recordings of dart leaders, dart stepped leaders and return strokes evaluated in two spectral ranges, from 370 nm to 630 nm and from 630 nm to 890 nm with a spectral dispersion of 0.26 nm/pixel (spectral resolution between 0.52 nm and 0.65 nm). In these studies triggered lightning spectra were recorded with 673 kfps (1.5 μ s per frame) with exposure times between 0.7 and 1.47 μ s. Some new doubly ionized line emissions were found in the 370 nm to 650 nm range but not in the spectral range from 650 nm to 850 nm.

The first sub-microsecond (0.476 μ s per frame with an exposure time of 0.16 μ s) resolved slit spectra with high spectral resolution (0.38 nm) of meter long lightning-like discharges are presented here. Unprecedented spectral time-dynamics are shown for lightning-like discharges produced with two different operation modes (lightning (LI) and switching (SI) impulse) of a 2 MV Marx generator. Quantitative analysis of recorded spectra led to measured values of the electron concentration and gas temperature comparable to those found in real lightning due to the extremely high temporal resolution and sensitivity of GALIUS. In addition, our study quantifies the overpressure in the lightning-like channel, the self-absorption in ionic spectral lines and the position and speed of the hydrodynamic shock front produced right after electric breakdown leading to lightning-like discharges. We have compared our measured spectra with synthetic spectra calculated for equilibrium air plasmas at atmospheric pressure and have found partial agreement. This, together with the high ($> 4 \text{ km s}^{-1}$) shock front speeds computed lead us to consider possible slight disruption of equilibrium right behind the shock front in post-trigger sub- μ s times.

5.2 Instrumentation

The investigations presented here have been carried out with an very fast (2.1 Mfps or $0.476 \mu\text{s}$ per frame with an exposure time of 160 ns) and high spectral resolution (between 0.29 nm and 0.75 nm depending on the grating used) spectrograph named GrAnada LIghtning Ultrafast Spectrograph (GALIUS) recently developed by the IAA-CSIC atmospheric electricity group (Passas et al., 2019). A total of 22 possible configurations can be set up with GALIUS, combining 10 interchangeable collector lenses (with focal lengths ranging from 25 mm to 200 mm) with two different collimator lenses (105 mm with F#4.5 and 50 mm with F#1.2 focal lengths for, respectively, the UV and visible-NIR ranges) and four interchangeable volume-phase holographic (VPH) gratings for spectral ranges from the near UV (380 nm) to the near IR (850 nm) (Passas et al., 2019).

GALIUS is a compact device that is housed in a portable aluminum box of $1100 \text{ mm} \times 380 \text{ mm} \times 230 \text{ mm}$, which can be bent in elevation from 0° to 50° due to a linear actuator and a telescopic mechanism attached on its fixed base. GALIUS can operate in slit or slitless mode and incorporates a very high-speed Photron FASTCAM SA-Z camera with a high light-sensitive image CMOS sensor (monochrome ISO 50000) of $1024 \times 1024 \text{ } 20 \mu\text{m}$ square pixels, with 12-bit ADC pixel depth. Finally, GALIUS incorporates a fast photodiode based photometer for triggering when a threshold of photons is reached (Passas et al 2019).

For the results presented here GALIUS is set up in slit mode ($50 \mu\text{m} \times 3 \text{ mm}$) and operated at 2.1 Mfps using collimator and collector lenses of, respectively, 50 mm (F#1.2) and 30 mm (F#1.5) focal lengths, and a grism with a diffraction grating of 1855 lines/mm with its central wavelenth (CWL) in $\simeq 657 \text{ nm}$ and a spectral resolution of 0.38 nm.

5.3 Experimental Setup

During the first half of 2019, a number of experiments were carried with small (several centimeters) sparks and meter long lightning-like discharges produced with, respectively, an electrostatic generator at the IAA-CSIC atmospheric electricity laboratory in Granada (Spain, 940 hPa) and with a 2.0 MV Marx generator at DENA in Terrassa (Spain, 1010 hPa).

Two discharge impulse modes were used at DENA with a maximum applied generator voltage of +0.8 MV and a distance between electrodes of $\simeq 1$ m. The tip of the grounded electrode was 0.2 m above the floor. GALIUS was pointed to the discharge region just below the upper electrode. The voltage was recorded by a calibrated capacitive voltage divider connected to high-speed digital oscilloscopes. Faraday cages and electromagnetic compatible (EMC) cabinets assured protection against electromagnetic interference.

Each discharge mode has its own positive voltage waveforms (see supporting information 5.8) with distinct rise times. The voltage of the Switching Impulse (SI) was adjusted with a rise time of $\simeq 100 \mu\text{s}$ exhibiting a fast ($\simeq 0.5 \mu\text{s}$) breakdown time. However, the characteristic voltage curve of the Lightning Impulse (LI) mode shows a fast ($\simeq 0.5 \mu\text{s}$) rise time followed by a short plateau of $\simeq 2\text{-}3 \mu\text{s}$ and the fast ($\simeq 0.5 \mu\text{s}$) breakdown time. The currents of the SI and LI modes are both characterized by fast rise times ($\simeq 0.5 \mu\text{s}$) but with very different decay times and peak currents (I_{peak}) of, respectively, $\simeq 0.5 \mu\text{s}$ and $\simeq 0.125$ kA (for the SI mode) and tens of μs and $\simeq 2.5$ kA (for the LI mode). The applied peak voltage and current used to generate the small (4 cm) spark discharge have values of $\simeq -55$ kV and $\simeq 0.350$ kA.

The total injected electric energies in each discharge, calculated from their

voltage and current, are 81 J (for SI mode), 684 J (for LI mode) and 1.2 J (for the small spark). Figures 5.4, 5.5, and 5.6 in the supporting information 5.8 show the typical voltage and current curve shapes for the discharges investigated in this study.

5.4 Time Resolved Spectra

In order to interpret the spectra recorded by GALIUS we have generated synthetic spectra (shown in the supporting information 5.8) based on equilibrium calculations for atmospheric pressure thermal plasmas (see section 6). Calculated spectra include all possible lines of atoms, molecules, singly and doubly ionized ions that can appear in the 645 - 665 nm spectral range investigated in this study (Kramida et al., 2015). Stark broadening of nonhydrogenic (Bekefi, 1976) and hydrogenic lines (Griem, 1964) are included and convolved with instrumental broadening. In particular, synthetic spectra show the expected relative importance of the different atomic, ionic and molecular spectral features as a function of the lightning-like channel temperature and serve as a guidance for comparison with the measured spectra.

The 645 - 665 nm lightning-like synthetic spectra in the supporting information 5.8 show the presence of six N I neutral lines (648.17 nm, 648.27 nm, 648.37 nm, 648.48 nm, 649.12 nm and 649.95 nm), two O I neutral lines (645.44 nm and 645.59 nm) and one H I neutral line (656.27 nm, the so-called H_α line). For the ions we see two singly ionized N II lines (648.20 nm and 661.05 nm), four singly ionized O II lines (649.58 nm, 662.73 nm and two lines at 656.52 nm and 657.11 nm close to the H_α line) and two weak N III doubly ionized emission lines (645.41 nm and 646.70 nm) not previously detected (Walker and Christian,

2017). Synthetic spectra also predict the presence of a line at 660.8 nm associated to a vibrational transition ($v' = 6 \rightarrow v'' = 3$) of the first positive system (FPS) of molecular nitrogen (N_2). This molecular spectral feature would only be detectable for temperatures below 12000 K (see Figure 5.13 in supporting information 5.8). The spectra do not show contamination from the metal electrodes.

Figure 5.1(a, b) and Figure 5.1(c, d) show unprecedented spectral time-dynamics for meter long lightning-like electrical discharges generated with, respectively, the SI and LI discharge modes of a Marx generator. As shown in Figure 5.1(a, c) the SI and LI discharge spectra last for about 12 μs and 60 μs , respectively. Figure 5.1(b, d) show different times of the SI and LI discharge spectra where distinct spectral features are visible. The time resolved spectra of a small (several centimeters long) spark produced with an electrostatic generator is shown in Figure 5.1(e, f).

Most recorded spectra exhibit a continuum emission that could be due to different types of continuous radiation sources (Uman, 1963). We found that the contribution of Bremsstrahlung radiation to the continuum is negligible for the measured temperatures and electron densities. Recombination and attachment continuum radiation are of the same order of magnitude as Bremsstrahlung radiation and cyclotron continuum radiation is unlikely in lightning (Uman, 1963). Thus, by elimination, this leaves black body radiation as the most probable source of the continuum emission present in the measured spectra. The inclusion of black body radiation into the calculation of synthetic spectra shows that the detected continuum emission exhibits a shape and magnitude similar to a simulated black body core at 7000 K (see supporting information 5.8). The dynamics of the black body continuum reveals that it is almost zero or very small at pre-trigger times (for SI and LI discharges, see Figure 5.1(b, d)). Then - at early times after triggering

- it reaches its larger value and afterwards it mildly decreases as time progresses while the lightning-like channel fades away and reaches ambient pressure.

Three temporal regimes with their own spectral features are clearly distinguishable in the SI and LI lightning-like discharges and in the small spark spectra. First, at early times ($\leq 1 \mu\text{s}$) ionic emissions dominate. In particular, we can distinguish the 648.20 nm and 661.05 nm singly ionized N II lines. Less visible, but also present in the sub- μs time scale of the SI discharge in Figure 5.1(b) and the small spark in Figure 5.1(f) spectra, are two doubly ionized N III lines at 646.70 nm (more noticeable) and 646.41 nm (less noticeable) to the left of the 648.20 N II ion line (see also synthetic spectra in the supporting information 5.8). Finally, very soon after triggering (0.356 μs and 0.510 μs in, respectively, the SI and spark spectra) we notice that, while the H_α line is not yet clearly emerged, there are two very small humps due to two singly ionized O II lines emitting at 656.52 nm and 657.11 nm. These two O II lines - hardly distinguishable in the measured spectra - are a bit better appreciated in the synthetic spectra at 32000 K and 33000 K (see Figures 5.14 and 5.16 in the supporting information 5.8).

The second temporal regime starts after $\simeq 1 \mu\text{s}$ and lasts up to $\simeq 2 \mu\text{s}$ (in the SI and small spark spectra) and up to $\simeq 10 \mu\text{s}$ (in the LI spectra). Here the H_α line is clearly the dominant spectral feature but in concurrence with two N II ion lines at 648.20 nm and 661.05 nm that softly disappear as time progresses.

Finally, the third temporal regime begins after $\simeq 2 \mu\text{s}$ (in the SI and small spark spectra) and after $\simeq 10 \mu\text{s}$ (in the LI spectra). This last regime is characterized by the complete prevalence of the H_α line and the replacement of the N II ion line at 648.20 nm by a weak neutral N I emission line at 648.27 nm. The H_α line is the last feature in disappearing at $\simeq 4 \mu\text{s}$ (small spark), at $\simeq 12 \mu\text{s}$ (SI discharge) and at $\simeq 60 \mu\text{s}$ (LI discharge), respectively.

An inspection to the spectra shown in Figure 5.1 indicates that neither the singly ionized N II (648.20 nm and 661.05 nm) lines nor the H_α line are self-reversed (causing a central dip in the line). Self-reversion of spectral lines is a manifestation of strong self-absorption and typically occurs in strong resonance lines (involving the ground energy level) and in inhomogeneous (non uniform) optically thick plasmas. The central dip in self-reversed lines is due to the cold absorbing atoms and / or ions from the outer regions of the lightning-like channel. So, in a first approximation, we can conclude that the lightning-like channel of the discharges investigated in this study is approximately homogenous. In most cases, however, self-absorption produces a height reduction and growth of the spectral line widths that might not be well distinguished from the shape of the different lines in the spectrum (El Sherbini et al., 2005).

Self-absorption can be important for atomic / ionic resonance lines, lines with low excitation energies of upper levels and lines with high transition probabilities. We have computed the self absorption (SA) coefficient of the two single ionized N II lines (648.20 nm and 661.05 nm) appearing in our spectra as a function of the time (see Figure 5.20 in the supporting information 5.8). For the meter long discharges we found that the SA coefficient grows towards 1 (complete optically thin) as the lightning-like channel expands and the channel over pressure returns to ambient pressure (see Figures 5.17 - 5.20 in the supporting information). At pre-trigger times (only recorded for the SI mode, see Figure 5.20(a) when the channel pressure is nearly ambient SA is found to be close to 1. The lack of pre-trigger times for the LI mode and the small spark prevents SA from exhibiting higher values at the beginning. The estimated SA coefficients refer to both the core channel and the shock front.

5.5 Electron Density and Temperature

5.5.1 Electron Density

For electron densities above $\simeq 10^{16} \text{ cm}^{-3}$, the broadening of spectral lines is controlled by the Stark effect caused by the interaction of charged particles (ions) and emitting atoms within the lightning and/or lightning-like air plasma. Thus we use the Stark broadening of spectral lines to derive the electron density. This method has the advantage of being independent of assumptions about the equilibrium state of the air plasma.

In general, plasma diagnostics using Stark broadened line profiles considers the full width at half maximum (FWHM) of the line shape as the relevant parameter related to the electron density. However, it is well known that ion dynamics can significantly modify both the width and the shape of certain spectral lines (Gigosos et al., 2003). This effect is especially important for the H_α and H_γ though it is nearly negligible for the H_β line (Nikiforov et al., 2015). Therefore, as an alternative to the FWHM of the H_α , we evaluate the full width at half area (FWHA) of the H_α line. Thus, when evaluating the H_α line, the FWHA can be considered a more appropriate method for the diagnostics of the electron density in electric discharges forming thermal lightning-like plasmas. The electron concentration is obtained by (Gigosos et al., 2003), (Nikiforov et al., 2015):

$$N_e = 10^{17} \times \left(\frac{FWHA}{1.098} \right)^{1.47135} \text{ cm}^{-3}. \quad (5.1)$$

We use the bootstrap method to estimate the error of the FWHA in a single measurement. This allows to derive the error in the electron density as obtained with equation (5.1). The key feature of the bootstrap method is subsampling the data with replacement (i.e. if we have N datapoints, we select among them N

points allowing for repetition). In our case we could also drop the repeated values since they do not contribute to the integral we need to calculate to obtain the FWHM (Gigosos et al., 2003).

Figure 5.2(a)-(b) shows the electron density for, respectively, the meter long SI (red dots) and LI (green dots) discharges and for the short (centimeters) spark (blue dots). No electron density could be retrieved at $-0.120 \mu\text{s}$ and $0.000 \mu\text{s}$ (trigger time) for, respectively, the SI and LI discharges due to the negligible H_α signal. The maximum electron density ($\simeq 10^{18} \text{ cm}^{-3}$) is measured in the LI discharge. The measured electron densities are comparable to those found in natural return strokes (Orville, 1968b) and triggered lightning return strokes with peak currents of 8.1 kA (Walker and Christian, 2019) due to the high temporal resolution and sensitivity of GALIUS.

5.5.2 Electron Temperature

To calculate the electron temperature from the time resolved spectra of lightning-like discharges used in this work, we will initially assume the criteria previously established by Prueitt (1963) and Uman (1969a), and also recently used by Walker and Christian (2019) for deriving the electron temperature in triggered lightning. In particular, we consider that (a) the channel of the lightning-like discharge is optically thin, (b) the temperature is relatively uniform along the lightning-like channel radial cross section and (c) that thermal equilibrium controls the concentration of the different atoms and ion energy levels emitting light due to spontaneous radiative deexcitation, that is, the density of excited atoms and ions follow Boltzmann's law. We also assume that local thermal equilibrium (LTE) applies so that the derived electron temperature equals the gas temperature.

The electron temperature is calculated from the intensity ratio of the 648.20

nm and 661.05 nm N II ion lines assuming that the corresponding emitting energy levels are populated following Boltzmann's equilibrium law. The estimation of the error in the electron temperature is evaluated with equation (11) in Walker and Christian (2019) that depends on the uncertainties in the tabulated Einstein coefficients (Kramida et al., 2015) and in the intensity ratio. The uncertainty in the intensity ratio is calculated using the bootstrap method also adopted above to quantify the error in the electron density.

Figure 5.2(c) shows the temperatures for, respectively, the meter long SI (red dots) and LI (green dots) discharges and for the small spark (blue dots). The three discharges analysed exhibit almost the same maximum temperature of $\simeq 32000$ K. The LI discharge (with a peak current of 2.5 kA) is characterized by exhibiting the lowest measured temperatures of $\simeq 16000$ K (after $\simeq 10 \mu\text{s}$). The characteristic time scales of the measured temperatures seem to be connected to the decay times of the currents producing the investigated discharges (tens of μs for the LI and $\simeq 1 \mu\text{s}$ for the SI and the small spark). However, the maximum values of the measured temperatures seem to be more related with the similar fast rise times ($\leq 0.5 \mu\text{s}$) of the currents than with the different current peak values. The measured electron temperatures are very similar to those found in natural return strokes (Orville, 1968b) and triggered lightning return strokes with peak currents of 8.1 kA (Walker and Christian, 2019).

5.6 Exploring Overpressure and Equilibrium Conditions in the Lightning-like Channel

The equilibrium (LTE) composition of atmospheric pressure lightning-like air plasmas (78 % N₂ and 22 % O₂) is calculated (see Figures 5.7 - 5.10 in the supporting information 5.8) in order to interpret the different features found in the time

resolved spectra of this work and to quantify possible departure from equilibrium.

The equilibrium calculations are performed in the temperature range 1000 - 35000 K with a method based upon the mass action law and the chemical base concept (Godin and Trépanier, 2004), (Teulet et al., 2009) and assuming a relative humidity (RH) of 50 % that corresponds to the ambient RH measured in the laboratory during experiments. The chemical species considered were 14 atomic, 24 diatomic and 44 polyatomic species including electrons, negative ions and single and double positive ions. Internal partition functions were also calculated for atoms, diatomic and polyatomic molecules as well as for positive and negative ions.

The comparison between the calculated equilibrium and the measured electron densities is shown in Figure 5.3(a-c) for the LI and SI discharge modes and for the small spark. Figure 5.3 also shows the variation in time of the magnitude $\delta_p = N_e^{exp} / N_e^{LTE, 1 atm}$ quantifying the over pressure in the discharge channel (while equilibrium is assumed). The values of δ_p change between maxima of $\simeq 8$ (for LI), $\simeq 4.5$ (for SI) and $\simeq 3.5$ (for the small spark) in the post-trigger sub- μs time scale and minima of roughly $\simeq 2$ (for LI and SI) at $\simeq 10 \mu s$ (for LI) and at $\simeq 2.73 \mu s$ (for SI), and $\simeq 1$ (for the small spark) at $\simeq 2.41 \mu s$.

The comparison of the calculated (equilibrium-based at 1 atm) spectra and measured time-resolved spectra (see Figure 5.14 through 5.16 in supporting information 5.8) reveals that the black body radiation is negligible (Figure 5.14) or very weak (Figure 5.15) in pre-trigger times. This is very well illustrated in Figure 5.14 where synthetic and measured spectra with no black body (very close to optically thin conditions, see Figures 5.20(a) in supporting information) nicely agree at $-0.120 \mu s$ suggesting that the discharge channel overpressure is still very small and that the electron density in the plasma channel would be very close to

the equilibrium electron density at 1 atm (used to compute the synthetic spectra). Interestingly, the black body continuum suddenly appears at $0.362 \mu\text{s}$ (see Figure 5.14), electrons mainly cause overpressure resulting in an optically thicker plasma channel which measured spectra do not agree with the calculated equilibrium spectra at ambient pressure. We think that this disagreement is mainly due to the fact that the very high speed recorded spectra include light emissions from both the hot core air plasma channel (kept at a lower gas density than ambient) and the hot and overpressure shock front. Right behind the shock front thermal nonequilibrium (different values of translational, vibrational and electronic temperatures) can occur that could also cause disruption of the Boltzmann equilibrium distribution for sufficiently high shock front speeds as the ones estimated here (Kadochnikov and Arsentiev, 2018).

The overpressure (and the black body radiation) gradually disappears at $\simeq 2.26 \mu\text{s}$ (see Figure 5.3(b)) and the measured and calculated spectra start to exhibit agreement (see Figure 5.14). Note that, as shown in Figure 5.3(b), $\delta_p \simeq 2.1$ and $\simeq 2.0$ for $2.260 \mu\text{s}$ and $2.736 \mu\text{s}$ (spectra not shown), respectively. The recovery of ambient pressure in the lightning-like plasma channel is more evident at $2.414 \mu\text{s}$ in the case of the small spark discharge (see Figure 5.16) where $\delta_p \simeq 1.0$ (see Figure 5.3(c)).

Out of the three conditions considered to estimate the temperature in a lightning-like channel, we have investigated two of them (optical thickness and equilibrium). We found that the lightning-like plasma for pre-trigger times (only illustrated for the 1 meter long SI mode, see Figure 5.20(a)) is close to optically thin and follows Boltzmann equilibrium at 1 atm (see Figure 5.3(b)). However, very soon ($\leq 0.5 \mu\text{s}$), it becomes optically thicker and an over pressure shock front is formed moving outwards very fast. Considering the ambient conditions

(RH and air mass density) during our experiments and the total injected electric energy for each investigated discharge (1.2 J, 81 J and 684 J for the small spark, the SI and LI meter long discharges, respectively) we have estimated (see text in supporting information and Figures 5.17 - 5.19) the approximate position (R) and speed (U) of the hydrodynamic shock front resulting from the solution of the Rankine-Hugoniot equations to evaluate the discrete changes in the mass density, pressure and velocity across the shock front produced after electrical breakdown (Zahn et al., 1982).

The plasma channel gradually returns to optically thin and close to ambient pressure conditions in $\leq 3 \mu\text{s}$ (for SI meter long and small spark discharges) or within several tens of μs (for LI meter long discharges). The possible non-equilibrium behind the rapidly moving shock front, the over pressure and the optical thickness could affect the measurement procedure employed to derive the “temperature” or characteristic energy in the lightning-like channel (see Figure 5.2(c)) and could lead to their underestimation.

5.7 Summary and Conclusions

Sub- μs high resolution time resolved spectra of laboratory produced lightning-like electrical discharges have been recorded for the first time within the visible spectral range (645 nm - 665 nm). Unprecedented spectral time-dynamics are explored for meter long and small laboratory electrical discharges.

The maximum electron density and gas temperature measured in a time scale of $\leq 0.50 \mu\text{s}$ (160 ns exposure time) were $\simeq 10^{18} \text{ cm}^{-3}$ and $\simeq 32000 \text{ K}$, respectively.

Overpressure, equilibrium and black body dynamics of the lightning-like plasma channel were investigated. We have computed fast ($> 4 \text{ km s}^{-1}$) propagation

speeds for the discharge shock front that, as discussed in previous works (Kadochnikov and Arsentiev, 2018), could lead to the disruption of the Boltzmann equilibrium right behind the shock front in post-trigger sub- μs times. However, Boltzmann equilibrium was found to be kept at very early pre-trigger times (where synthetic spectra based on equilibrium calculations at 1 atm nicely agree with measured spectra) and, depending on the discharge, at “late” times such as $\simeq 2 \mu\text{s}$ (SI, small spark) or $\simeq 10 \mu\text{s}$ (LI) after triggering when the shock front speed has considerably decreased and the pressure inside the discharge channel approaches the ambient one.

Analysis of the temporal evolution of the black body radiation and of the self-absorption coefficient suggest that meter long discharges and short spark discharges behave differently with respect to the optical thickness of the spectral lines. The optical thickness of meter long discharges is influenced by its over pressure. Close to optically thin lines are found for near ambient pressure channels (occurring at pre-trigger and late times). For short sparks, however, the optical thickness of spectral lines seems to change little with time.

A possible slight non-equilibrium just behind the shock wave and a transient partial optical thickness could affect the assumptions underlying the procedure employed to derive the “temperature” in the lightning-like channel and might cause their underestimation.

Future studies will be conducted to investigate real lightning dynamics using sub-microsecond time resolved spectroscopy with GALIUS.

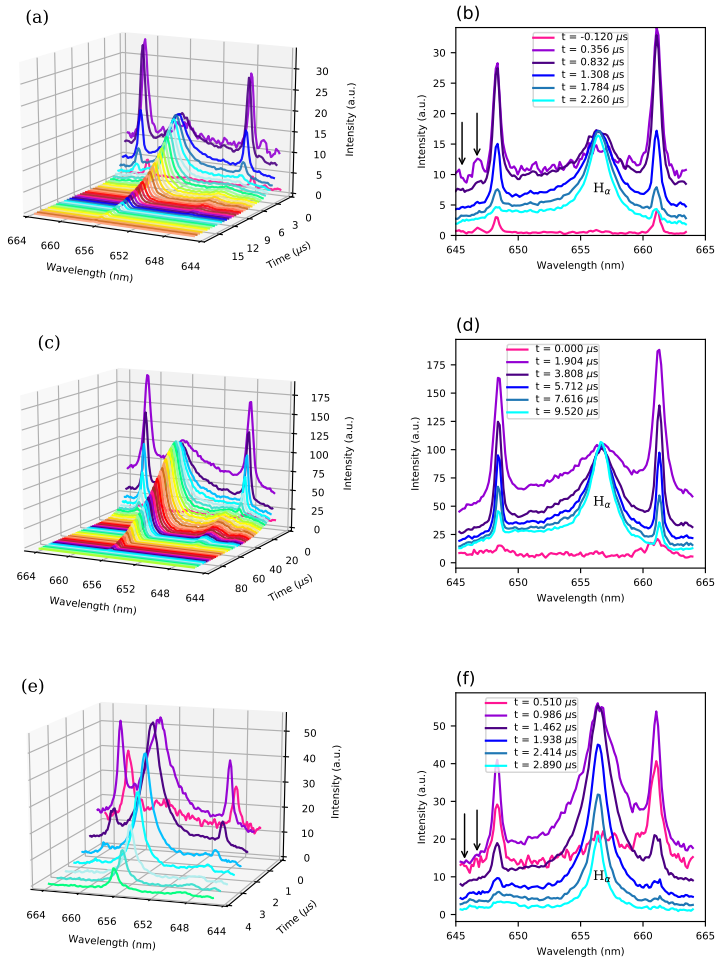


Figure 5.1: Time resolved spectra of meter long lightning-like discharges produced with the Switching Impulse (SI) mode (a) - (b) and Lightning Impulse (LI) mode (c) - (d) of a Marx generator. Panels (e) - (f) show time resolved spectra of a 4 cm long spark produced with a small electrostatic generator. The peak intensities and voltages reached in these discharges are 0.125 kA and 0.8 MV for SI mode, 3 kA and 0.8 MV for LI mode and 0.350 kA and -55.0 kV for the electrostatic spark, respectively. The strong intensities shown correspond to two singly ionized N II lines at 648.20 nm and 661.05 nm and to the H_{α} line at 656.27 nm. The panels in the right column show the six initial times for the SI (b) and electrostatic discharges (f), and six selected (not consecutive) instants in the temporal evolution of LI mode discharges (d). The weak doubly ionized N III emission lines at 645.41 nm and 646.70 nm marked with arrows can be seen in the very early (sub- μ s) times of spectra in panels (b) and (f). The weak N I neutral line at 648.27 nm is seen (as a soft hump) in the late times of panels (a), (c) and (e).

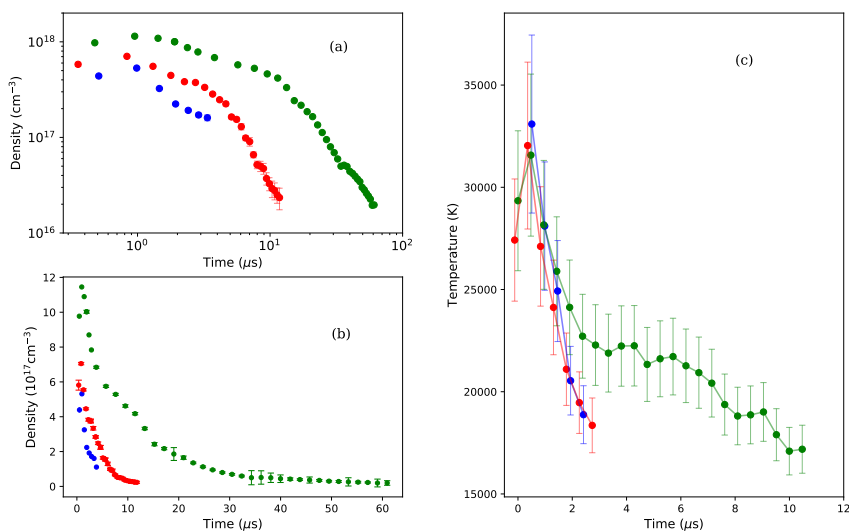


Figure 5.2: Temporal evolution of the measured electron density in logarithmic (a) and linear (b) scale, and temperature (c) for meter long lightning-like discharges (SI, red dots and LI, green dots), and small spark (blue dots) discharges. Due to very weak H_{α} signal, the electron density could not be measured at $-0.120 \mu\text{s}$ (for the SI mode discharge) and at $0.000 \mu\text{s}$ (for the LI mode discharge). Note that the measured electron (gas) temperature values and time scale for the LI mode discharge (green dots in panel (c)) are very similar to those reported in natural lightning return strokes (Orville, 1968b) and to those recently reported by Walker and Christian (2019) in triggered lightning return strokes with peak currents of 8.1 kA.

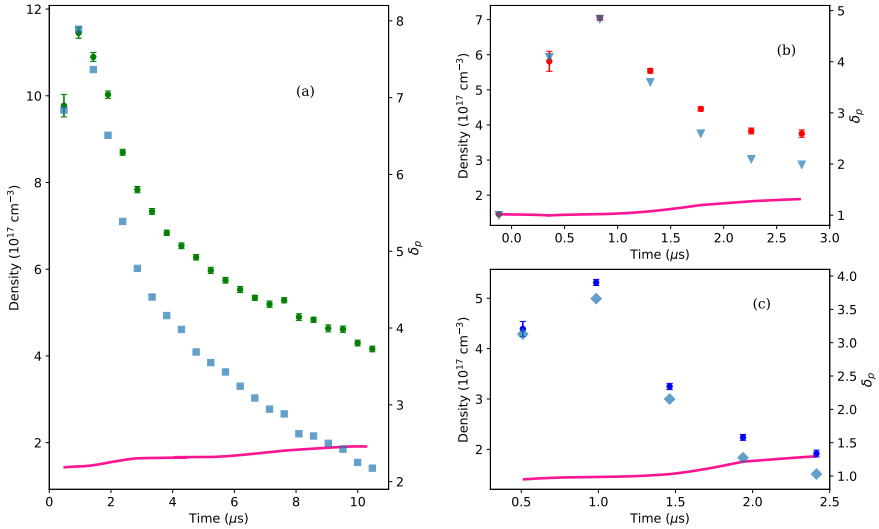


Figure 5.3: Time dependence of the measured electron density (green, red and blue dots), calculated equilibrium electron densities (pink solid line) at 1 atm using the measured temperatures and δ_p (square, triangles and diamond symbols) to quantify overpressure in the discharge channel with respect to ambient pressure ($\delta_p = 1$) for (a) LI mode and (b) SI mode of meter long lightning-like discharges, and for (c) a small spark discharge. Note that the measured electron density and the channel overpressure for the LI mode discharge (panel (a)) exhibit very similar values to those reported in natural lightning return strokes (Orville, 1968b) and to those recently reported by Walker and Christian (2019) in triggered lightning return strokes with peak currents of 8.1 kA. Regarding panel (b) time $-0.120 \mu\text{s}$ (electron density could not be measured by spectroscopic means at this particular time), note that the SI measured and synthetic spectra agree very well at $-0.120 \mu\text{s}$ (see Figure 5.14 at 27000 K and Figures 5.17 in supporting information 5.8). This suggests an equilibrium (at 1 atm) electron density at the pre-trigger time of $-0.120 \mu\text{s}$ for the SI discharge shown in (b), which explains why we have included a symbol (diamond) at $-0.120 \mu\text{s}$ for the electron density corresponding to equilibrium air at 1 atm.

5.8 Supporting Information

Introduction

We include here the shape of the typical voltages and currents used to generate the different lightning-like discharges investigated in this study (Figure 5.4 through 5.6). We also provide the equilibrium composition in meter long (Switching (SI) and Lightning (LI) Impulse modes of a Marx generator) and small (centimeter long) air thermal plasmas at 1 atm for the times for which electron density and temperature are measured (Figure 5.7 through 5.10). We present calculated synthetic spectra of lightning-like discharges assuming equilibrium composition at 1 atm (Figures 5.11 through 5.13) and compare synthetic with measured spectra of the SI, LI and small spark discharges (Figures 5.14 through 5.16). Figures 5.17 through 5.19 show the δ_p factor, the total pressure and the partial pressures due to electrons, ions and neutrals together with an estimation of the shock front position and velocity as a function of time for meter long discharges (SI and LI) and for a small (4 cm long) spark discharge. Figure 5.20 shows the self-absorption (SA) coefficient ($0 \leq SA \leq 1$) of the 647 nm and 661 nm singly ionized N II lines as a function of time. Figures 5.21 and 5.22 show the typical shape of the H_α line and of the 647 nm and 661 nm ion lines to illustrate the procedures followed to derive the electron density and temperature. Finally, Figure 5.23 shows a raw image spectrum of the LI mode of the Marx generator. Some details of the equilibrium, black body continuum (background) dynamics, synthetic spectra calculations and the procedure followed to derive a line spectrum from a raw image spectrum are presented in Text S1.

Text S1.

Text S1

The measured voltages and currents used to generate the different lightning-like discharges investigated in this study are shown in Figure 5.4, Figure 5.5 and Figure 5.6. The camera buffer allowed us to capture images of the discharge before the trigger takes place, although this was not always possible.

Local thermal equilibrium (LTE) composition of atmospheric pressure lightning-like air plasmas (78 % N₂ and 22 % O₂) is calculated and shown here in order to interpret the different features found in the measured time resolved spectra of this work and to quantify possible departures of the measured electron densities from equilibrium. The equilibrium calculations are performed in the temperature range 1000 K - 35000 K with a method based upon the mass action law and the chemical base concept (Godin and Trépanier, 2004), (Teulet et al., 2009). We have assumed a relative humidity (RH) of 50 % that corresponds to the ambient RH measured in the laboratory during experiments. The chemical species considered were 14 atomic, 24 diatomic and 44 polyatomic species including electrons, negative ions and single and double positive ions. Internal partition functions were also calculated for atoms, diatomic and polyatomic molecules as well as for positive and negative ions.

Comparisons between measured electron densities and equilibrium concentration of electrons are shown in Figure 5.7 (SI meter long discharge), Figure 5.8 (LI meter long discharge) and Figure 5.9 (small - 4 cm - spark). Figure 5.7 - Figure 5.9 also present equilibrium concentrations at 1 atm of key neutral and ionic species in the humid air plasma channel formed by different lightning-like discharges in the range of measured temperatures ($\simeq 17000$ K - $\simeq 30000$ K). Figure 5.10 shows calculated equilibrium concentration for a selected number of species in the entire

range of temperatures considered in the calculations (1000 K - 35000 K). The concentration of species like nitrogen oxide (NO) reaches its maximum at $\simeq 3300$ K, that is, well below the minimum measured temperature.

Synthetic spectra of atmospheric pressure LTE plasmas of humid air at 1 atm are shown in Figure 5.11 (35000 K - 30000 K), Figure 5.12 (29000 K - 18000 K) and Figure 5.13 (16000 K - 8000 K). We have calculated synthetic spectra considering the more abundant neutral atomic (H I, N I, O I) and molecular (N_2) species and atomic ion species (N II, NIII, O II, O III). We have assumed Boltzmann equilibrium for the electronically excited atomic and molecular states and for the vibrational levels of the molecular N_2 included in the spectra. Synthetic spectra include all the tabulated observed optical transitions of the considered neutral atoms and atomic ions (Kramida et al., 2015). For N_2 , the synthetic spectra include the first positive system (FPS) in the visible - near-infrared (500 - 1500 nm), second positive system (SPS) in the near-ultraviolet - blue (250 - 450 nm) and the Lyman Birge Hopfield system in the vacuum ultraviolet (120 - 230 nm).

The emission intensity of a spectral line from an upper energy level i to a lower energy level j can be written as $I_{ij} = (1/4\pi)h\nu_{ij}A_{ij}N_i$, where h is the Planck's constant and ν_{ij} is the frequency of the emitted photon. The number density of atoms / ions in the upper energy level i , N_i , is $N_i = (Ng_{ik}/Z(T))exp(-\epsilon_i/k_B T)$, where k_B is the Boltzmann constant, N is the total number density of atoms / ions of each considered species (N I, O I, H I, ...) and $Z(T)$ is the corresponding partition function (Godin and Trépanier, 2004), (Teulet et al., 2009).

Lines dominated by Instrument and / or Doppler broadening exhibit a Gaussian profile. However, when Stark broadening dominates (for sufficiently high electron densities $\geq 10^{16}$ cm $^{-3}$), the spectral line profile exhibits a Lorentzian shape. The calculated synthetic spectra shown in this section include convolved

Instrumental ($\Delta\lambda_I$), Doppler ($\Delta\lambda_D$) and Stark ($\Delta\lambda_S$) full width broadenings of spectral (hydrogenic and nonhydrogenic) lines associated with neutrals and singly ionized ions. Synthetic spectra assume that spectral lines have a Lorentzian shape with a full width at half maximum given by $\Delta\lambda_{Synthetic} = 0.5 \times \Delta\lambda_S + \sqrt{(0.5\Delta\lambda_S)^2 + \Delta\lambda_I^2}$ since in our conditions we have that $\Delta\lambda_S \gg \Delta\lambda_I$ and $\Delta\lambda_I \gg \Delta\lambda_D$ (Nikiforov et al., 2015).

The nonhydrogenic Stark broadening is predominantly caused by electrons so that we use equation (13.14) in Bekefi (1976) where the electron impact approximation is assumed and corrected for the relatively unimportant quasistatic ion broadening (Bekefi, 1976). A comprehensive list of coefficients needed to compute nonhydrogenic Stark broadening from expression (13.14) in Bekefi (1976) is given in Table 4-5 of Griem (1964).

The limited accuracy of our synthetic spectra is mainly due to inaccurate data and / or to the complete lack of data needed to calculate spectra. For instance, Stark broadening coefficients for the neutral lines 648.17 nm, 648.27 nm, 648.37 nm and 648.48 nm are not available in Table 4-5 of Griem (1964) and we selected instead the available coefficients of the closest neutral N I line in 537.20 nm. In addition, the Einstein coefficients (A) of the N I lines 648.17 nm, 648.27 nm, 648.37 nm and 648.48 nm are not very accurate (category "C" in Kramida et al. (2015)). We applied a reduction of 77 % to the Einstein coefficient of the neutral N I line at 648.27 nm and did not consider the other three (less intense) lines. This is justified so that the synthetic and measured spectra of the small spark match at 2.890 μs when a pressure of $\simeq 1$ atm is reached in the spark channel (see Figure 5.3(c) and lower right panel of Figure 5.16). However, for the investigated meter long discharges (SI and LI) we find that room pressure is not yet reached for the last accessible times (see Figure 5.3(a) and 5.3(b)) and, consequently, their

spectra can not be used to estimate the reduction of the A coefficient of the neutral N I line at 648.27 nm.

Stark broadening of hydrogenic lines like H_α is implemented by using $N_e = C(N_e, T)\Delta\lambda_S^{3/2}$ (Griem, 1964) where $\Delta\lambda_S^{3/2}$ is the full Stark width and $C(N_e, T)$ is a coefficient that is only a weak function of the electron density. This expression combines, in an approximate form, the broadening due to electrons and that due to the ion dynamics. Values of $C(N_e, T)$ for several hydrogen lines (including H_α) are summarized in Table 14-1 of Griem (1964).

Stark broadening of molecular species is not considered since molecules will only be present at low temperatures when the ionization degree and electron density are such that Stark broadening is no longer the dominant broadening mechanism. For the case of double ionized N III ions, no Stark broadening coefficients are available. We have considered an arbitrary Stark broadening of 0.1 nm convolved with the instrumental broadening.

The calculated synthetic spectra also include the contribution from possible black body (continuum) emission, which has been considered as a fitting parameter of the synthetic to the measured spectra.

Synthetic spectra in Figure 5.11 exhibit two strong singly ionized N II lines at 648.20 nm and 661.05 nm and a weak H_α line (656.27 nm) that slightly grows with decreasing temperature from 35000 K to 30000 K. We see that the spectrum for 35000 K shows two small wrinkles at 645.41 nm and 646.70 nm (corresponding to two doubly ionized N III spectral lines). Also for 35000 K, the two weak features at 656.52 nm and 657.11 nm are due to two singly ionized O II spectral lines. These O II emissions slightly affect the shape of the line at 656.2 (H_α) at high temperatures. Black body emission is especially noticeable in these high temperature spectra.

In Figure 5.12 we see that the spectrum for 18000 K shows two weak humps at 645.44 nm and 645.59 nm corresponding to two neutral O I spectral lines. These O I features become less noticeable at 29000 K due to increasing ionization. Finally, the weak features shown at 649.12 nm and 649.95 nm for 18000 K are associated to two neutral N I lines that fade away with increasing temperatures. Black body emission in this temperature range (18000 K - 29000 K) is much less important than for higher temperatures (see Figure 5.11).

Figure 5.13 shows synthetic spectra calculated for the lowest considered temperature range (8000 K - 16000 K). The line at 660.8 nm corresponds to molecular emission. In particular, it corresponds to a vibrational transition ($v' = 6 \rightarrow v'' = 3$) of the first positive system (FPS) of molecular nitrogen (N_2) that remains visible at 8000 K. The H_α line (656.27 nm) starts to be apparent from $\simeq 8000$ K (very narrow) and it keeps growing up to $\simeq 20000$ K (see Figure 5.12) when it begins to decline. Around $\simeq 18000$ K - 20000 K (see Figure 5.12) the 648.20 nm N II ion line is replaced by a N I multiplet (648.17, 648.27, 648.37 and 648.48 nm) that remains active for about 10 μs for the SI discharge and during tens of μs in the case of the LI discharge.

Finally, Figure 5.14 - Figure 5.16 present a comparison of synthetic spectra with measured ones for meter long discharges (SI in Figure 5.14 and LI in Figure 5.15) and for the small spark (Figure 5.16). Synthetic and measured spectra do not completely agree. We think that this is mainly due to two reasons: (a) unavailability and / or lack of accurate basic data (Einstein coefficients and Stark broadening parameters) needed to compute reliable synthetic spectra based on equilibrium concentrations of excited species and (b) to the fact that the ultra-high speed recorded spectra include light emissions from the hot and overpressure shock front and from the hot core air plasma channel (kept at a lower gas density

than ambient) behind the shock front.

Regarding point (b) (overpressure hot shock front and hot channel core), it is interesting to analyze Figure 5.14 (for the SI meter long discharge) and Figure 5.16 (for the small spark). Both of them display spectra corresponding to the six times shown in, respectively, Figure 5.1(b) and Figure 5.1(f). Figure 5.14 shows that synthetic and measured spectra nicely agree at $-0.120 \mu\text{s}$ (the earliest time before triggering that we could evaluate), a time for which we could measure the temperature but not the corresponding electron density. The match of spectra at $-0.120 \mu\text{s}$ suggests that the discharge channel overpressure (with respect to the ambient 1 atm pressure) is still very small and that the electron density in the plasma channel would be very close to the equilibrium electron density at 1 atm (used to compute the synthetic spectra). However, $0.476 \mu\text{s}$ afterwards (or $0.356 \mu\text{s}$ after triggering) the channel overpressure (and black body radiation) becomes very important (see Figure 5.14 for 32000 K) with $\delta_p > 4$ (see Figure 5.3(b) and Figure 5.17), which is reflected in the low H_α signal of the synthetic spectra. The overpressure in the discharge channel diminishes as time progresses but it still remains ($\delta_p \simeq 2$) at $2.260 \mu\text{s}$ (see Figure 5.17). Thus, time-resolved spectroscopy indicates that continuum radiation is negligible at very early (pre-trigger) times, reaches a maximum at about $0.356 \mu\text{s}$ after triggering and tend to decrease with increasing times (lower measured temperature).

In the case of Figure 5.15 for the LI lightning-like discharge, we see that black body continuum emission at trigger time ($0.0 \mu\text{s}$) - associated to 31000 K - is considerably smaller than at lower temperatures.

The sequence of six synthetic and measured spectra displayed in Figure 5.16 for the case of a small spark indicates that the overpressure ($\delta_p > 3$, see Figure 5.3(c) and Figure 5.19) was already set in the first time ($0.510 \mu\text{s}$ at 33000 K)

we could evaluate. In the case of the small spark, the overpressure in the channel rapidly evolves towards ambient pressure in less than $3 \mu\text{s}$ as we can see in the spectra shown in Figure 5.16 for $2.890 \mu\text{s}$ for which $\delta_p \simeq 1$ (see Figure 5.3(c) and Figure 5.19). The dynamics of the black body continuum (or background) shown in Figure 5.16 is similar to that of Figure 5.14 and 5.15, except for the fact that black body radiation is already noticeable in the first time ($0.510 \mu\text{s}$) of the small spark spectra but, as in Figure 5.14 and 5.15, it tends to disappear as time progresses and the pressure in the plasma channel returns to ambient values.

Figures 5.17 through 5.19 show the time evolution of the total and partial pressures (due to electrons, ions and neutrals) in the discharge channel shock front for, respectively, the meter long discharges SI (Figure 5.17) and LI (Figure 5.18), and for the small spark discharge (Figure 5.19). Once the overpressure factor δ_p is experimentally determined, we can approximately compute the total and partial pressures by using the ideal gas law with the concentrations of electrons, ions and neutrals multiplied by δ_p . Figures 5.17 - 5.19 also include the approximate position (R) and speed (U) of the hydrodynamic shock front estimated with $R = \alpha t^{0.5}$ and $U = 0.5 \times \alpha t^{-0.5}$ resulting from the solution of the Rankine-Hugoniot equations to evaluate the discrete changes in the mass density, pressure and velocity across the shock front produced after electrical breakdown (Zahn et al., 1982). The values of the parameter α is estimated from $\alpha = (2E/(\pi\rho 0.63))^{0.25}$ where E is the total injected electric energy per unit length (in J m^{-1}) (see Figures 5.4, 5.5 and 5.6) and ρ is the ambient air density in the laboratory experiments (Zahn et al., 1982). In our case, α (small spark) = $2.29 \text{ m s}^{-0.5}$, α (meter long SI discharge) = $2.89 \text{ m s}^{-0.5}$ and α (meter long LI discharge) = $4.93 \text{ m s}^{-0.5}$. The adopted values for ρ were 1.10 kg m^{-3} for the small spark experiments at the IAA-CSIC in Granada (94000 Pa, 50 % and 293 K) and 1.17 kg m^{-3} for meter

long discharge experiments in Barcelona (101000 Pa, 50 %, 293 K). The values of U and R decrease and increase monotonically as time progresses with U reaching values of about 10 times the speed of sound in air (see Figures 5.18 for the LI discharge). The shock front position R should approximately indicate the location where overpressure is measured.

Figure 5.20 shows the self-absorption (SA) coefficient of the 647 nm and 661 nm singly ionized N II lines as a function of time for meter long discharges SI (top panel) and LI (middle panel), and for a small (4 cm long) spark discharge (bottom panel). We have evaluated the SA under the assumption of a homogenous plasma (El Sherbini et al., 2005). The SA is defined as the ratio of the measured peak intensity to the value of the line intensity in absence of self-absorption. SA is equal to one if the the line is optically thin, while it decreases to zero as the line becomes optically thick. Thus, the SA(s) are obtained from $\Delta\lambda / \Delta\lambda_0 = (\text{SA})^\beta$ with $\beta = -0.54$ (El Sherbini et al., 2005) and $\Delta\lambda$ and $\Delta\lambda_0$ being the full width at half maximum (FWHM) of the observed (measured) ion line(s) and the calculated FWHM of the true ion line (without self-absorption), respectively. Note that the calculated FWHM of the true ion lines use the measured electron density obtained from the H_α line, which is known to be insignificantly affected by self-absorption unless the amount of hydrogen is very high, which is not the case in air (El Sherbini et al., 2005), (Parigger et al., 2014). We have considered that $\Delta\lambda_0$ results from the convolution of calculated instrumental and Stark effect FWHM(s) of the two N II ionic lines which self-absorption coefficients are searched for. The calculation procedure of Stark FWHMs was previously commented. According to Figure 5.20, the values of the SA coefficient grow towards one with increasing time (or decreasing pressure in the discharge channel). This is especially evident for the LI discharge (middle panel of Figure 5.20) where the the SA increases from 0.2 to

≥ 0.8 as the pressure in the channel decreases (see Figures 5.18).

Finally, Figures 5.21 and 5.22 illustrate the method followed to derive the electron density and electron temperature. For the electron density, the black body background inherited from the spark core radiation is first subtracted in Figure 5.21 to not overestimate the electron density. As we are considering a small bandwidth (645 — 664 nm) of the spark spectrum, we have reasonably assumed that the black body contribution is flat in the narrow spectral bandwidth investigated and it is different at every time stage of the spark. As the spectrum is sometimes noisy, we estimated the blackbody radiation background as the mean value of the first 5 lowest values (starting in 645 nm) of the line spectra at any instant of time. So, for every time stage of the spark, we subtracted this blackbody radiation background from its discharge line spectrum before estimating the electron density.

Due to the large electron density the broadening of the H_α line is large and it should be considered that it extends over the entire ($\simeq 20$ nm) spectral range covered in our ultra high speed observations at 2.1 Mfps. Once the shape of the H_α (green dotted line) is determined, we compute the full width at half area (FWHA) (see grey shadow) under the green dotted line used to derive the measured electron density. The FWHA for the H_α is much less influenced by ion dynamics than the full width at half maximum (FWHM) and, consequently, it is a more reliable procedure (than using the FWHM) to obtain the electron density from the H_α line.

Figure 5.22 shows that to evaluate the electron temperature we only consider the intensity signal above the black body background (see red dots) and we consider the total area (not the peak maximum) under the intensities of the 647 nm and 661 nm singly ionized N II lines.

Figure 5.23 shows a raw image (8 pixels height and 1024 pixels wide) spectrum of the LI mode discharge. The method we used to derive line spectra from raw spectra is the same as the one we described before (Passas et al., 2019): (1) distortion correction, to straighten the curved raw spectrum; (2) wavelength calibration, to assign an absolute wavelength to each pixel of the CMOS sensor; (3) flux calibration, to provide the spectral sensitivity of the spectrograph; and (4) data reduction.

In this case (using a different diffraction grating to that used in (Passas et al., 2019)), for steps (1) and (2), we recorded the spectrum of two commercial neon and argon spectral lamps. Then, we trimmed these images so all spectral lines appeared in every row of the spectrum. We identified the corresponding wavelengths by comparing the distances between the spectral lines to the gaps that neon and argon spectra show according to NIST atomic spectra databases. Finally, to straighten the spectrum, we assigned the central pixel of each spectral line to a single wavelength for every row of the spectral image with a Python code we have implemented, that generates a calibration matrix that will be used hereinafter to correct the distorted spectra recorded with GALIUS, associating every pixel coordinate of the CMOS to an absolute wavelength. This calibration matrix is calculated every time we perform a new set of measurements. For step (3) we recorded the spectral radiance of a halogen tungsten spectral lamp (QTH) at 50 fps located at 60 cm from the collector lens of GALIUS using the diffraction grating using here, and corrected its distortion according to steps (1) and (2), so we have the straightened QTH response. Then we repeated these measurements with a calibrated Jobin Yvon HORIBA FHR1000 spectrometer using the same calibration setup. From these calculations, we obtained the diffraction grating instrument function that allows us to do a relative flux correction of the raw signal.

Finally, for step (4) we subtracted the black image background (an image without any spectrum) from the raw image. Then, we applied the wavelength calibration matrix calculated in steps (1) and (2), to straighten the spectrum and assign a wavelength to every column of the CMOS image. Then, we divided this image by the instrument function calculated in (3) so we corrected the CMOS inhomogeneities and the different response of the pixels to different wavelengths. Last step was to sum up the 8 rows of the reduced spectrum so we got the line spectra shown in the main manuscript.

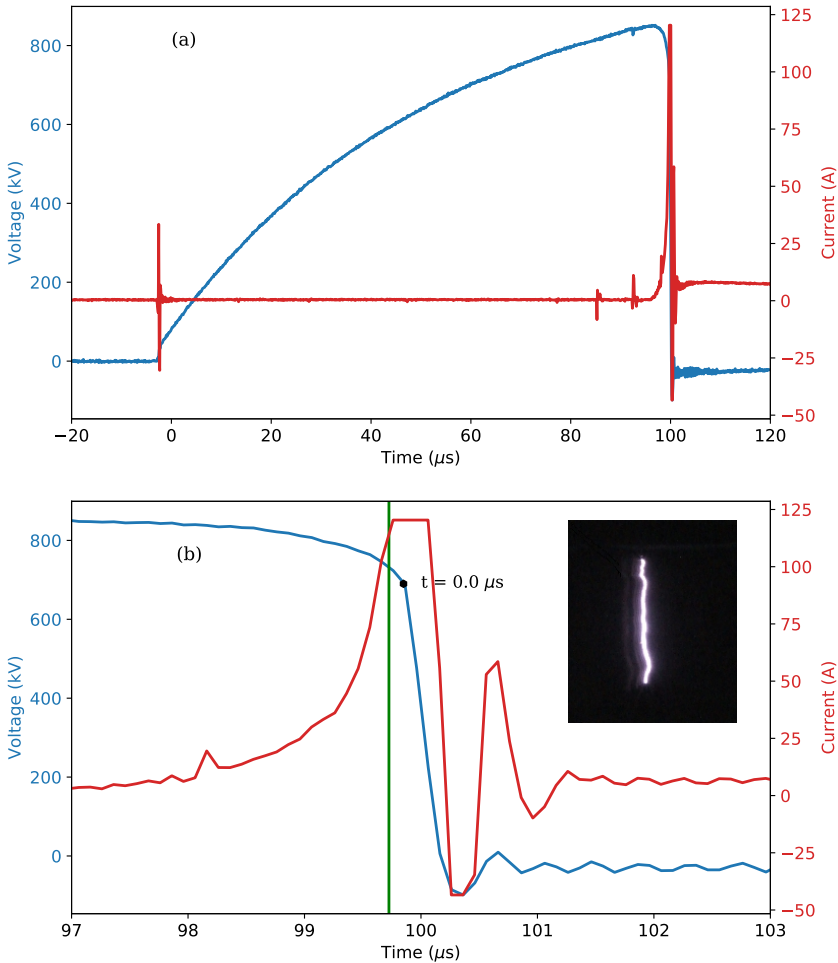


Figure 5.4: Measured voltage (blue line) and current (red line) during the generation of the Switching Impulse (SI) mode discharge of the Marx generator. (a) Complete time evolution of the voltage and current. (b) Zoom in for a close view of the rise / decay region around $100 \mu\text{s}$ with an image showing the typical appearance of the SI discharge. The green line in (b) indicates the time of the first recorded spectrum. The black dot in (b) indicates the triggering time. The injected electric energy is 81 J or 81 J/m (since the discharge length is $\simeq 1$ m).

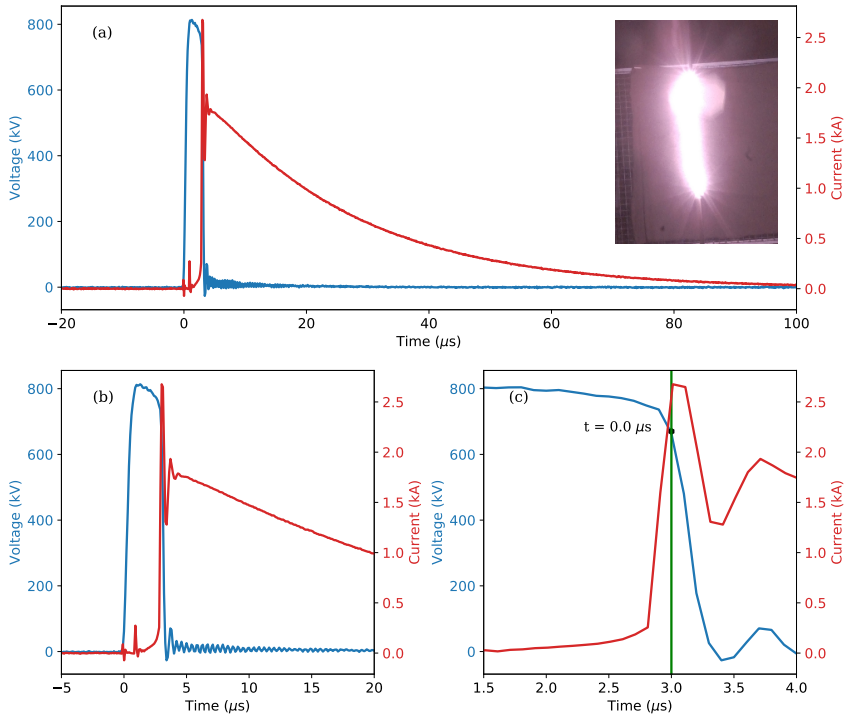


Figure 5.5: Measured voltage (blue line) and current (red line) during the generation of the Lightning Impulse (LI) mode discharge of the Marx generator. Panels (a), (b) and (c) show time intervals between, respectively, $-20 \mu\text{s}$ and $100 \mu\text{s}$, $-5 \mu\text{s}$ and $20 \mu\text{s}$, and $1.5 \mu\text{s}$ and $5 \mu\text{s}$. The inset image in (a) shows the typical appearance of the LI discharge. The green line in (c) indicates the time of the first recorded spectrum. The black dot in (c) indicates the triggering time. The injected electric energy is 684 J or 684 J/m (since the discharge length is $\simeq 1 \text{ m}$).

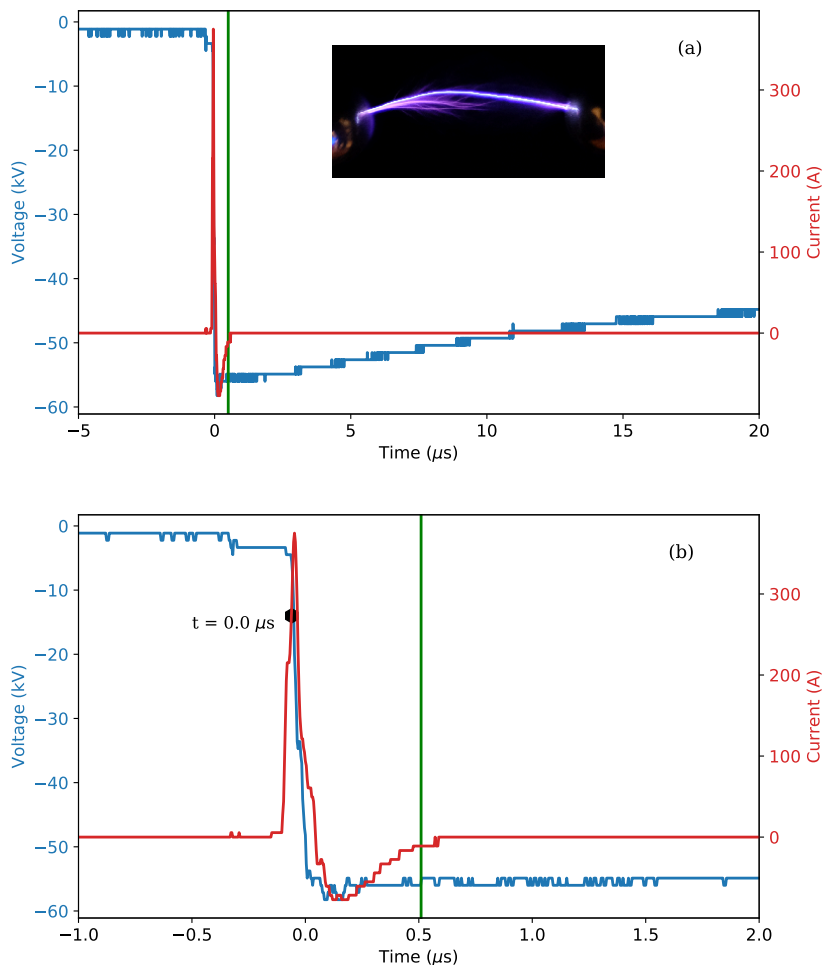


Figure 5.6: Measured voltage (blue line) and current (red line) during the generation of the small (4 cm long) spark discharge. (a) Complete time evolution of the voltage and current with an inset image showing the typical appearance of the small spark discharge. (b) Zoom in for a close view of the rise / decay region around $0.0 \mu\text{s}$. The green line indicates the time of the first recorded spectrum. The black dot in (b) indicates the triggering time. The injected electric energy is 1.2 J or 30 J/m (since the discharge length is $\simeq 0.04 \text{ m}$).

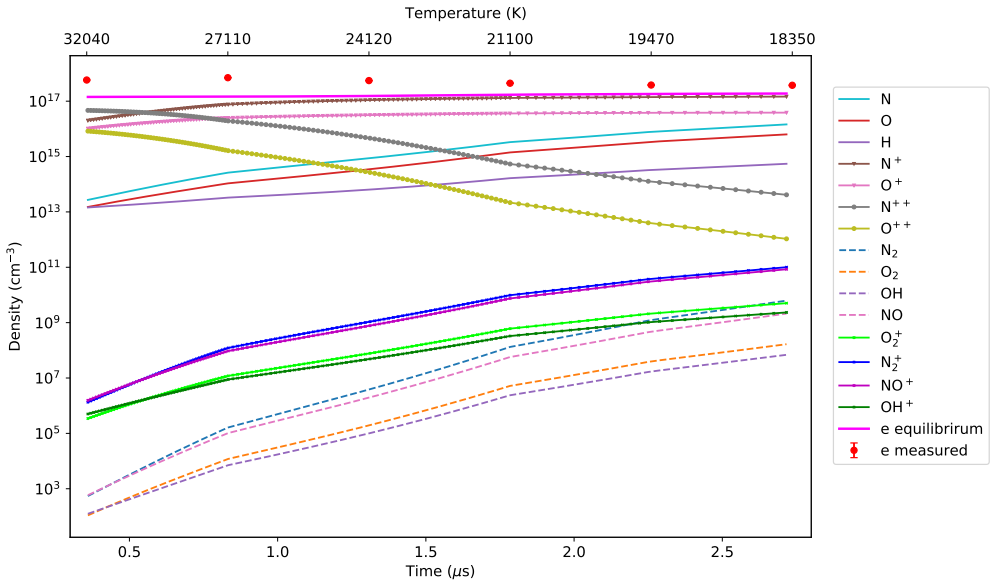


Figure 5.7: Measured electron density (red dots) in the SI lightning-like discharge and the equilibrium composition in a thermal plasma of humid (50 % RH) air at 1 atm (ambient pressure in Tarrasa, Spain). The figure shows the concentrations for a selection of neutral (atoms and molecules) and ionic (atomic and molecular) species as a function of time (bottom axis) and measured temperatures (top axis). The displayed times correspond to the different SI recorded spectra. The temperatures derived from each measured spectra are shown in the top axis. The measured electron densities can be recovered by multiplying the equilibrium electron densities at 1 atm by the δ_p factor for each time (see Figure 5.3).

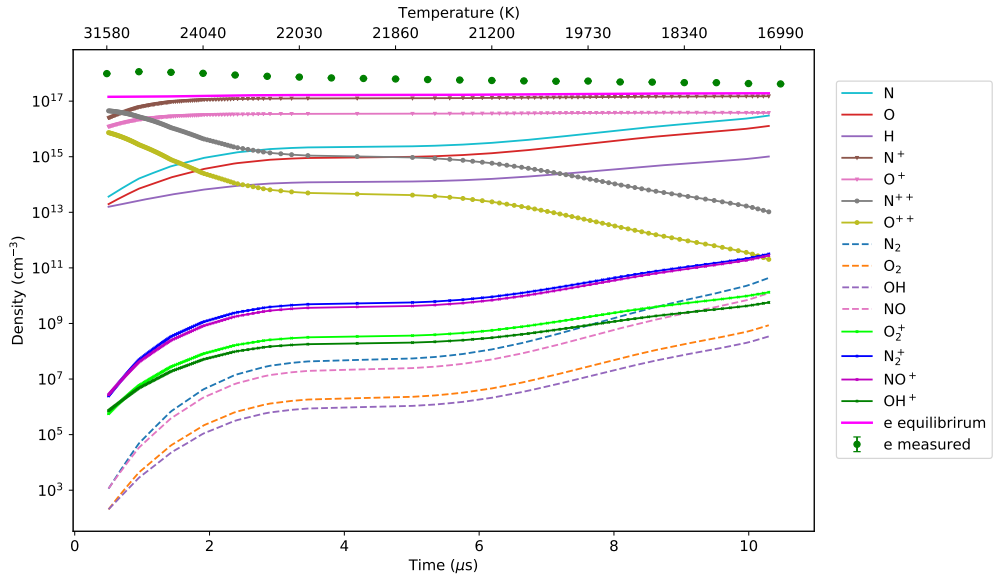


Figure 5.8: Measured electron density (green dots) in the LI lightning-like discharge and the equilibrium composition in a thermal plasma of humid (50 % RH) air at 1 atm (ambient pressure in Tarrasa, Spain). The figure shows the concentrations for a selection of neutral (atoms and molecules) and ionic (atomic and molecular) species as a function of time (bottom axis) and measured temperatures (top axis). The displayed times correspond to the different LI recorded spectra. The temperatures derived from each measured spectra are shown in the top axis. The measured electron densities can be recovered by multiplying the equilibrium electron densities at 1 atm by the δ_p factor for each time (see Figure 5.3).

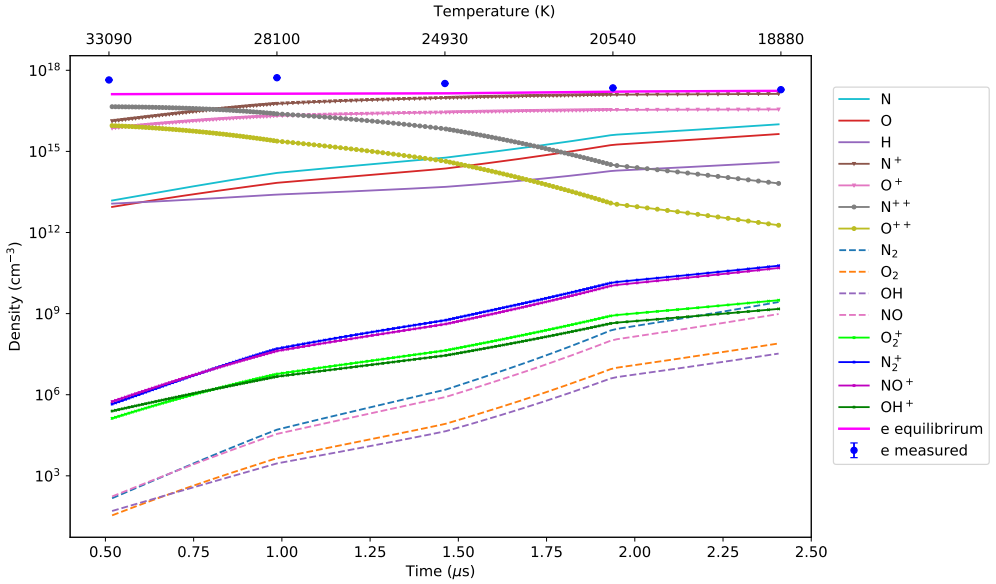


Figure 5.9: Measured electron density (blue dots) in the small spark discharge and the equilibrium composition in a thermal plasma of humid (50 % RH) air at 0.93 atm (ambient pressure in Granada, Spain). The figure shows the concentrations for a selection of neutral (atoms and molecules) and ionic (atomic and molecular) species as a function of time (bottom axis) and measured temperatures (top axis). The displayed times correspond to the different small spark measured spectra. The temperatures derived from each recorded spectra are shown in the top axis. The measured electron densities can be recovered by multiplying the equilibrium electron densities at 0.93 atm by the δ_p factor for each time (see Figure 5.3).

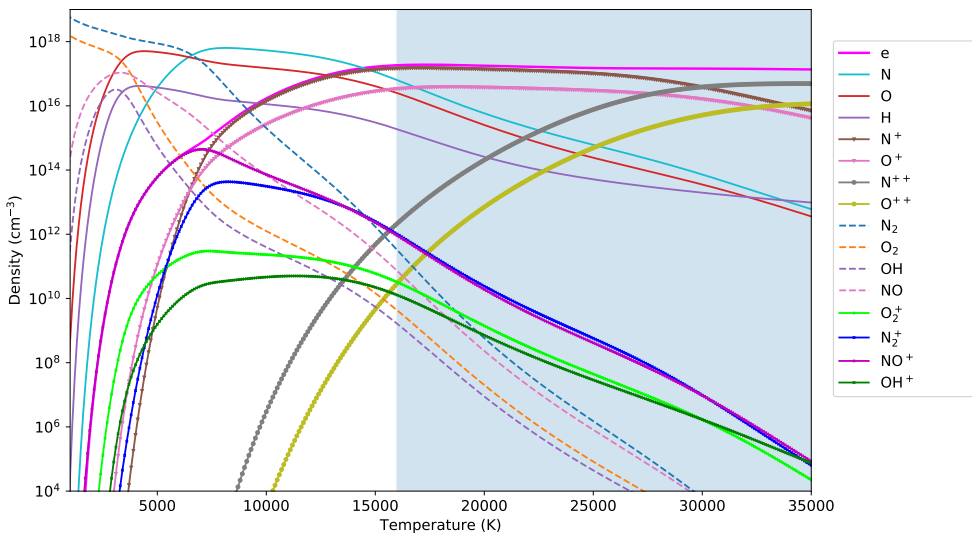


Figure 5.10: Equilibrium composition in an atmospheric pressure plasma of humid (50 % RH) air for gas temperatures between 1000 K and 35000 K. The figure displays the concentrations of the same species shown in Figures 5.7, 5.8, and 5.9. The bluish shadowed region indicates the variation of equilibrium densities within the approximate range of measured temperatures including temperatures above measured values due to possible underestimated temperature measurements.

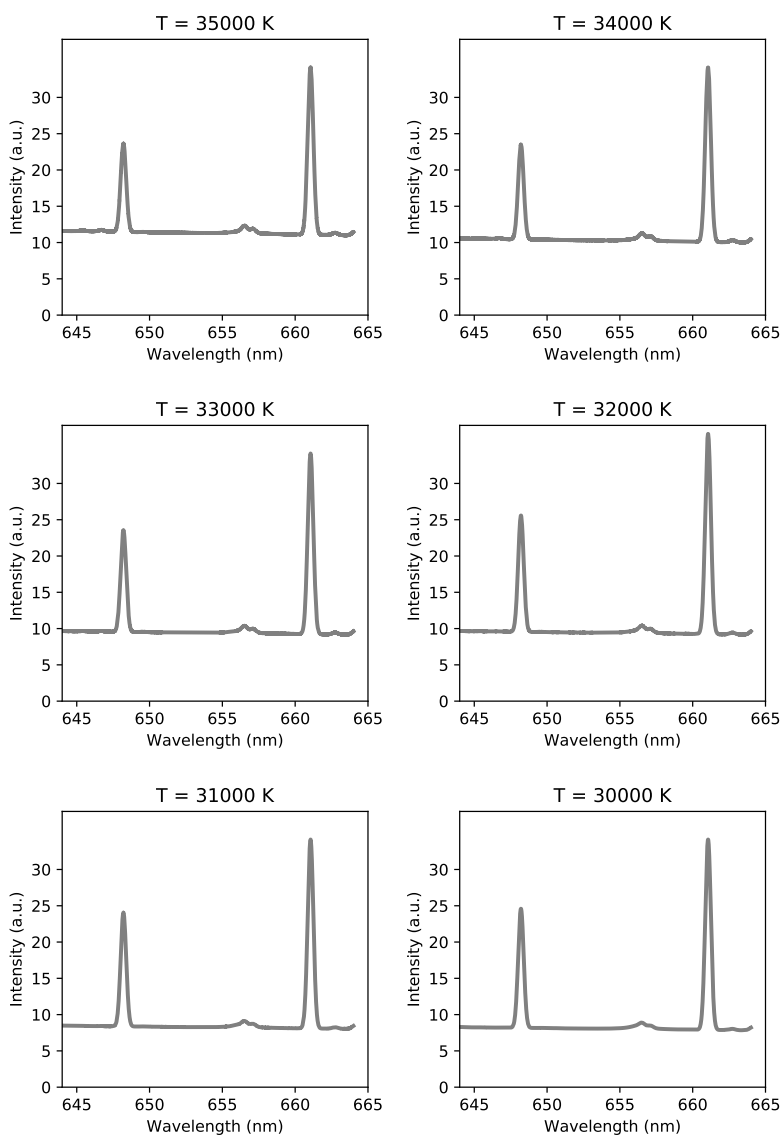


Figure 5.11: Synthetic spectra (645 nm - 665 nm) for an atmospheric pressure thermal plasma of humid (50 % RH) air for gas temperatures between 35000 K (top left) and 30000 K (bottom right). The figure illustrates the case of the meter long Switching Impulse (SI) discharge.

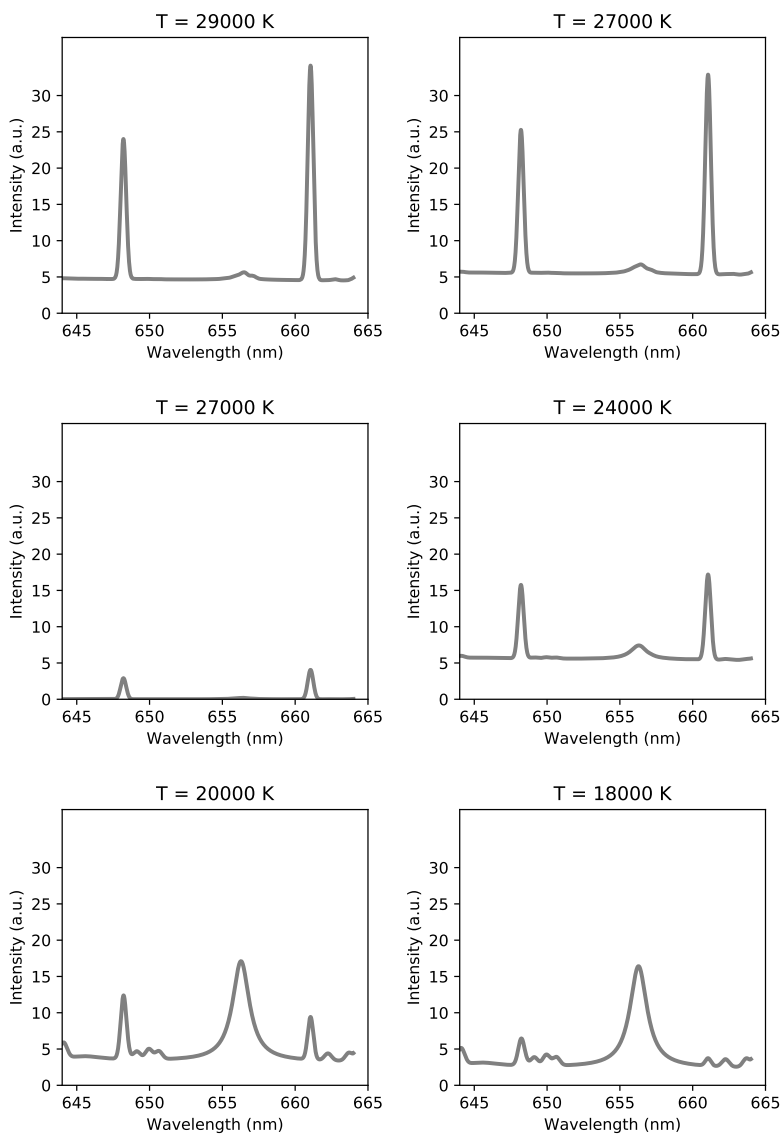


Figure 5.12: Synthetic spectra (645 nm - 665 nm) for an atmospheric pressure thermal plasma of humid (50 % RH) air for gas temperatures between 29000 K (top left) and 18000 K (bottom right). The figure illustrates the case of the meter long Switching Impulse (SI) discharge. Note that the case of 27000 K is shown with and without black body (continuum) radiation since no black body is seen in the measured spectra at $-0.120 \mu\text{s}$ (see Fig 5.14).

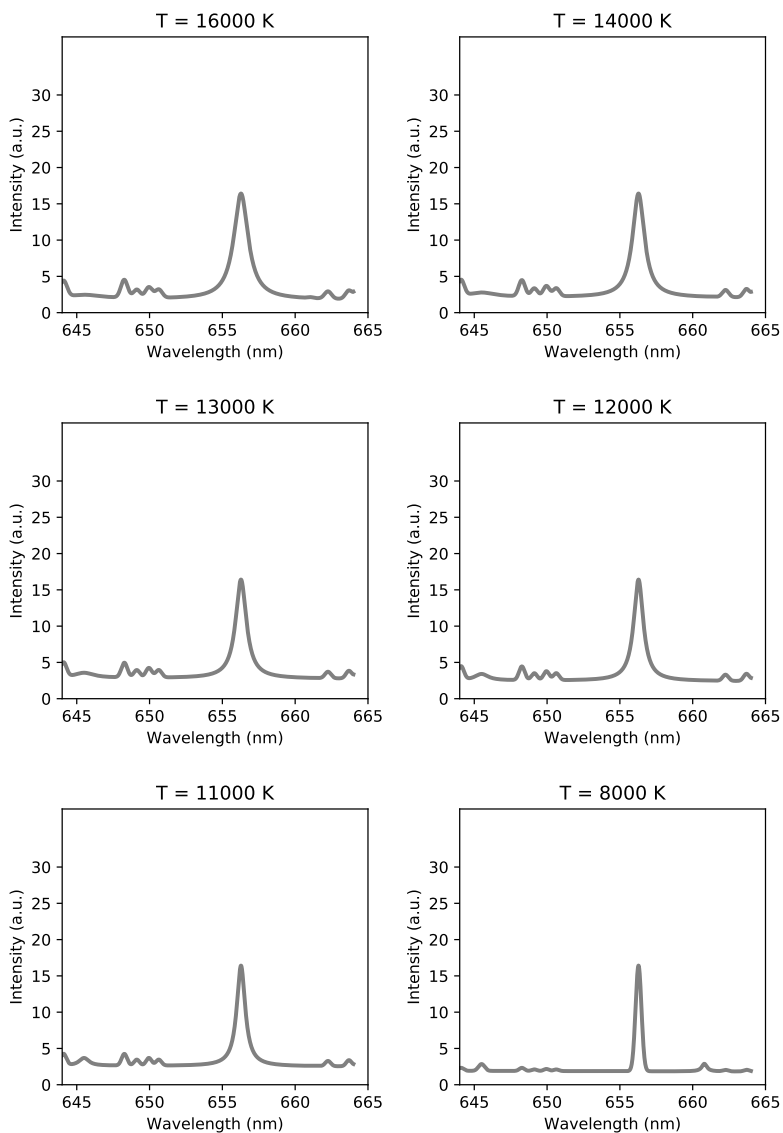


Figure 5.13: Synthetic spectra (645 nm - 665 nm) for an atmospheric pressure thermal plasma of humid (50 % RH) air for gas temperatures between 16000 K (top left) and 8000 K (bottom right). The figure illustrates the case of the meter long Switching Impulse (SI) discharge.

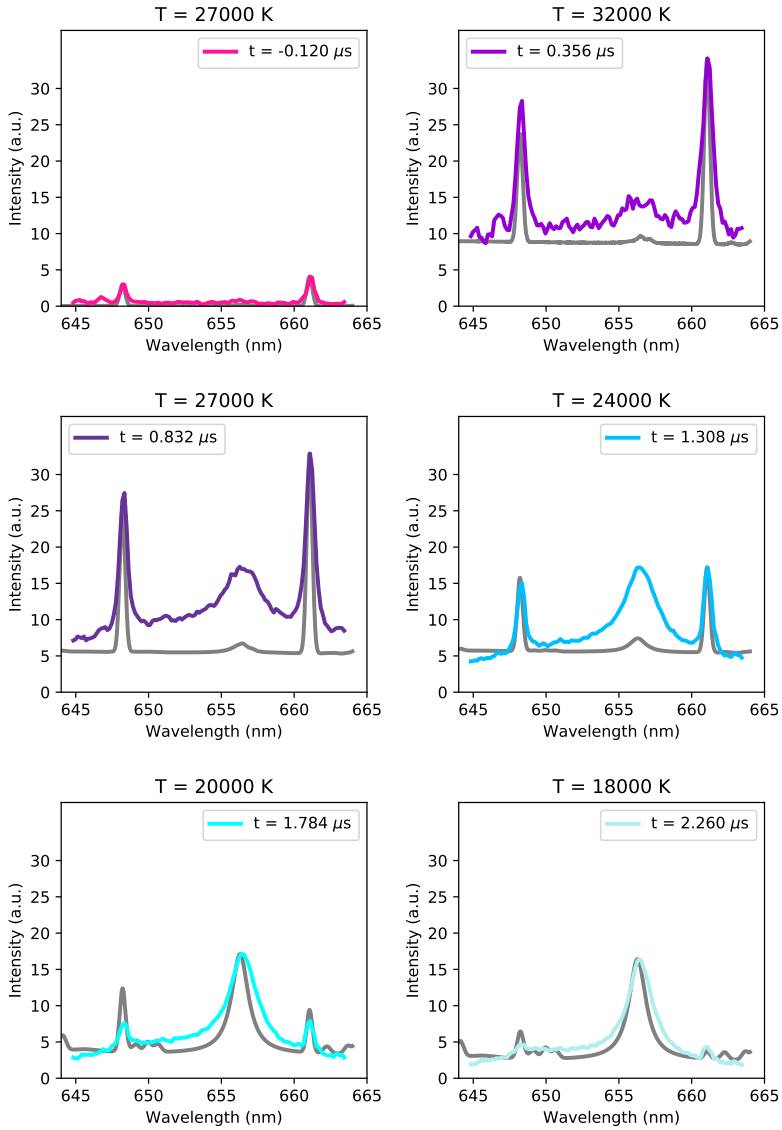


Figure 5.14: Comparison between calculated synthetic spectra (grey line) and measured spectra corresponding to the early times (from pre-trigger sub- μs to $\approx 2.5 \mu\text{s}$ after triggering) of a meter long Switching Impulse (SI) discharge. Note that no black body emission is detected at $-0.120 \mu\text{s}$ with 27000 K (see Figure 5.2(b) for the time evolution of the measured temperatures).

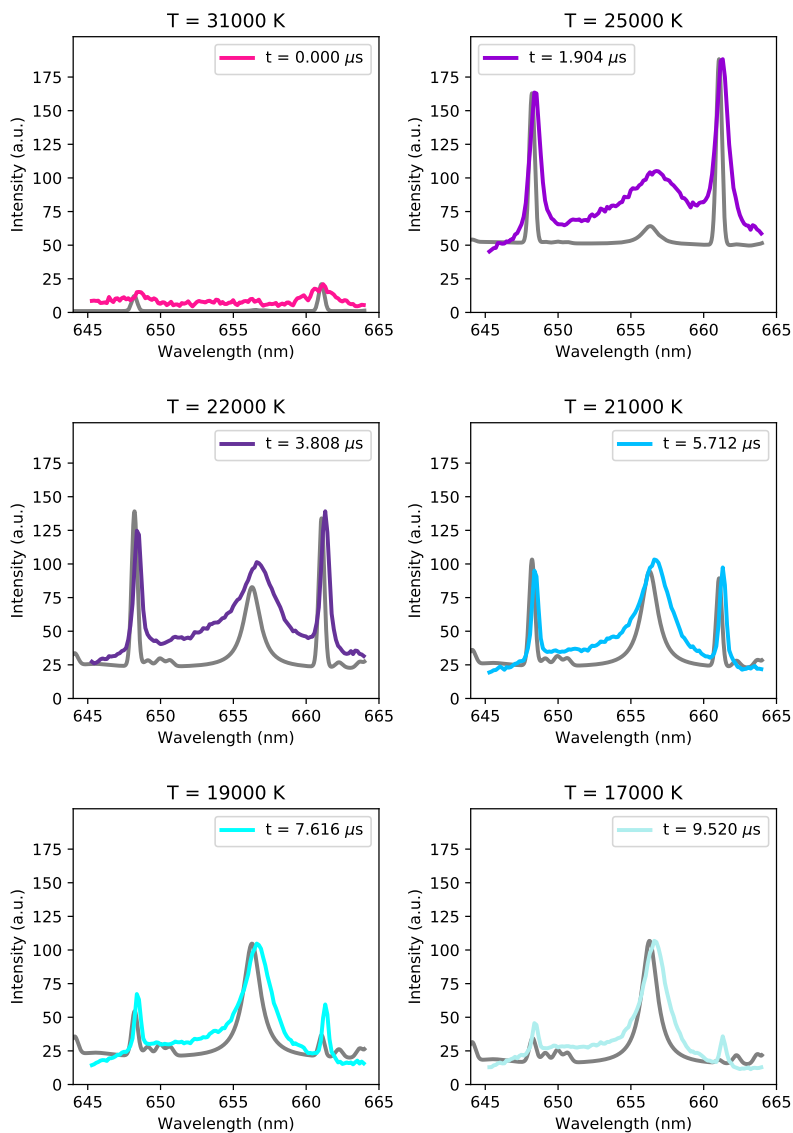


Figure 5.15: Comparison between calculated synthetic spectra (grey line) and measured spectra corresponding to the early times (from sub- μs to $\simeq 10 \mu\text{s}$) of a meter long Lightning Impulse (LI) discharge. Weak black body emission is visible in the measured spectra at 0.0 μs with a measured temperature of 31000 K.

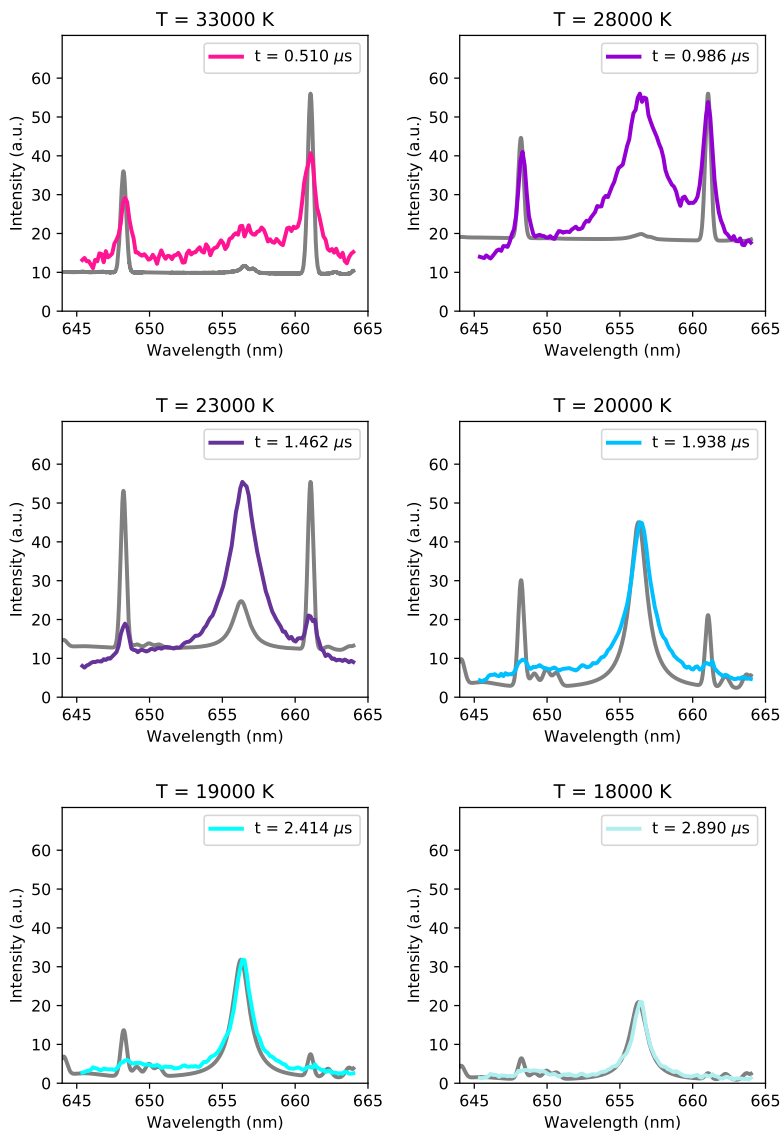


Figure 5.16: Comparison between calculated synthetic spectra (grey line) and measured spectra corresponding to the early times (from sub- μs to $\simeq 3 \mu\text{s}$) of a small spark discharge.

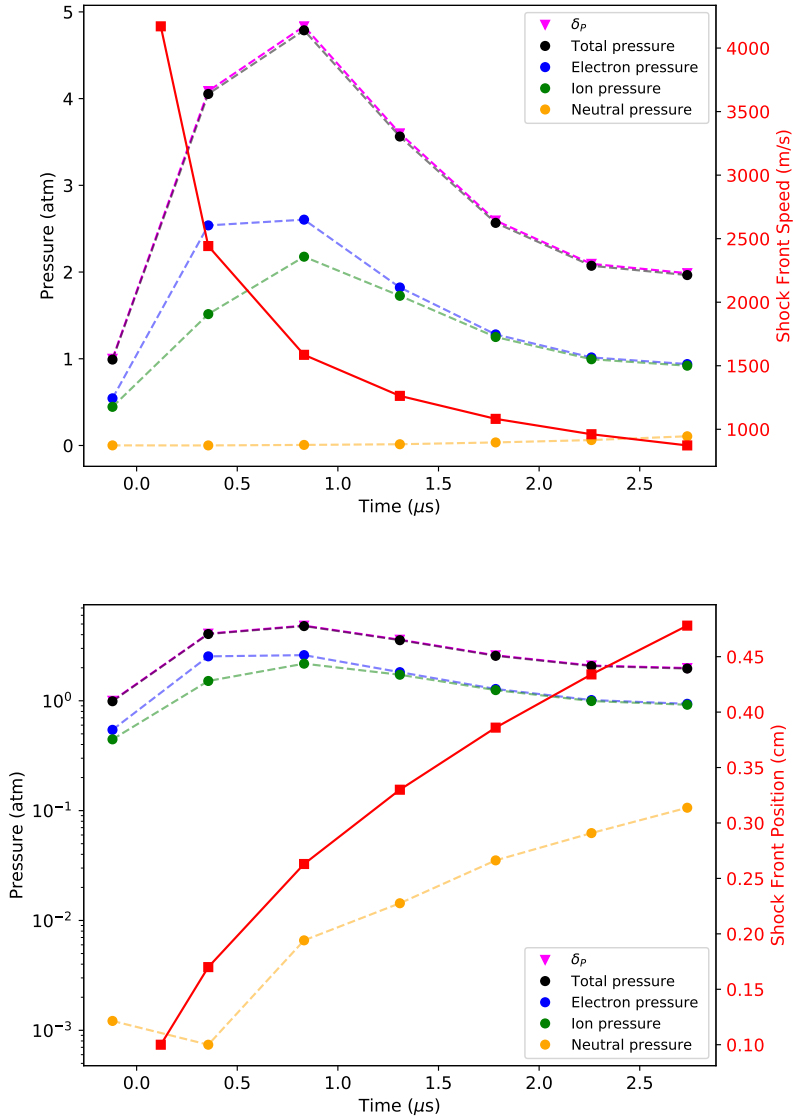


Figure 5.17: The factor δ_p , total pressure and partial pressures due to electrons, ions and neutrals as a function of time (left axis) in linear scale (top panel) and logarithmic scale (bottom panel). The right axis of the top and bottom panels include an estimation of the shock front speed (top panel) and shock front position (bottom panel) for the meter long SI discharge. Note that the pressure for $-0.12 \mu\text{s}$ was represented assuming an equilibrium (at 1 atm) electron density as it is suggested from Figure 5.14 at $-0.12 \mu\text{s}$ with 27000 K. Note also that the first value of the shock front position and speed are shown 240 ns after the pre-trigger time ($-0.12 \mu\text{s}$) for which the first image was recorded.

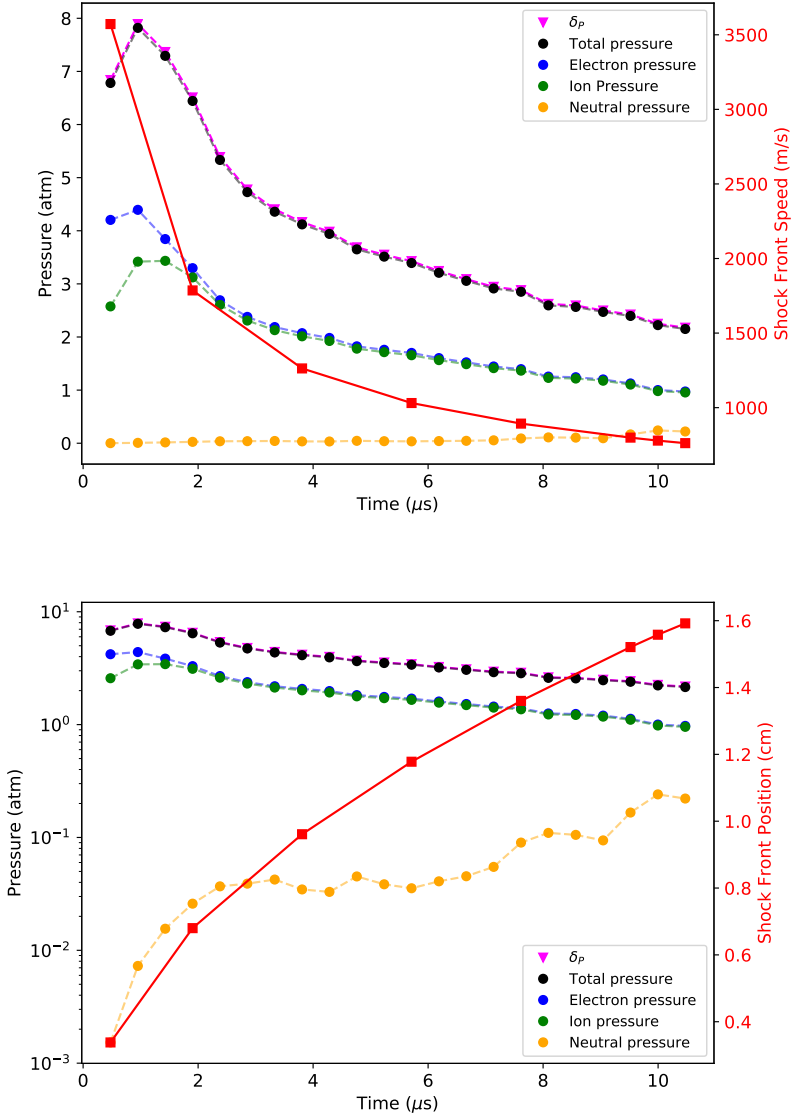


Figure 5.18: The factor δ_p , total pressure and partial pressures due to electrons, ions and neutrals as a function of time (left axis) in linear scale (top panel) and logarithmic scale (bottom panel). The right axis of the top and bottom panels include an estimation of the shock front speed (top panel) and shock front position (bottom panel) for the meter long LI discharge.

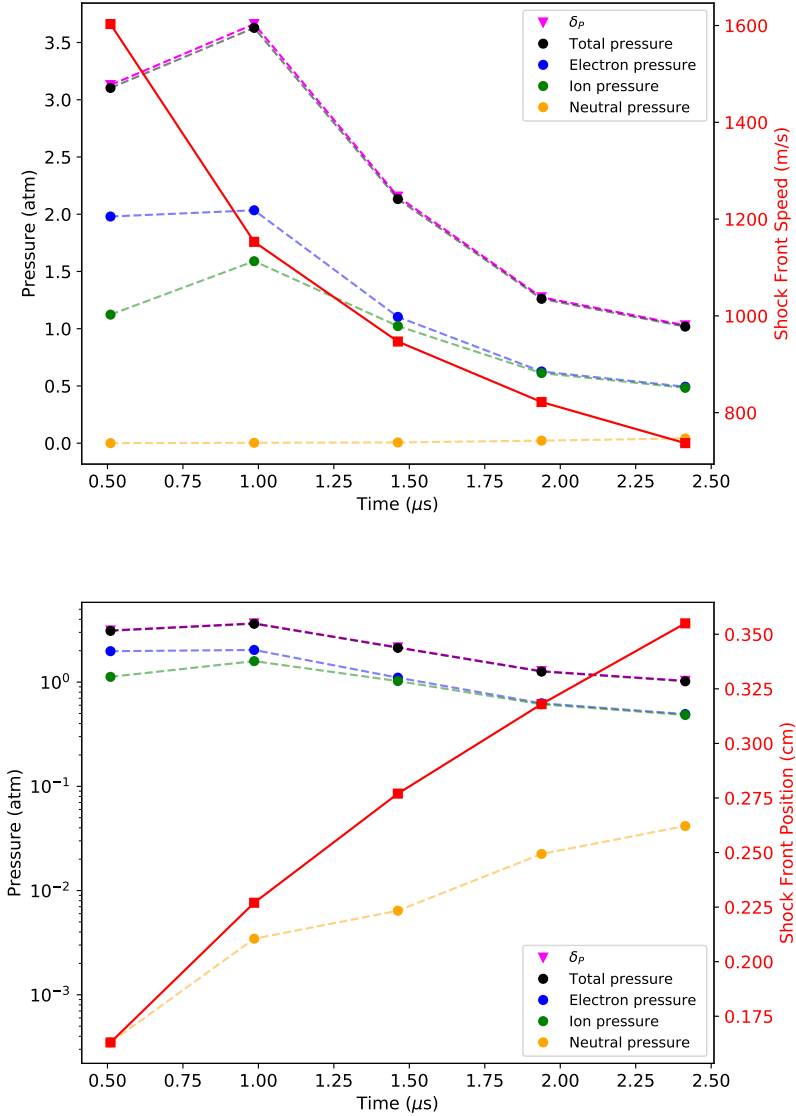


Figure 5.19: The factor δ_p , total pressure and partial pressures due to electrons, ions and neutrals as a function of time (left axis) in linear scale (top panel) and logarithmic scale (bottom panel). The right axis of the top and bottom panels include an estimation of the shock front speed (top panel) and shock front position (bottom panel) for a small (4 cm long) spark discharge.

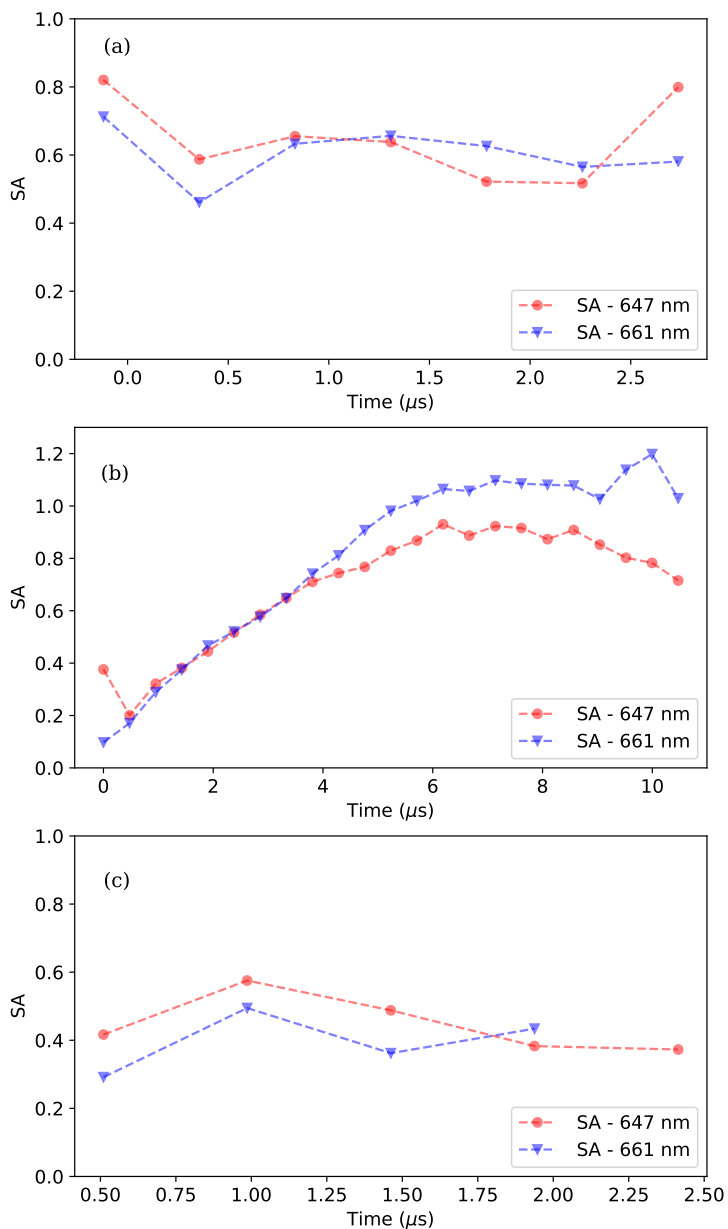


Figure 5.20: Self-absorption (SA) coefficient ($0 \leq \text{SA} \leq 1$) of the 647 nm and 661 nm singly ionized N II lines as a function of time for meter long discharges SI (top panel) and LI (middle panel), and for a small (4 cm long) spark discharge (bottom panel). A SA = 1 indicates a complete optically thin line emission while SA = 0 applies for a complete optically thick line. The signal of the 661 nm ion line was not considered reliable after 2 μs .

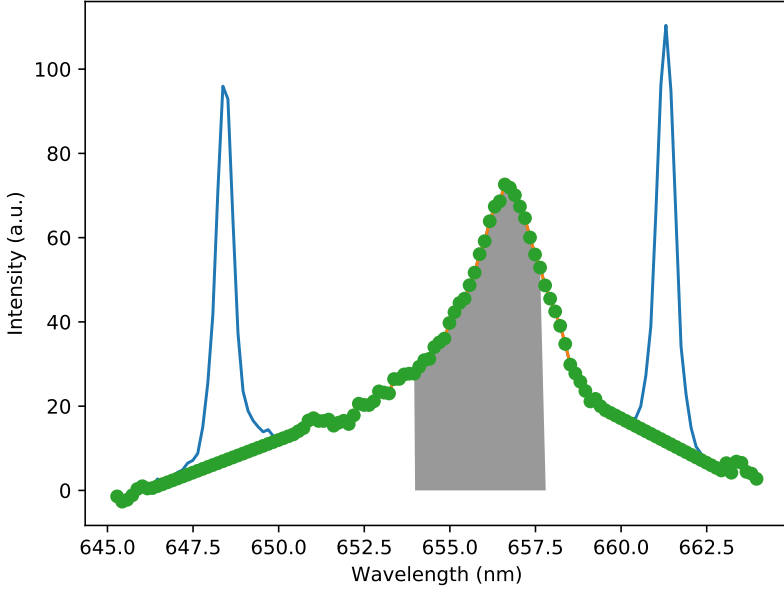


Figure 5.21: Illustration of the method followed to derive the electron density. The black body background is first subtracted. Due to the large electron density the broadening of the H_α line is large and it should be considered that it extends over the entire ($\simeq 20$ nm) spectral range covered in our ultra high speed observations at 2.1 Mfps. Once the shape of the H_α (green dotted line) is determined, we compute the full width at half area (FWHA) (see grey shadow) under the green dotted line used to derived the measured electron density. The FWHA for the H_α is much less influenced by ion dynamics than the full width at half maximum (FWHM) and, consequently, it is a more reliable procedure (than using the FWHM) to obtain the electron density from the H_α line.

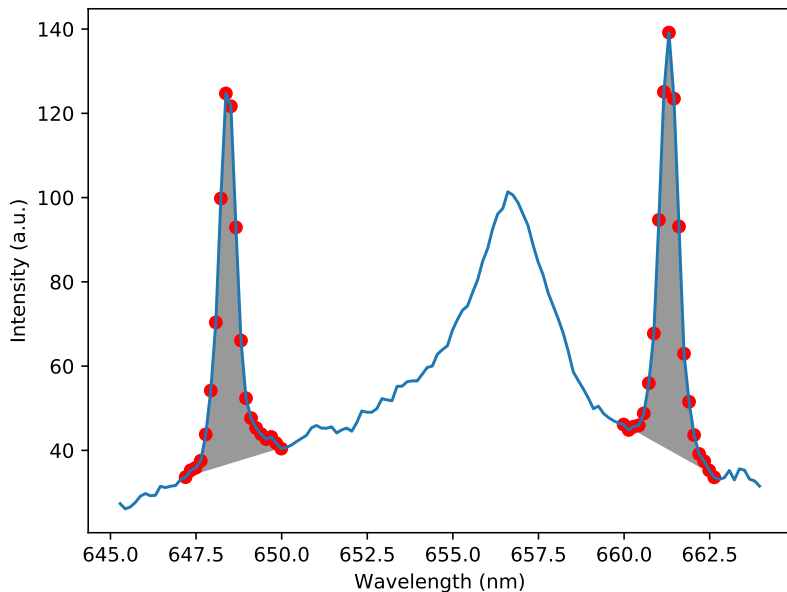


Figure 5.22: Illustration of the method followed to derive the electron temperature. To evaluate the electron temperature we only consider the intensity signal above the background (see red dots). We consider the total area (not the peak maximum) under the intensities of the 647 nm and 661 nm singly ionized N II lines.



Figure 5.23: Raw spectral image of the LI mode discharge generated with the Marx generator. This spectral image is 8 pixels height and 1024 pixels wide and was recorded at 2.1 Mfps. The diffraction grating used has 1855 lines per mm and a spectral resolution of 0.38 nm.

Chapter 6

Evidence of molecular optical emissions

The content in this chapter was published in *Journal of Geophysical Research: Atmospheres* with title ‘**High-speed spectroscopy of lightning-like discharges: evidence of molecular optical emissions**’.

Author: **Kieu, T. N.**, Gordillo-Vázquez, F. J., Passas, M., Sánchez, J., Pérez-Invernón.

Volume **126**, Issue **11**, e2021JD035016

First published: 26 May 2021

<https://doi.org/10.1029/2021JD035016>

Keypoints

- High speed (down to submicrosecond time scales), high sensitivity lightning-like spectra (380 nm-800 nm) reveal a rich chemistry
- Molecular species like CO, CN, C₂, N₂ and N₂⁺ are detected. This opens

the door to find and quantify lightning NO production by spectroscopy

- Electron concentrations and gas temperatures obtained from different methods are compared and discussed

Abstract

High speed spectra (between ~ 380 nm and ~ 800 nm) of meter long lightning-like discharges recorded at 672000 fps and 1400000 fps (with $1.488 \mu\text{s}$ and $0.714 \mu\text{s}$ time resolutions and 160 ns exposure time) show optical emissions of neutral hydrogen, singly-ionized nitrogen, oxygen and doubly-ionized nitrogen which are similar to those found in natural lightning optical emissions. The spectra recorded in the near ultraviolet-blue range (380 - 450 nm) and visible-near infrared (475 - 793 nm) exhibited features of optical emissions corresponding to several molecular species (and emission bands) like CN (Violet bands), N_2 (Second Positive System), N_2^+ (First Negative System), C_2 (Swan band) and CO (Quintet and Ångström bands). Molecular species can be formed at regions of the lightning-like channel where the gas temperature would be milder and / or in the corona sheath surrounding the heated channel. We have quantified and compared electron densities and temperatures derived from different sets of neutral and ion line emissions and have found different sensitivities depending on the lines used. Temperatures derived from ion emissions are higher and change faster than those derived from neutral emissions.

Plain Language Summary

Lightning strokes are extremely fast atmospheric electricity events characterized by temperatures that can reach tens of thousands of degrees. Investigation of the fundamental properties of different types of lightning can help to deepen our understanding on lightning chemistry and, particularly, their contribution to key molecular gases such CO, CN and NO and, also, how different types of lightning propagate. High sensitivity, time resolved optical emission spectroscopy is an ideal diagnostic technique to remotely study the fast temporal optical emissions of lightning. Our study explores the presence of molecular species production in heated lightning-like channels by using a forefront detector for microsecond and sub-microsecond time resolved lightning spectroscopy.

6.1 Introduction

Details of lightning spectroscopy studies in the first half of the twentieth century have been reviewed by [Salanave \(1961\)](#). Even though these early studies were on time-averaged spectroscopy over many lightning flashes, they already provided identification of some chemical species from their spectral features. [Wallace \(1960\)](#) examined a lightning spectrum in the near-ultraviolet (367 nm - 428 nm) that revealed the presence of the cyanide radical (CN) violet bands, N₂ second positive and the N₂⁺ first negative system that allowed them to estimate rotational temperatures in the range 6000 - 30000 K ([Wallace, 1960](#)). Later, [Wallace \(1964\)](#) re-examined another lightning spectrum in a wider spectral region (315 nm - 980 nm) and identified more line emissions of singly-ionized oxygen, nitrogen as well as the presence of Stark-broadened neutral oxygen and nitrogen lines. In the same period, [Zhivlyuk and Mandel'shtam \(1961\)](#) had also estimated gas temper-

atures in lightning that were around $20000 \text{ K} \pm 5000 \text{ K}$.

Since the 1960s, time-resolved lightning spectroscopy has advanced thanks to the development of new technologies for high speed recording. [Salanave \(1961\)](#) recorded the first time-resolved (averaged) lightning spectra using slitless spectroscopy techniques with time resolution of $\sim 20 \text{ ms}$ and spectral resolution of $\sim 0.2 \text{ nm}$. The lightning spectra in the range 385 to 690 nm showed the presence of neutral, singly-ionized ions of nitrogen, oxygen, and some emission features of CN and of the first negative system of N_2^+ , but no doubly-ionized species were detected. Stimulated by these initial lightning spectroscopic studies, a number of papers were soon afterward published on the use of lightning spectroscopy to investigate qualitative and quantitative properties of lightning ([Prueitt, 1963](#)); ([Uman, 1964, 1963](#)); ([Uman et al., 1964](#)); ([Uman and Orville, 1964](#)); ([Orville and Uman, 1965](#)); ([Uman and Orville, 1965](#)). For instance, [Prueitt \(1963\)](#) calculated the excitation temperature of five different lightning strokes. [Uman et al. \(1964\)](#) studied the maximum possible values of the temperature, electron density, mass density of air and pressure in a lightning channel. They also discussed the continuum spectra, the opacity and the optical thickness in these papers. These quantitative analyses laid the foundation of lightning spectroscopic diagnostics.

[Orville \(1968a\)](#) recorded the first time-resolved spectra of cloud-to-ground lightning return strokes between a thundercloud and the ground. This was achieved by using slitless spectroscopy recorded on film with two high-speed streak cameras. These spectra were obtained in the 400 - 660 nm spectral range with time resolution of 2 - 5 μs and 1 nm wavelength spectral resolution that allowed recording the optical emissions of neutral hydrogen, neutral and singly ionized atoms of nitrogen and oxygen. No molecular or doubly ionized emissions were identified. The temperature estimated from these strokes showed a rising trend in the first 10

μs up to around 28000 - 31000 K and then decreased. The dynamics of electron density derived from the Stark-broadened H_α exhibited a decreasing trend from $\sim 10^{18} \text{ cm}^{-3}$ to $\sim 10^{17} \text{ cm}^{-3}$ (Orville, 1968b).

Newman et al. (1967) were the first to produce triggered-lightning strokes using a rocket carrying aloft stainless steel wire to fire a potential thundercloud lightning. Later, in the 1980s and 1990s, a new generation of fast and sensitive camera sensors were introduced thanks to the development of CCD and CMOS technology. This led to a new era of lightning and laboratory produced lightning-like discharges spectroscopy using high speed cameras. During the summers of 2012 and 2013, Walker and Christian (2017) obtained the first high-speed spectra of triggered lightning at 672000 fps ($1.5 \mu\text{s}$ of time resolution). These spectra covered different phases of a lightning flash including the initial stage, dart leader, return stroke and continuing current. Spectra of return strokes showed emission features of neutral, singly and doubly ionized nitrogen and oxygen atoms and neutral argon and hydrogen. It was the first time that doubly ionized nitrogen atoms were identified. However, no molecular species were detected in their triggered lightning spectra. Their estimations of the gas temperature and electron density in the lightning channel led to values that were far more higher than previous results: the measured temperatures exceeded $\sim 40000 \text{ K}$ and electron densities reached $\sim 10^{19} \text{ cm}^{-3}$ thanks to their high-speed recording and sensitivity (Walker and Christian, 2019).

Recently, Kieu et al. (2020) have explored spectral features of meter long lightning-like discharges in the submicrosecond time regime. They used an ultrafast spectrograph named GALIUS (Passas et al., 2019). These lightning-like discharges were recorded at 2100000 fps with time resolution of $0.416 \mu\text{s}$ (160 ns exposure time) within a reduced spectral range (645 - 665 nm). The spectra

showed the dynamics of neutral hydrogen and neutral, singly and doubly-ionized nitrogen. Even though the measured peak currents of these lightning-like discharges were quite humble (~ 3 kA) compared to peak currents in real lightning, the estimation of the temperature and electron density gave similar results: measured electron densities reached values of up to $\sim 10^{18}$ cm $^{-3}$ and the temperatures were as high as ~ 32000 K. The analyses carried out in [Kieu et al. \(2020\)](#) also indicated a possible disruption of equilibrium behind the shock front in the very early times.

Contrary to optical spectra of Transient Luminous Events (TLEs) where molecular optical emissions dominate over neutral and ionic emissions ([Hampton et al., 1996](#); [Kanmae et al., 2007](#); [Parra-Rojas et al., 2013, 2015](#); [Passas et al., 2016b](#); [Gordillo-Vázquez et al., 2018](#); [Pérez-Invernón et al., 2018](#); [Gordillo-Vázquez and Pérez-Invernón, 2021](#)), lightning spectra mostly exhibit the presence of neutral and ion lines. The presence of molecular emissions in lightning spectra is interesting since it indicates the presence of mild temperature regions and / or the activity of streamers surrounding the heated lightning channel where molecules can exist and be electronically excited.

In this paper, we focus on the time-resolved spectroscopy of several lightning-like discharges using GALIUS in different wide spectral regions: near ultraviolet-blue (380 - 450 nm), visible-near infrared (475 - 793 nm) and the near infrared (770 - 805 nm). Most molecular optical emissions were detected in the near ultraviolet-blue (380 - 450 nm) region. Spectra in the visible range exhibited features of doubly ionized nitrogen and molecular C $_2$ emissions together with the strongest light emissions from singly ionized nitrogen at 500 nm. Submicrosecond time resolution (0.714 μ s) was used to record spectra in the near-infrared where neutral oxygen triplet (777 nm and 795 nm) and singlet (715 nm) lines were distinctly

detected from the early time. We calculated the temperature and electron density from these neutrals and compared them with the results derived from other neutral (H_α at 656.30 nm) and ion (N II at 648 nm and 661 nm) lines. A discussion on these results follows in the paper.

6.2 Instrumentation and Experimental Setup

The results presented here have been obtained with an ultrafast and high spectral resolution (between 0.29 nm and 0.75 nm) spectrograph named GrAnada Lightning Ultrafast Spectrograph (GALIUS). GALIUS is a portable, ground-based spectrograph able to record spectra of natural/triggered or lightning-like discharges with submicrosecond time resolution. GALIUS can be set up with a total of 22 configurations made of combinations of 10 collector lenses (focus lengths ranging from 25 mm to 200 mm), 2 different collimator lenses in the UV and visible-NIR range (105 mm with F#4.5 and 50 mm with F#1.2) and 4 interchangeable volume-phase holographic (VPH) gratings for spectral ranges from the near-ultraviolet (380 nm) to the near infrared (805 nm) and high spectral resolution (0.29 nm to 0.75 nm depending on the grating used). More details about GALIUS and its configurations can be found elsewhere ([Passas et al., 2019](#); [Kieu et al., 2020](#)).

For all spectra presented here, GALIUS was set up in slit mode (50 μm x 3 mm), using the high-speed Photron FASTCAM SAZ camera, 12-bit ADC pixel depth constructed on a very high sensitivity (monochrome ISO 50000) CMOS sensor with sensor size of 1024 \times 1024 20 μm square pixels. In the near-ultraviolet blue range, the camera was set up with 2 collimator lenses (105 mm and 50 mm) and collector lens 50 mm (F#1.5) controlled by the grism R1 with central

wavelength in 357 nm, spectral resolution 0.29 nm and 2086 lines/mm. The recording speed in this configuration was 672000 fps (160 ns exposure time) and the spectra was recorded in the range 380 - 450 nm. In the visible-near infrared range, GALIUS used two similar collimator lenses (50 mm, F#1.2) and a collector lens (50 mm, F#1.67 for long sparks). Spectra in this region were recorded at 672000 fps (160 ns exposure time) using the grism R2 with central wavelength in 656.30 nm, spectral resolution 0.75 nm and 1015 lines/mm. This was the widest spectral range recorded. The recorded images showed spectral emissions from 475 nm up to 793 nm. Finally, the camera was set up to allow submicrosecond time resolution in the near-infrared spectral range. These spectral images were obtained at 1400000 fps (0.714 μ s time resolution and 160 ns exposure time) within the 770 - 805 nm spectral range. We used grism R4 with central wavelength in 778 nm, spectral resolution of 0.34 nm and 1727 lines/mm. The collimator and collector lenses were the same as with the set up used with grism R2.

In 2019, we moved GALIUS to the facilities of the company DENA Desarrollos in Terrassa (Spain) to work with ~ 1 meter long lightning-like discharges produced by a 2.0 MV Marx generator. This generator can produce sparks up to 900 kV in Switching Impulse (SI) and Lightning Impulse (LI) modes. The experimental setup used here can be found elsewhere (Kieu et al., 2020). In the SI mode, the voltage slowly rises up to its maximum peak in 100 μ s and then it decays in ~ 0.5 μ s. In the LI mode, the voltage rapidly reaches its peak in 0.5 μ s, keeping a plateau of 2-3 μ s and then decaying in 0.5 μ s. Opposite to voltage, the current in the SI mode reaches its peak and immediately decays while the current in the LI mode rises up fast (0.3-0.5 μ s) but decays slowly in about 100 μ s. The LI mode is most similar to triggered and natural lightning where the current rise time is relatively fast (several μ s) and the current decays in tens to

hundreds of μs (Walker and Christian, 2019). Natural lightning can exhibit peak currents much higher (15-150 kA) than the ones usually available in experimental facilities. In spite of this we have obtained similar temperatures (and only slightly lower electron densities) than obtained in natural (Orville, 1968b) and triggered lightning (Walker and Christian, 2019).

In the following sections, we will show and discuss spectra of lightning-like discharges in the SI and LI modes produced with the same voltage (800 kV) and that generates ~ 1 meter long discharges ~ 8.5 meters away from GALIUS.

6.3 GALIUS time-resolved spectra

6.3.1 GALIUS spectra in the near ultraviolet-blue (380 - 450 nm)

Time-resolved spectra in the near-ultraviolet were recorded by grism R1 at 672000 fps (1.488 μs time resolution) from 380 nm to 450 nm, as shown in Figure 6.1 for discharges generated in the LI mode. A zoom in of the spectral region between 400 nm and 425 nm is shown in Figure 6.1(b). No spectra could be recorded in the SI mode in this spectral region due to the faint luminosity and short life-time of the discharge. To identify emitting species, we have labeled these spectra with their corresponding wavelengths and ionization states, e.g. neutral nitrogen (N I), singly ionized nitrogen (N II), and doubly ionized nitrogen (N III).

Figure 6.1 shows the presence of singly ionized atomic nitrogen and oxygen, doubly ionized atomic nitrogen together and molecular optical emissions that were labeled in green, purple, blue and black color, respectively. The doubly ionized nitrogen lines at 409.7 nm, 410.3 nm were first reported by Walker and Christian (2017) but the 419.6 nm and 420.0 nm reported here were not seen before in this region. They only appear in the first frame (at 1.28 μs) of the near-ultraviolet

6.3. GALIUS TIME-RESOLVED SPECTRA

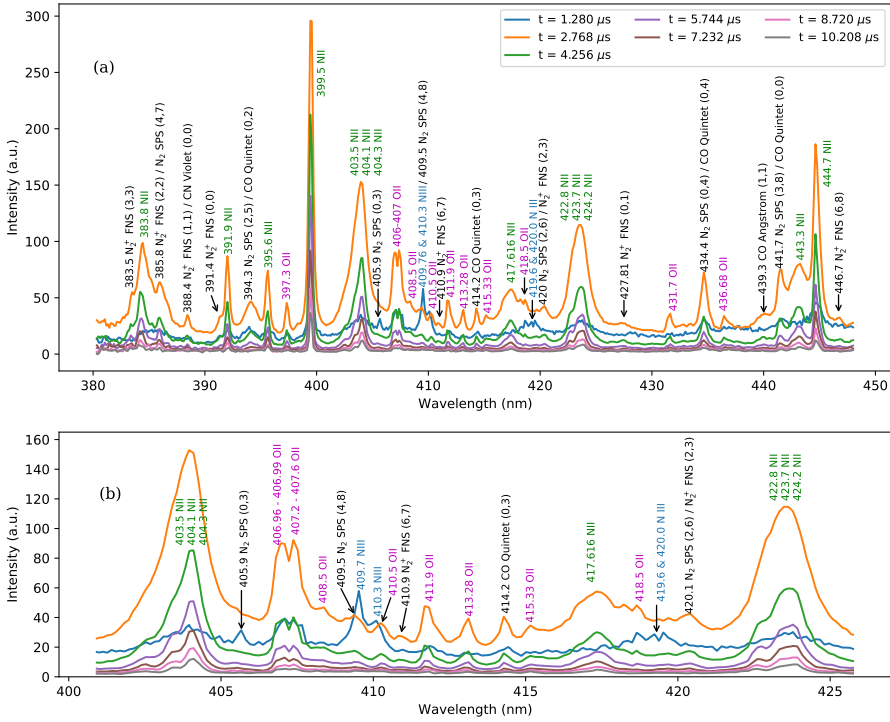


Figure 6.1: Time resolved R1 (380 - 450 nm) spectra of a meter long lightning-like discharge produced with the LI mode of a Marx generator with 800 kV. Panel (a) shows the entire spectral range. Panel (b) displays a zoom of the 400 - 425 spectral gap. The spectrum was recorded at 672000 fps (160 ns exposure time) with spectral and time resolutions of 0.29 nm and 1.488 μ s, respectively. Spectral lines of singly ionized atomic nitrogen and oxygen, doubly ionized atomic nitrogen and several molecular species (N_2 , N_2^+ , C_2 , CN, and CO) are visible and marked with green, purple, blue and black labels, respectively.

spectra. Many optical emissions in this near ultraviolet blue region are due to molecular species. Optical emissions of the CN violet band system ($B^2\Sigma^+$, $v' \rightarrow X^2\Sigma^+$, v'') contributed with the presence of the line 388.3 nm ($v' = 0 - v'' = 0$). The N_2 second positive system (SPS) shows two transitions at 394.3 nm ($v' = 2 - v'' = 5$) and 405.8 nm ($v' = 0 - v'' = 3$) (Luque and Gordillo-Vázquez, 2011), (Gordillo-Vázquez et al., 2012). The N_2^+ first negative system (FNS) can be identified by humps at 388.4 nm ($v' = 1 - v'' = 1$), 391.4 nm ($v' = 0 - v'' = 0$) and 427.81 nm ($v' =$

Molecule	System name	Transition	Measured wavelength (nm) & vibrational transition (v', v'')
N_2^+	First negative	$B^2\Sigma_u^+ - X^2\Sigma_g^+$	383.54 (3,3), 385.79 (2,2), 388.43 (1,1), 391.44 (0,0), 410.90 (6,7), 420.00 (2,3), 427.81 (0,1), 446.66 (6,8)
N_2	Second positive	$C^3\Pi_u - B^3\Pi_g$	385.80 (4,7), 394.30 (2,5), 405.94 (0,3), 409.50 (4,8), 420.05 (2,6), 434.40 (0,4), 441.70 (3,8)
CO	Ångström system	$B^1\Sigma - A^1\Pi$	439.31 (1,1)
CO	Quintet states	$a''^5\Pi - d^3\Delta$	441.60 (0,0)
CO	Quintet states	$a''^5\Pi - a'^3\Sigma^+$	394.32 (0,2), 414.20 (0,3), 434.56 (0,4)
CN	Violet system	$B^2\Sigma^+ - X^2\Sigma^+$	388.30 (0,0)
C_2	Swan band	$d^3\Pi_g - a^3\Pi_u$	516.50 (0,0)

Table 6.1: Molecular species and vibro-electronic optical transitions detected in the present study. N_2 Second Positive System (SPS) and N_2^+ First Negative System (FNS) transitions were taken from [Gilmore et al. \(1992\)](#) and [Camacho et al. \(2007\)](#). Transitions of CO were taken from [Czech et al. \(2013\)](#) and [Al-Tuwirqi et al. \(2012\)](#). Transitions from C_2 and CN were taken from [Wallace \(1960, 1964\)](#), and [Czech et al. \(2012\)](#)

0 - $v'' = 1$). Some of these lines were earlier reported in lightning spectra ([Wallace, 1960](#); [Salanave et al., 1962](#)). After these early molecular detections, there were no modern reports on molecular emissions in lightning spectra.

Our R1 (near-ultraviolet blue) spectra includes the presence of traces of several CO optical emissions associated to the CO Ångström ($B^1\Sigma, v' \rightarrow A^1\Pi, v''$) and Quintet systems ($a''^5\Pi, v' \rightarrow a'^3\Sigma^+, v''$ and $a''^5\Pi, v' \rightarrow d^3\Delta, v''$). In particular, we found the lines 394.32 nm, 414.20 nm, 434.56 nm, 441.6 nm and 439.31 that belong to the (0, 2), (0, 3), (0, 4), (0, 0) and (1, 1) vibrational transitions of the Quintet and Ångström systems, respectively. In addition, three transitions associated to the CO Quintet system overlap with optical emissions of the N_2 second positive system. Table 1 shows all the molecular transitions detected and

displayed in Figure 6.1.

The presence of ground state and electronically excited CO in lightning-like discharges could be explained by the action of thermal dissociation of CO₂ (CO₂ → CO (X¹Σ_g, v ≥ 0) + O(³P)), electron-impact dissociation of CO₂ (CO₂ + e → CO (X¹Σ_g, v ≥ 0) + O(³P) + e), N + CO₂ → NO + CO (X¹Σ_g, v ≥ 0) and electron-impact excitation of ground state CO (CO(X¹Σ_g, v ≥ 0) + e → CO(B¹Σ, a''⁵Π, a''⁵Π, v ≥ 0) + e) taking place in the shocked air surrounding the lightning-like channel, which is cooled rapidly by hydrodynamic expansion (Levine et al., 1979; Ripoll et al., 2014). This mechanism would prevent CO from further dissociation and could support the detection of CO (Levine et al., 1979). If, on the contrary, CO was produced in the slower-cooling inner core of the lightning channel, no CO would be produced (it would have been lost by thermal dissociation) and no CO would be detected (Levine et al., 1979). Once ground-state CO(X¹Σ_g) is produced, excited electronic states producing Ångström and Quintet states can be produced by thermal and / or electron-impact excitation.

It is interesting to note that although traces of CO are detected in the present spectroscopic analysis of lightning-like discharges as well as with chemical detectors in previous studies (Levine et al., 1979), global atmospheric chemistry circulation models predict that CO is slightly depleted by the action of lightning (Murray, 2016; Gordillo-Vázquez et al., 2019). A possible explanation for this could be that once CO is produced in the lightning channel, it is depleted by reactions involving lightning produced OH and ground state oxygen atoms O(³P) like CO + OH → CO₂ + H, CO + OH + O(³P) → CO₂ + OH and CO + OH + O₂ → CO₂ + HO₂.

The detection of C₂ and, in particular, the formation of C₂(d³Π_g, v) underlying the Swan band optical emissions can be explained in terms of the presence of

$\text{CO}(X^1\Sigma_g, v)$ in the lightning-like channel. At relatively high temperatures (4000 - 6000 K) typical of air in the edge of the expanding channel of a lightning-like discharge, ground state $\text{C}(^3\text{P})$ atoms can be efficiently produced through the reaction $\text{CO}(X^1\Sigma_g, v_1) + \text{CO}(X^1\Sigma_g, v_2) \rightarrow \text{CO}_2 + \text{C}(^3\text{P})$ (Carbone et al., 2020). Once $\text{C}(^3\text{P})$ is formed, Little and Browne (1987) proposed a possible three step mechanism for the formation of $\text{C}_2(d^3\Pi_g, v)$ producing the Swan band through: (1) $\text{C}(^3\text{P}) + \text{C}(^3\text{P}) + \text{M} \rightarrow \text{C}_2(^5\Pi_g, v) + \text{M}$, (2) $\text{C}_2(^5\Pi_g, v) + \text{M} \rightarrow \text{C}_2(^5\Pi_g, v=0) + \text{M}$ and (3) $\text{C}_2(^5\Pi_g, v=0) + \text{M} \rightarrow \text{C}_2(d^3\Pi_g, v=6) + \text{M}$, where $^5\Pi_g$ is a metastable (quintet) state for which a crossing exists between the $v=6$ level of the $d^3\Pi_g$ and the $v=0$ of the $^5\Pi_g$ state (Carbone et al., 2020).

The presence of CN and its violet band (due to the radiative deexcitation of $\text{CN}(B^2\Sigma^+)$) in the R1 spectra can be explained by competing mechanisms for the formation of C_2 and CN that promote and go in favor of the formation of CN in a N_2 rich environment like air. According to Dong et al. (2014), once atomic carbon and molecular C_2 are available, CN radicals can be formed by $\text{C}(^3\text{P}) + \text{N}_2 \rightarrow \text{CN}(X^2\Sigma^+) + \text{N}$, $\text{C}(^3\text{P}) + \text{N} \rightarrow \text{CN}(X^2\Sigma^+)$ and $\text{C}_2 + \text{N}_2 \rightarrow 2 \text{CN}(X^2\Sigma^+)$, $\text{C}_2 + 2 \text{N} \rightarrow 2 \text{CN}(X^2\Sigma^+)$. The excitation energy of $\text{CN}(B^2\Sigma^+)$ is about 3 eV so that it can be easily produced by thermal and / or electron-impact excitation of ground state $\text{CN}(X^2\Sigma^+)$ in the lightning-like channel. Alternative kinetic mechanisms for the formation of $\text{CN}(X^2\Sigma^+)$ and $\text{CN}(B^2\Sigma^+)$ would require the presence of the metastable $\text{N}_2(A^3\Sigma_u^+)$ through $\text{CO}(X^1\Sigma_g) + \text{N}_2(A^3\Sigma_u^+) \rightarrow \text{CN}(X^2\Sigma^+) + \text{NO}$ and $\text{CN}(X^2\Sigma^+) + \text{N}_2(A^3\Sigma_u^+) \rightarrow \text{CN}(B^2\Sigma^+) + \text{N}_2$ (Crispim et al., 2021). These reaction paths should also be possible in mild temperature regions of the lightning-like channel so that ground state N_2 can be excited by electron collisions before dissociation occurs.

Figure 6.2 shows the fit of synthetic spectra of heated humid (80 % relative

humidity (RH)) air to the measured R1 spectra (normalized with respect to the 399.5 nm N II ion line) corresponding to the early times (from 1.28 μs to $\sim 10.20 \mu\text{s}$) of a meter long Lightning Impulse (LI) discharge. As time increases the measured gas temperatures decreases. The synthetic spectra are based on equilibrium calculations of thermal air plasmas (see supporting information 5.8 of chapter 5). Calculated spectra include all possible lines of atoms, singly and doubly ionized ions that can appear in the R1, R2 and R4 spectral ranges explored in this study and considered in [Kramida et al. \(2015\)](#). The only molecular species considered is N_2 and, in particular, the Lyman-Birge-Hopfield (LBH) band, First Positive System (FPS) and Second Positive System (SPS). Stark broadening of nonhydrogenic ([Bekefi, 1976](#)) and hydrogenic lines ([Griem, 1964](#)) are included and convolved with instrumental broadening (0.29 nm for R1 and 0.75 nm for R2) using the measured electron densities and gas temperatures. Since no electron densities could be measured in the near ultraviolet-blue spectral range using grism R1, we used the electron concentrations measured with grism R3 (see panel (b) in [Figure 6.6](#)) in our previous paper since the spectral resolutions of R1 and R3 are similar ([Kieu et al., 2020](#)). From the measured R1 gas temperatures (see panel (d) in [Figure 6.6](#)), the corresponding equilibrium concentrations and partition functions of chemical species (atoms, ions and molecules) were calculated to generate the synthetic spectra.

The agreement between synthetic and measured R1 spectra is fine except for some N II ion lines (383.8 nm, 403.5 nm, 404.1 nm, 404.3 nm, 417.6 nm, 422.8 nm, 423.7 nm and 424.2 nm), which predicted intensities are below the measured values and a few transitions of CO and of the N_2^+ First Negative System (FNS) not included in the synthetic spectra calculation. Since the measured R1 spectra mostly include ionic emissions, their intensity rapidly decreases as the gas

temperature evolves towards lower values. For instance, the strong N II ion lines at 399.5 nm and 444.7 nm fade away as time evolves.

The use of simulated spectra is justified because they contribute to detect the limits of our knowledge (accuracy of available spectroscopic constants and calculated Stark broadening mechanisms) and model approximations (equilibrium assumptions).

6.3.2 GALIUS spectra in the visible-near infrared (475 - 793 nm)

Time-resolved spectra in the visible-near infrared range from 475 nm to 793 nm were recorded with grism R2 at 672000 fps as shown in Figures 6.3(a) and 6.3(b, c) for ~ 1 m long - 800 kV discharges in SI and LI modes, respectively. We can see in the first frame (at $t = 0.930 \mu\text{s}$ (SI mode) and $t = 1.250 \mu\text{s}$ (LI mode), see panel (b)) of both figures the sharp rising of the singly ionized nitrogen (N II) at 500 nm. Then, in the second frame (at $t = 2.418 \mu\text{s}$ (SI mode) and $t = 2.738 \mu\text{s}$ (LI mode), see panel (b)), the 500 nm ion line reaches its maximum intensity. Similarly, Figure 6.3 also shows the evolution dynamics of the 777 nm neutral oxygen line with its rising from the first frame to its maximum at later times of around $\sim 2.418 \mu\text{s}$ and $\sim 8 - 10 \mu\text{s}$ for the SI and LI modes, respectively. The maximum intensity of the 500 nm N II line is much larger than the peak of the 777 nm O I line in these early times. However, the neutral 777 nm O I line lasts much longer (see panel (c)) than the singly ionized 500 nm N II line. The explanation for this is that ion emissions appear in the early time and remain excited only for a short time (a few microseconds) while the neutral emissions appear later but last much longer since they are easier to excite.

The second interesting feature in the R2 spectra of Figure 6.3 is the presence of a line at ~ 517 nm. This line was first identified by Orville (1968a) in an

attempt to prove the existence of singly ionized oxygen lines in lightning spectra. However, when Orville (1968a) used it to calculate temperatures, the result yielded too high values in the range 40000 K - 70000 K which considerably exceeded the temperature values 20000 K - 30000 K previously derived by the same authors (Orville, 1968b). The singly ionized oxygen line at 517.5 nm seems to be a weak one (Kramida et al., 2015). This means that the line in this position of the R2 spectra may result from the overlapping of that oxygen ion line and another emission lines from other species. In particular, the C₂ emission at 516.5 nm corresponds to the band head (0 - 0) which is the strongest transition in the C₂ Swan band system (see section 3.1). Therefore, it could be very possible that the recorded emission at ~ 517 nm corresponds to the overlapping of the C₂ (0 - 0) 516.5 Swan band and the singly ionized oxygen at 517.5 nm that could not be well resolved because of the limited spectral resolution (0.75 nm) of the R2 spectra.

Finally, other interesting line emissions present in the R2 spectra are those of several doubly ionized nitrogen at 485.8 nm, 486.7 nm, 532.0 nm and 532.7 nm in early times (from 0.93 μ s to ~ 2 μ s). These ion lines were recently identified in triggered lightning return stroke spectra recorded at 672000 fps (Walker and Christian, 2017). However, in their identification the doubly ionized nitrogen lines were only present in the first frame of their spectra.

Figure 6.4 shows the fit of synthetic spectra of heated humid (80 % RH) air to the measured R2 spectra (normalized with respect to the 500 nm N II ion line) corresponding to the early times (from 1.250 μ s to ~ 10.178 μ s) of a meter long Lightning Impulse (LI) discharge. In a time gap of ~ 9 μ s the measured gas temperatures decrease from ~ 34000 K to ~ 17000 K as derived from the ratio of the 648 nm and 661 nm N II ion lines (see Figure 6.6(e)). The R2 synthetic spectra were calculated using as inputs the measured R2 electron

densities (obtained from the H_α line) and gas temperatures (see Figure 6.6). From the measured gas temperatures, the corresponding equilibrium concentrations and partition functions of chemical species (atoms, ions and molecules) were calculated to generate the corresponding R2 synthetic spectra.

There is a reasonable agreement between synthetic and measured R2 spectra except for the 656.30 nm H_α line and the 567.9 nm line of the N II ion, which predicted intensities are below the measured values. The 777 nm line of O I is not well matched at 2.738 μs . On the other hand, the C_2 Swan band peak at 516.5 nm was not included in the synthetic spectra calculation and so there is no synthetic line able to match that peak.

6.3.3 GALIUS spectra in the near-infrared (770 - 805 nm)

In the near-infrared spectral region we focus the study on the dynamics of two neutral oxygen triplet lines at 777 nm and 795 nm. Their spectra were recorded at 1400000 fps with submicrosecond time resolution (0.714 μs and 160 ns exposure time) as shown in Figure 6.5. The spectra recorded in this spectral range did not exhibit any molecular emissions. Figure 6.5(a, b) and 6.5(c, d) show the optical emissions from ~ 1 m long spark produced with 800 kV in the SI and LI modes, respectively. The neutral O I line at 777 nm is in reality a triplet with sublines at 777.19 nm, 777.42 nm, 777.54 nm. The O I line at 795 nm is also the combination of three lines at 794.75 nm, 795.08 nm, 795.21 nm. These two triplet O I lines are among the longest lasting emission lines in lightning spectra, around 25 μs in the SI mode and about 100 μs following the duration of the input current of the LI mode. Neutral emissions usually appear a bit later but last longer than ion lines (Walker and Christian, 2019; Kieu et al., 2020). In spite of this, the emergence of the 777 nm line can be seen in a time as early as 0.25 μs in the SI mode (see Figure

6.5(b)) and $\sim 0.55 \mu\text{s}$ in the LI mode (see Figure 6.5(d)). The emergence of the 795 nm line is weaker than the 777 nm one because, though they have very similar Einstein coefficients, the excitation energy of the 795 nm triplet is higher (~ 14.04 eV) than that of the 777 nm triplet (~ 10.73 eV). It is interesting to note that, as it is seen from high speed photometric recordings from space, lightning 777 nm optical radiation inside thunderclouds has a duration of several milliseconds due to scattering by water and/or ice particles before it is finally absorbed (Luque et al., 2020; Soler et al., 2020). Lightning near-infrared optical emissions inside thunderclouds are more absorbed than near-ultraviolet and blue radiation (Luque et al., 2020).

The non-scattered (by clouds) lightning 777 nm optical emission (mainly connected to the heated channel luminosity) is of interest for diagnostic purposes since its temporal dynamics closely follows that of lightning currents (Fisher et al., 1993; Cummer et al., 2006; Walker and Christian, 2019; Kolmašová et al., 2021). It is also tightly correlated to the distant quasi-static (≤ 0.1 Hz to 400 Hz) magnetic field signature attributed to lightning continuum currents that have been associated to delayed sprites (Cummer and Füllekrug, 2001; Cummer et al., 2006). Recent results by Kolmašová et al. (2021) have demonstrated that, in addition to high-peak current of causative lightning strokes, the velocity of the current wave and the conductivity of the heated channel of the return stroke are important factors that control the intensity of elves. Cho and Rycroft (1998) had previously shown that the amplitude and the rise time of lightning affect the intensity of elves. The amplitude relates to the lightning channel conductivity and the rise time influences the current wave velocity of the lightning return stroke pulse.

The electrical conductivity of the (heated) lightning channel can be affected by the ambient relative humidity which depends on season, environment i.e. coastal,

maritime or inland, and regional climate. For instance in high altitude plateaus the conductivity can be up to 20 % - 40 % lower (Guo et al., 2009). We have explored the temporal dynamics of the electrical conductivity in a spot of the heated, highly ionized lightning-like channel.

6.4 Quantitative analysis: Electron density, Temperature and Electrical conductivity

6.4.1 Electron density

Stark broadening is often used to estimate the electron density in lightning discharges (Uman et al., 1964; Orville, 1968b; Walker and Christian, 2019). The advantage of this method is that Stark broadening is independent of assumptions on the equilibrium state of the plasma. Consequently, electron densities are usually derived from the full width at half maximum (FWHM) of a line profile. However, it is well-known that ion dynamics affects both the line widths and their shapes. This effect is especially important for the H_α and H_γ lines but it is nearly negligible for the line H_β (Gigosos et al., 2003). Therefore, Gigosos et al. (2003) suggested an alternative method to calculate the electron density from the Stark broadening of the H_α line using the Full Width at Half Area (FWHA) of the H_α with the equation:

$$N_e = 10^{17} \times \left(\frac{\text{FWHA}}{1.098} \right)^{1.47135} \text{cm}^{-3}. \quad (6.1)$$

Electron densities obtained from the FWHA of the Stark broadened H_α line in the visible-near infrared spectra (using grism R2) recorded at 672000 fps are shown in Figure 6.6(a) and 6.6(b) (see red line) for ~ 1 meter long sparks in the SI

and LI modes, respectively. For comparison, electron densities derived from short spectral range (using grism R3) recorded at 2100000 fps are also shown in Figure 6.6(a) and 6.6(b) (see yellowish dots and line). Even though our electron densities are obtained from lightning-like discharges the results are similar to those derived by Orville (1968b) in real lightning.

For comparison with the FWHA method, the full width at half maximum (FWHM) of a Stark broadened line can also be used to estimate the concentration of electrons. Griem (1964) provided a convenient equation (see below) to derive electron densities from the Stark FWHM broadening of spectral lines corresponding to neutral or singly ionized atoms:

$$\Delta\lambda_{Stark}[\text{\AA}] \simeq 2\omega(T)\frac{n_e[cm^{-3}]}{10^{16}}, \quad (6.2)$$

where $\omega(T)$ is a tabulated function (in units of \AA) that depends on the temperature and on the line transition wavelength considered. Equation (2) is only valid for electron densities in the range $10^{16} - 10^{18} \text{ cm}^{-3}$ and it provides values of the electron density with an error within 20 % – 30 %. Griem's calculation for $\omega(T)$ only considered the broadening of the 777.19 nm, the strongest subline in the 777 triplet. For this subline $\omega(T)$ varies between $1.99 \times 10^{-2} \text{\AA}$ at 2500 K and $5.56 \times 10^{-2} \text{\AA}$ at 40000 K (Griem, 1964). To make the calculation more precise, we interpolated the tabulated function $\omega(T)$ and measured the $\Delta\lambda_{Stark}$ of the 777.19 nm subline extracted from the full Stark broadening of the triplet. To find out the FWHM of each subline belonging to the triplet 777 nm, we built a triplet Lorentzian function (L_3) to fit the experimental data. Since the O I 777 nm triplet is the combination of sublines 777.19 nm, 777.41 nm, and 777.53 nm with relative intensities 870, 810 and 750 (Kramida et al., 2015), the Lorentzian

function (with six fitting parameters) for the 777 nm triplet line can be written as:

$$L_3 = k + \frac{870}{810} \times \frac{I}{\pi} \frac{\sigma_1}{(\lambda - \lambda_c + a)^2 + \sigma_1^2} + \frac{I}{\pi} \frac{\sigma_2}{(\lambda - \lambda_c)^2 + \sigma_2^2} + \frac{750}{810} \times \frac{I}{\pi} \frac{\sigma_3}{(\lambda - \lambda_c - b)^2 + \sigma_3^2} \quad (6.3)$$

where k , I , λ_c and σ_1 , σ_2 , σ_3 are the background of the fitting, the intensity and wavelength of the central subline of the triplet, and the broadenings of the sublines 777.19 nm, 777.41 nm, and 777.53 nm, respectively. The numerical values $a = 0.223$ and $b = 0.122$ are the shifts of the lateral wavelengths with respect to the central line of the triplet.

Figure 6.7 shows the resulting Lorentzian fit of the triplet 777 nm for spectra recorded with grism R4 in the Switching mode (a) at $0.964 \mu\text{s}$ and in the Lightning mode (b) at $4.12 \mu\text{s}$. The fitting coefficients in the SI and LI modes for k , λ_c , I , σ_1 , σ_2 and σ_3 are 0.13, 777.50 nm, 9.15, 0.62, 0.65, 0.58, and 2, 777.60 nm, 100, 0.405, 0.474, 0.356. The resulting central wavelengths (777.50 nm and 777.60 nm) are not exactly 777.41 nm because of slight wavelength calibration detuning during the SI and LI mode spectral recording.

The electron densities obtained from the Stark broadening of the 777.19 nm subline of the O I 777 nm triplet for spectra recorded with gratings R4 and R2 are shown in Figures 6.6(a) and 6.6(b) (see green and pink lines for R4 and R2, respectively) for the SI and LI modes of a ~ 1 meter long spark produced with a peak voltage of 800 kV. We see that the maximum electron density derived from the 777.19 nm always stays above the one obtained from the H_α spectral line (656.30 nm) and it seems to flatten at later times ($\sim 4 \mu\text{s}$ and $\sim 10 \mu\text{s}$ for the SI and LI modes, respectively). This might be due to the fact that the

FWHM method is less sensitive when the broadening of the line is not sufficiently large. We conclude that the analysis of the FWHM could be used as a first rough estimate of the electron density. The FWHA under the Stark broadened H_α line seems to be more sensitive (than the FWHM) to the time dynamics of the electron concentration within the heated channel.

6.4.2 Temperature

The most common method to determine the temperature of a hot plasma channel is to measure the relative intensities of different spectral lines of the same species. To calculate the gas temperature from the time resolved spectra of lightning-like discharges recorded in this work, we will assume the criteria previously established by Prueitt (1963) and Uman (1969a), and also recently used by Walker and Christian (2019) for deriving the gas temperature in triggered lightning. In particular, we consider that (a) the channel of the lightning-like discharge is optically thin (there is no light absorption through the line of sight), (b) the temperature is relatively uniform along the lightning-like channel radial cross section (temperatures are similar at the edge and the center of the lightning channel) and (c) that thermal equilibrium controls the concentration of the different atoms and ion energy levels emitting light due to spontaneous radiative deexcitation, that is, the density of excited atoms and ions follow Boltzmann's law. We also assume that local thermal equilibrium (LTE) applies so that the derived electron temperature equals the gas temperature.

Therefore, the gas temperature is calculated from the intensity ratio of different pairs of lines depending on the grism used and assuming that the corresponding emitting energy levels are populated following Boltzmann's equilibrium law. In particular, for the near-ultraviolet blue spectra recorded with grism R1, we used

two singly ionized nitrogen lines at 399.5 nm and 444.7 nm. For visible-near infrared spectra recorded with grism R2 we used the pair of lines at 648 nm and 661 nm associated with singly ionized nitrogen, and the pair of O I neutral lines 715 nm and 777 nm. Details of these calculations can be found in [Kieu et al. \(2020\)](#). Finally, for spectra recorded with grism R4 in the near-infrared the temperature was calculated from the ratio of the line intensities of the triplets 777 nm and 795 nm.

The estimation of the error in the electron temperature is evaluated with equation (11) in [Walker and Christian \(2019\)](#) that depends on the uncertainties in the intensity ratio and assuming a 10 % uncertainty in the tabulated Einstein coefficients ([Kramida et al., 2015](#)). The uncertainty in the intensity ratio is calculated using the bootstrap method also adopted to quantify the error in the electron density.

Figure 6.6(c, d) show the temperatures for, respectively, the meter long SI (Figure 6.6(c)) and LI (Figure 6.6(d)) discharges. The use of the pair of ionic lines 648 nm and 661 nm provide consistent temperature values with each other when used with spectra obtained with gratings R2 and R3 recorded at 672 kfps and 2.1Mfps, respectively. The pair of N II ion lines 399.5 nm and 444.7 nm in the spectra recorded at 672 kfps with grism R1 (only for LI discharges) also provide consistent temperature values with those derived with gratings R2 and R3. The temperatures measured with ion lines can only be tracked for relatively short times between 2 - 4 μs (SI mode) and up to $\sim 10 \mu\text{s}$ (LI mode). However, when neutral lines (O I 777 nm and 795 nm, or O I 777 nm and 715 nm) are employed the obtained temperatures are slightly lower (maximum of ~ 28000 K) than the ones obtained when with ion lines (maximum of ~ 33000 K) but can be tracked for longer times (than with ion lines) between $\sim 11 \mu\text{s}$ (SI mode) and $\sim 50\text{-}60 \mu\text{s}$ (LI

mode) since neutral lines last longer. These results resemble those derived from 5 meter long lightning-like discharges in air produced with 6.4 MV by Orville et al. (1967), where it was mentioned that the ion radiation is mostly emitted from the hotter region of the channel while the neutral radiation is emitted from the cooler regions. Finally, it should be noticed that, since the 715 nm line of O I is weaker than the 795 nm line of O I, the derived temperature can be followed for shorter times when evaluated from R2 spectra (compared to R4 spectra that include the O I line at 795 nm).

6.4.3 Time dynamics of the electrical conductivity

Once the electron concentration and gas temperature are known we can estimate the variation in time of the electrical conductivity in the heated (and highly ionized) lightning-like channel. We assume isotropic collisions so that the momentum transfer cross section $\sigma_{tr} = \sigma_c$, with σ_c being the cross section for electron-neutral collisions. Since the heated channel is highly ionized ($N_e/N \geq 10^{-3}$), it is reasonable to assume that the ion (N_i) and electron (N_e) densities are similar ($N_i = N_e$) and, consequently, the effective collision frequency for momentum transfer $\nu_m = Nv\sigma_{tr} + N_e v\sigma_{Coulomb} \simeq N_e v\sigma_{Coulomb}$, where N is the gas density, v is the mean thermal velocity of electrons and $\sigma_{Coulomb}$ is the cross section of electron-ion collisions dominated by Coulomb forces. For instance, for electron (and gas) temperatures ($T_e = T$) ~ 1 eV (11600 K) and $N_e = 10^{13} \text{ cm}^{-3}$, $\sigma_{Coulomb} \simeq 2 \times 10^{-13} \text{ cm}^2$, while $\sigma_{tr} \simeq 10^{-16} - 10^{-15} \text{ cm}^2$ (Raizer, 1991). Thus, we can consider that the electrical conductivity σ in the heated lightning-like channel is controlled by $\sigma_{Coulomb}$ as $\sigma = e^2 N_e / m \nu_m =$ (with e and m being the electron charge and mass, respectively) $= 1.9 \times 10^4 \times T_e(\text{eV})^{1.5} (\ln\Lambda)^{-1} \text{ S m}^{-1}$ with $\ln\Lambda = 13.57 + 1.5 \log(T_e(\text{eV})) - 0.5 \log(N_e (\text{cm}^{-3}))$ (Raizer, 1991). According to Figure 6.8 the elec-

trical conductivity decreases from $1.35 \times 10^4 \text{ Sm}^{-1}$ to $6 \times 10^3 \text{ Sm}^{-1}$ (approximately a factor of two) in $\sim 50 \mu\text{s}$ mostly following the decay time scale of the temperature (see Figure 6.6(d)) from $\sim 27000 \text{ K}$ to $\sim 15000 \text{ K}$. This indicates that high current flows are only favored in the very early times of a cloud-to-ground lightning stroke. The conductivity values obtained in this study are slightly smaller than those previously reported ($\sim 1.6\text{-}2.2 \times 10^4 \text{ Sm}^{-1}$) using non-time resolved lightning spectra of cloud-to-ground strokes (Guo et al., 2009). Interestingly, our conductivity values are higher and close to those recently reported in stepped leader tips ($\sim 4.3 \times 10^3 \text{ Sm}^{-1}$) and dart stepped leaders ($\sim 1.1 \times 10^4 \text{ Sm}^{-1}$), respectively, where, by using $20 \mu\text{s}$ slit-less spectroscopy, the measured electron densities and gas temperatures were $\sim 10^{15} \text{ cm}^{-3}$ (stepped leader tip), $\sim 10^{17} \text{ cm}^{-3}$ (dart-stepped leader) and $\sim 15000 \text{ K}$ (stepped leader tip) and $\sim 22000 \text{ K}$ (stepped dart leader) (Zhang et al., 2020).

6.5 Conclusions

In this paper we reported on high-speed time-resolved spectroscopic analysis of lightning-like discharges recorded by a fast and very sensitive spectrograph named GALIUS. The spectra were recorded in three separate spectral regions: near-ultraviolet blue (380 - 450 nm), visible - near infrared (475 - 793 nm) and near-infrared (770 - 805 nm). GALIUS spectra in the near-ultraviolet blue range, recorded at 672000 fps (time resolution $1.488 \mu\text{s}$), exhibited early time optical emissions associated to singly ionized nitrogen, oxygen, doubly ionized nitrogen and several molecular species. In addition to the spectral features of the CN violet transition, N_2 second positive system and N_2^+ first negative system reported in some previous studies, we found spectroscopic signatures of optical emissions due

to the Swan band (516.5 nm) of C_2 and of several electronically excited states of CO. These molecular species could exist in the mild temperature regions of lightning-like plasma channels and / or could be produced due to the chemical activity of streamers surrounding a heated lightning channel. Spectra in the visible - near infrared range (475 - 793 nm) exhibited the strongest optical emission from singly ionized nitrogen 500 N II lasting from the onset of the discharge to about 10 μs .

Molecular species such as CN and N_2 were found in high-temperature (6000 - 7000 K) combustion environments accompanied with nitrogen oxide (NO) optical emissions in the 140 nm - 340 nm spectral range (Hornkohl et al., 2014). While the 140 - 340 nm spectral gap is presently outside the detection range of GALIUS, our detection of molecular emissions in lightning-like channels opens the door to detect and quantify NO production by lightning using high sensitivity spectroscopic techniques. We speculate that the sensitivity of the sensor can play a key role in determining the presence of molecular species in lightning spectra.

The spectra recorded in the near infrared at 1400000 fps (time resolution 0.714 μs) showed the dynamics of two distinct O I triplets at 777 nm and 795 nm. Optical emissions from the 777 nm triplet, which are the strongest ones, begin almost at the onset of the discharge at about 0.25 - 0.55 μs and last up to $\sim 100 \mu s$ following the input current. These O I triplets and the O I 715 nm line were used to calculate the gas temperature inside the lightning-like channel. The gas temperature was also evaluated from the ratio of two pairs of N II ion lines (648 nm and 661, and 399.5 and 444.7 nm) and compared with the temperature derived from pairs of neutral O I lines. The temporal dynamic of the gas temperatures is conditioned by the lifetime of ion and neutrals lines. Thus, while the final temperatures are roughly the same (~ 15000 K) for the Lightning Impulse (LI)

mode, ionic lines can provide more reliable temperatures in the early times ($\leq 2 \mu\text{s}$) but neutrals can be followed longer and can better account for the thermal relaxation of the lightning-like channel.

We have completed our measurements with simulated spectra. The comparison between measured and synthetic spectra reveal some disagreements that could be due to inaccuracies of available spectroscopic constants, calculated Stark broadening mechanisms and/or underlying model approximations (equilibrium assumptions).

Finally, the concentration of electrons within the heated channel was determined by the analysis of the Stark broadening of spectral lines. We compared the electron densities resulting from the FWHA under the H_α line, and from the FWHM of the neutral 777.19 nm O I line. For the H_α broadening, electron densities were in a good agreement with those obtained in real lightning (Orville, 1968b) but the estimations from the FWHM of the 777.19 nm overestimated electron number concentrations and can be considered as a rough estimation.

6.5. CONCLUSIONS

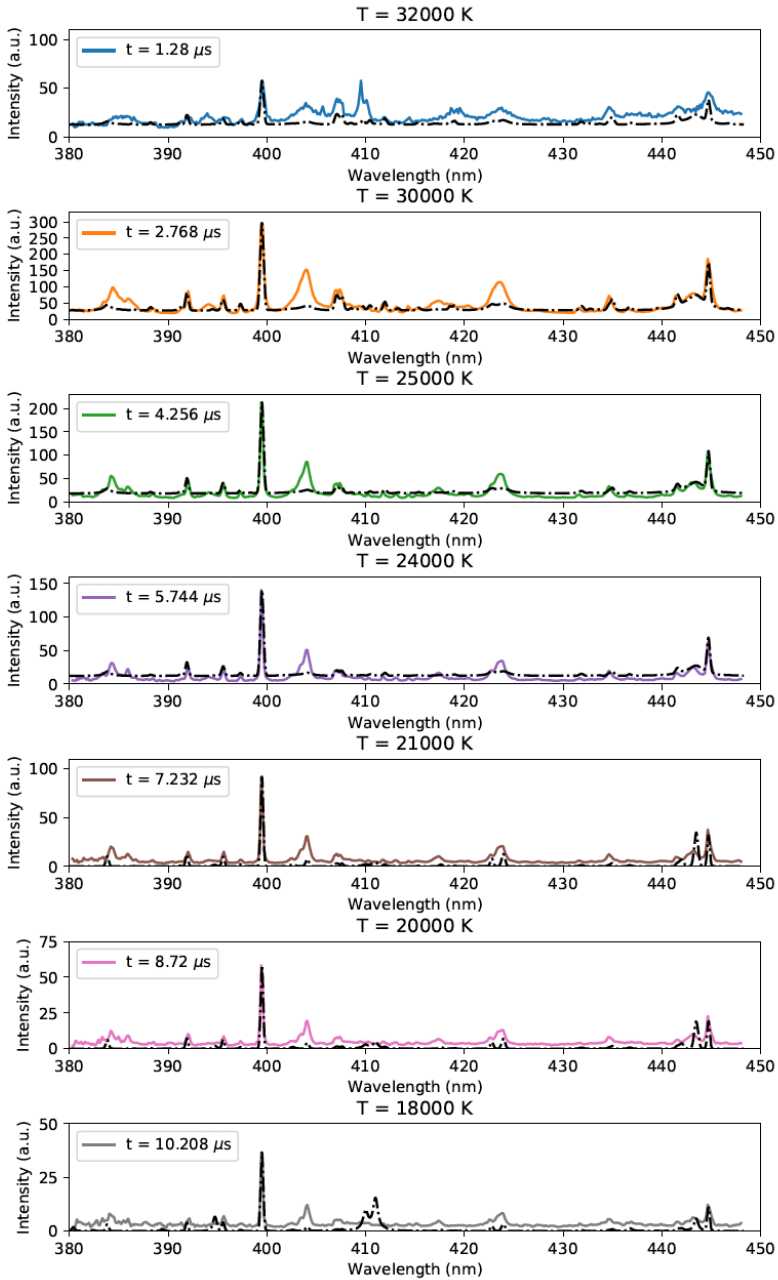


Figure 6.2: Comparison between calculated synthetic spectra (black dashed dotted line) of heated humid (80 % RH) air and measured R1 (380 - 450 nm) spectra (color line) of a meter long Lightning Impulse (LI) discharge produced with a peak voltage of 800 kV. Note that synthetic spectra do not include molecular species except for the Lyman Birge Hopfield (LBH), Second Positive System (SPS) and First Positive System (FPS) bands of N_2 .

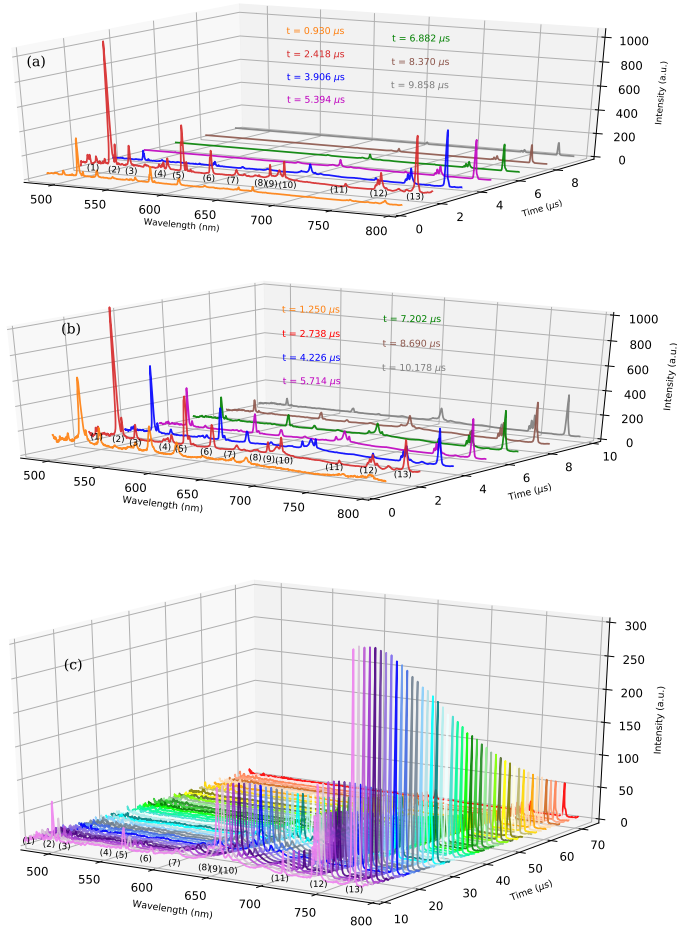


Figure 6.3: Time resolved R2 (475 - 793 nm) spectra of a meter long lightning-like discharge produced with the SI mode (panel (a)) and LI mode (panels (b) and (c)) of a Marx generator with 800 kV. For easier comparison between SI and LI mode spectra, panels (a) and (b) show similar time range (but not exactly the same). Panel (c) for LI mode show spectra for times starting in 10.178 μs . The spectra were recorded at 672000 fps (160 ns exposure time) with spectral and time resolutions of 0.75 nm and 1.488 μs , respectively. Spectral lines of neutrals (O I, N I, H I), singly ionized atoms (N II, O II) and the C₂ Swan band head at 516.5 nm are visible. Note that the numbers stand for: (1) 485.8 - 486.7 N II, (2) 500.1 - 500.5 nm N II, (3) 516.5 nm C₂ / O II, (4) 553.5 nm N II, (5) 567.9 - 571.0 N II, (6) 592.7 - 594.1 N II, (7) 616.8 nm N II, (8) 648.2 nm N II, (9) 656.3 nm H I, (10) 661.0 N II, (11) 715.6 O I, (12) 742.4-744.3-746.8 nm N I, (13) 777.4 nm O I.

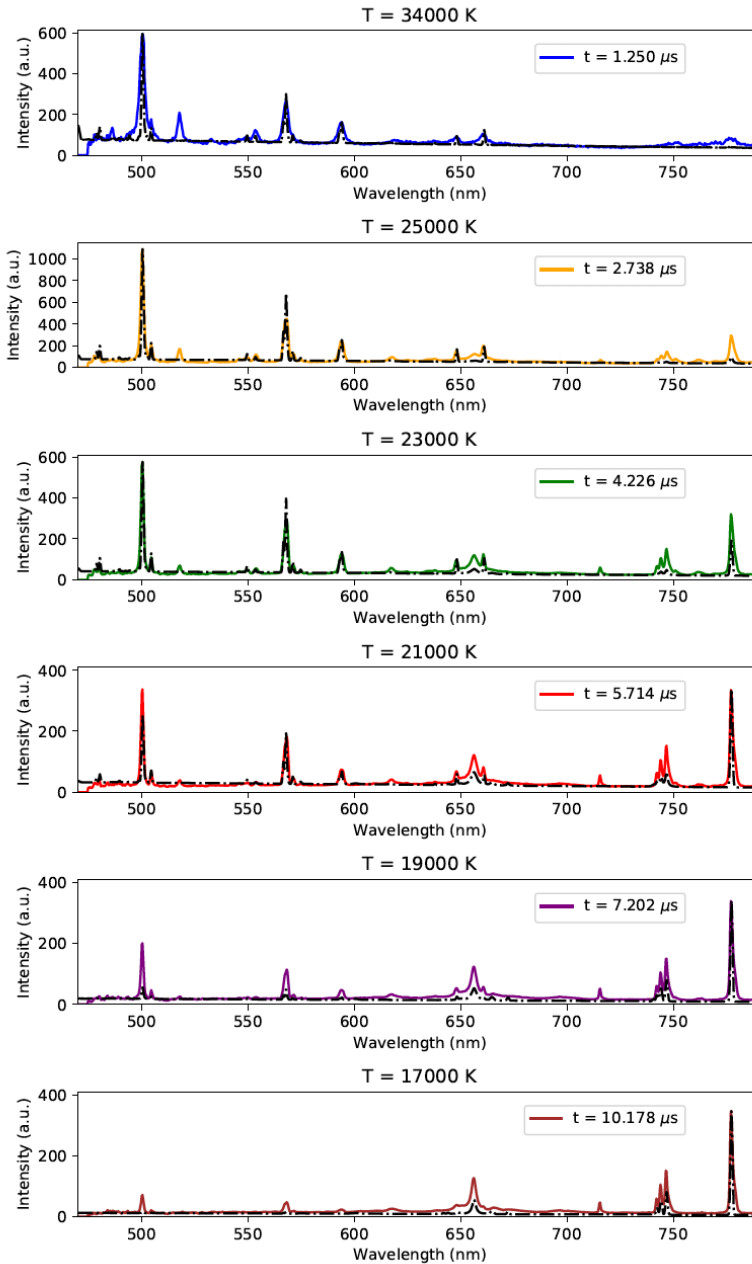


Figure 6.4: Comparison between calculated synthetic spectra (black dashed dotted line) of heated humid (80 % RH) air and measured R2 (475 - 793 nm) spectra (color line) of a meter long Lightning Impulse (LI) discharge produced with a peak voltage of 800 kV. Note that synthetic spectra do not include molecular species except for the Lyman Birge Hopfield (LBH), Second Positive System (SPS) and First Positive System (FPS) bands of N_2 . The peak associated to the C_2 Swan band is visible at 516.5 nm.

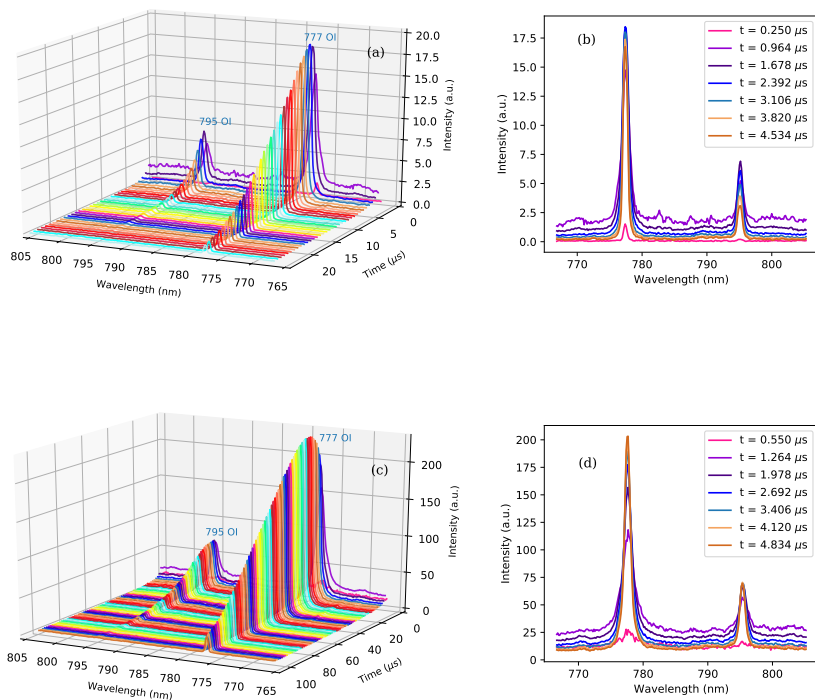


Figure 6.5: Time resolved R4 (770 - 805 nm) spectra of a meter long lightning-like discharge produced with the SI mode (panels (a), (b)) and LI mode (panels (c), (d)) of a Marx generator with 800 kV. The spectra were recorded at 1400000 fps (160 ns exposure time) with spectral and time resolutions of 0.34 nm and 0.714 μs , respectively. Triplets of oxygen neutrals (O I) at 777 nm and 795 nm are clearly visible.

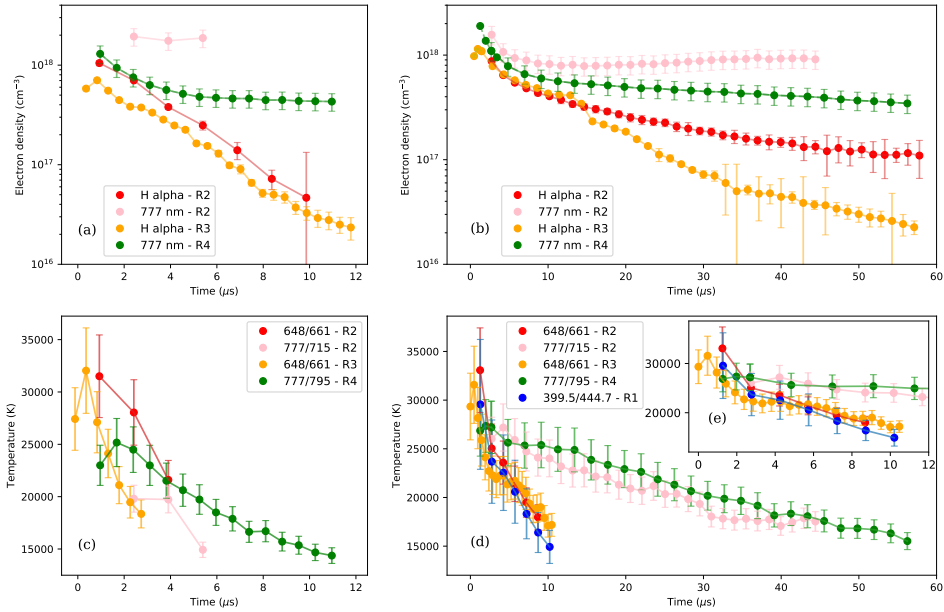


Figure 6.6: Electron densities and temperatures in a meter long lightning-like discharge produced with 800 kV in the SI (panels (a, c) and LI (panels (b, d) modes. Temperatures are quantified using different combinations of neutral (O I 777 nm and O I 795 nm with R4) and ion lines (NII 648 nm and NII 661 nm with R2, and N II 399.50 nm and N II 444.70 nm with R1). Electron densities are obtained from the Stark broadening of the 777 nm O I triplet and from the full width at half area (FWHA) of the H_{α} line at 656.30 nm. We have included for comparison electron densities and temperatures reported in a previous paper (see yellowish line) using grism R3 (645 nm - 665 nm) recorded at 2.1 Mfps for the same discharge and setup (Kieu et al., 2020). Note that the inset marked with (e) in panel (d) is a zoom out of the first time steps (up to 12 μ s) in panel (d).

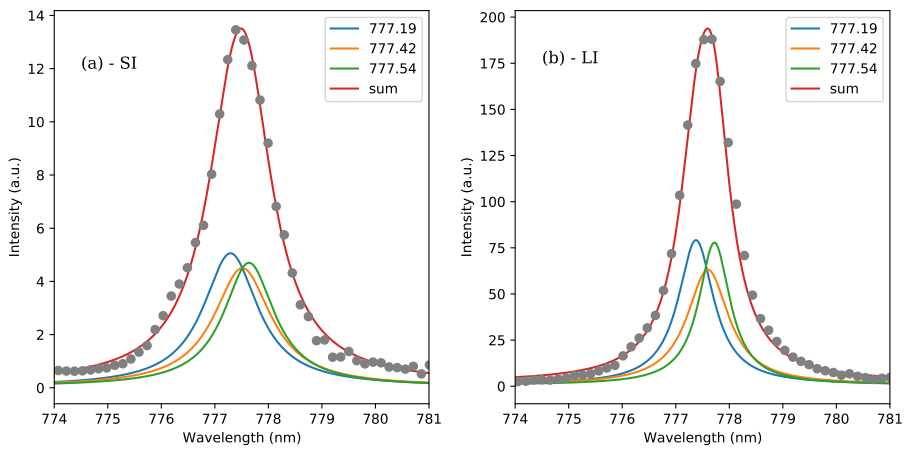


Figure 6.7: Lorentzian fit of the O I 777 nm triplet in the Switching (SI) mode (a) at $0.964 \mu\text{s}$ and in the Lightning (LI) mode (b) at $4.12 \mu\text{s}$ recorded with grism R4 (~ 0.34 nm spectral resolution). The red line is the triplet Lorentzian fit (sum) to the measured (grey dots) intensity of the O I 777 nm triplet. The blue, orange and green lines are the resulting single Lorentzians fits for each line component of the O I 777 nm triplet.

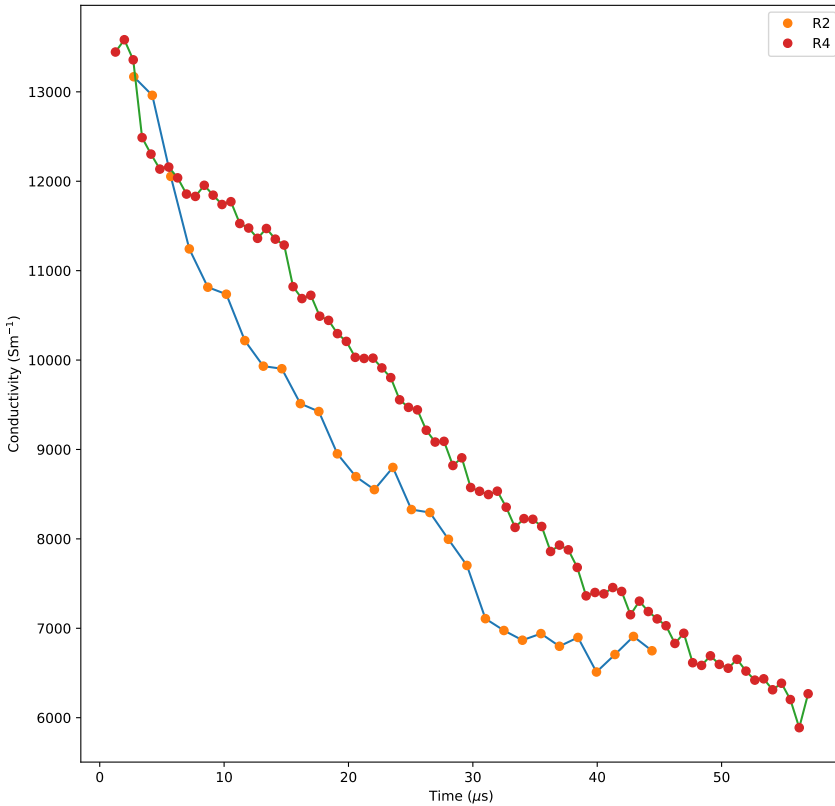


Figure 6.8: Time evolution of the electrical conductivity of a point in a heated ~ 1 m long lightning-like discharge channel produced with 800 kV in the LI mode. The electrical conductivity was computed using values of N_e (see Figure 6.6(b)) and T (see Figure 6.6(d)) derived from the FWHM of the O I 777.4 nm line, and the O I line ratios 777/715 and 777/795 obtained from spectra recorded with grisms R2 and R4, respectively. The solid lines are a guide for the eye.

Chapter 7

Conclusions

In this project, we succeeded in building a new spectroscopic system, GALIUS, to study transient spectroscopic features of artificial and natural lightning discharges. In total, GALIUS allows 22 set up configurations so that the system is flexible for measurements in the laboratory and in the field. The first advantage of GALIUS is the use of a slit which allows the system to control the spectral range of the measurements regardless of the locations of the discharges. With this we can fix a spectral range and calibrate the system in wavelength and flux. Another distinct feature of GALIUS is the possibility to combine four interchangeable VPHs which allows the system to record images from the near-ultraviolet to the near infrared (380 - 790 nm). GALIUS was able to record images in a wide spectral range which gave us many interesting details from different transient optical emissions of species in lightning-like discharges. However, the most interesting feature of GALIUS is the possibility to operate at 2.1 M fps (0.476 μ s time resolution). This allows the system to study the behavior of lightning-like discharges at sub microsecond time scale.

At its highest recording speed, 2.1 M fps, GALIUS recorded images of differ-

ent laboratory produced discharges: 4 cm sparks and 1 m sparks generated in Lightning and Switching Impulse modes at 800 kV. This is the first time that time-resolved lightning-like discharges have been explored in the sub-microsecond time regimes. The recorded spectra show the optical emissions of H_α and two singly ionized nitrogen lines (648 nm and 661 nm). We also saw emissions of doubly ionized nitrogen lines (645.41 nm and 646.70 nm) which were not previously detected. The optical emissions of neutral nitrogen atoms appeared at later times than ion lines. Our analysis of lightning-like spectra revealed high values of the electron density and temperature of $\sim 10^{18} \text{ cm}^{-3}$ and $\sim 32000 \text{ K}$, respectively. These values allows us to evaluate the overpressure, equilibrium and black body radiation in the heated channel. Our calculations show some evidences that suggest the possible disruption of the Boltzmann equilibrium right behind the shock front of the lightning-like channel recorded at sub- μs time regimes. Analysis of the self-absorption coefficients suggests that 1 m long discharges and short (4 cm long) discharges behave differently with respect to the optical thickness of the spectral lines.

GALIUS spectra recorded at 672000 fps in the near ultraviolet-blue from 380 nm to 450 nm showed evidence of optical molecular emissions such as: CN (violet bands), N_2 (Second Positive System), N_2^+ (First Negative System), C_2 (Swan band) and CO (Quintet and Ångström bands). Some of these emissions were found in time-averaged lightning spectra (before 1961) and time-resolved flash spectra (Salanave's spectra after 1961) but were not yet reported in time-resolved stroke spectra. These molecular optical emissions suggest the existence of mild temperature regions in lightning-like plasma channels that could allow molecular emissions that could also be due to the chemical activity of streamers surrounding a heated lightning channel.

In the visible and near-infrared spectral range (from 475 nm to 790 nm), GALIUS spectra show optical emissions due to various ionized and neutral species. For instance, the 500 nm line of nitrogen ions was the strongest emission in this spectral range in the early time. Ionic optical emissions disappear rapidly in about 10 μ s while neutral emissions, as that of oxygen atom at 777 nm, remains longer up to 100 μ s in the LI discharge mode. The quantifications of the electron density and temperature from the near ultraviolet-blue to the near infrared were performed with different methods and spectral lines: the electron density was calculated from the FWHA under the H_α line and the FWHM of the oxygen 777 nm line. The results derived from the FWHA of the H_α showed good agreement with previous electron density values found in triggered lightning and natural lightning. However, electron densities from FWHM of the oxygen 777 nm line remained high for a long time as their values (when obtained from FWHM) are considered to be only a first approximation. Temperatures were calculated from the ratio of four different pair of lines: 399.5 nm and 444.7 nm (N II); 648 nm and 661 nm (N II); 715 nm and 777 nm (O I), and 795 nm and 777 nm (O I). Temperatures derived from ionized species gave higher estimations but also decayed faster than temperatures calculated from neutral species.

Our spectral analysis of lightning-like discharges is still an on-going work. We are presently working on new studies aimed at determining the temperature and electron density in the heated channel from easy-to-make measurements of time dependence luminosities. This could be a new way to extract useful information from lightning spectra.

Finally, this project will continue (when possible) with analysis of real lightning spectra recorded with GALIUS in the near future in the post-covid era.

Bibliography

- Al-Tuwirqi, R., Al-Suliman, N., Khalil, A., and Gondal, M. (2012). New observation of the quintet states of co excited by glow discharge. *Molecular Physics*, 110(23):2951–2956.
- Bekefi, G. (1976). Principles of laser plasmas. *New York: John Wiley and Sons*.
- Camacho, J., Poyato, J., Diaz, L., and Santos, M. (2007). Optical emission studies of nitrogen plasma generated by IR CO₂ laser pulses. *Journal of Physics B: Atomic, Molecular and Optical Physics*, 40(24):4573.
- Carbone, E., D’Isa, F., Hecimovic, A., and Fantz, U. (2020). Analysis of the C₂ Swan bands as a thermometric probe in CO₂ microwave plasmas. *Plasma Sources Science and Technology*, 29(5):055003.
- Cen, J., Yuan, P., Xue, S., and Wang, X. (2015). Spectral characteristics of lightning dart leader propagating in long path. *Atmospheric Research*, 164:95–98.
- Cho, M. and Rycroft, M. J. (1998). Computer simulation of the electric field structure and optical emission from cloud-top to the ionosphere. *Journal of Atmospheric and Solar-Terrestrial Physics*, 60(7-9):871–888.

- Christian, H. J., Blakeslee, R. J., Boccippio, D. J., Boeck, W. L., Buechler, D. E., Driscoll, K. T., Goodman, S. J., Hall, J. M., Koshak, W. J., Mach, D. M., et al. (2003). Global frequency and distribution of lightning as observed from space by the optical transient detector. *Journal of Geophysical Research: Atmospheres*, 108(D1):ACL-4.
- Crispim, L. W. S., Peters, F. C., Amorim, J., Hallak, P. H., and Ballester, M. Y. (2021). On the CN production through a spark-plug discharge in air-CO₂ mixture. *Combustion and Flame*, 226:156-162.
- Cummer, S. A., Frey, H. U., Mende, S. B., Hsu, R.-R., Su, H.-T., Chen, A. B., Fukunishi, H., and Takahashi, Y. (2006). Simultaneous radio and satellite optical measurements of high-altitude sprite current and lightning continuing current. *Journal of Geophysical Research: Space Physics*, 111(A10).
- Cummer, S. A. and Füllekrug, M. (2001). Unusually intense continuing current in lightning produces delayed mesospheric breakdown. *Geophysical Research Letters*, 28(3):495-498.
- Czech, T., Sobczyk, A. T., Jaworek, A., and Krupa, A. (2012). Corona and back discharges in flue-gas simulating mixture. *Journal of Electrostatics*, 70(3):269-284.
- Czech, T., Sobczyk, A. T., Jaworek, A., Krupa, A., and Rajch, E. (2013). Studies of corona and back discharges in carbon dioxide. *The European Physical Journal D*, 67(1):23.
- Dong, M., Chan, G. C. Y., Mao, X., Gonzalez, J. J., Lu, J., and Russo, R. E. (2014). Elucidation of C₂ and CN formation mechanisms in laser-induced plas-

- mas through correlation analysis of carbon isotopic ratio. *Spectrochimica Acta Part B: Atomic Spectroscopy*, 100:62–69.
- Dufay, J. (1926). Spectres des éclairs. *Compt. Rend.*, 182:1331–1333.
- Dufay, M. (1949). Recherches sur les spectres des éclairs, deuxième partie: Etude du spectre dans les régions violette et ultraviolette. *Ann. Geophys.*, 5(4):255–263.
- Dwyer, J. R. and Uman, M. A. (2014). The physics of lightning. *Physics Reports*, 534(4):147–241.
- Efron, B. and Tibshirani, R. (1985). The bootstrap method for assessing statistical accuracy. *Behaviormetrika*, 12(17):1–35.
- El Sherbini, A. M., El Sherbini, T. M., Hegazy, H., Cristoforetti, G., Legnaioli, S., Palleschi, V., Pardini, L., Salvetti, A., and Tognoni, E. (2005). Evaluation of self-absorption coefficients of aluminum emission lines in laser-induced breakdown spectroscopy measurements. *Spectrochimica Acta Part B: Atomic Spectroscopy*, 60(12):1573–1579.
- Fantz, U. (2006). Basics of plasma spectroscopy. *Plasma sources science and technology*, 15(4):S137.
- Fisher, R. J., Schnetzer, G. H., Thottappillil, R., Rakov, V. A., Uman, M. A., and Goldberg, J. D. (1993). Parameters of triggered-lightning flashes in florida and alabama. *Journal of Geophysical Research: Atmospheres*, 98(D12):22887–22902.
- Fox, P. (1903). The spectrum of lightning. *The Astrophysical Journal*, 18:294.

- Fuquay, D. M., Baughman, R. G., Taylor, A. R., and Hawe, R. G. (1967). Characteristics of seven lightning discharges that caused forest fires. *Journal of Geophysical Research*, 72(24):6371–6373.
- Gigosos, M. A., González, M. A., and Cardenoso, V. (2003). Computer simulated balmer-alpha,-beta and-gamma stark line profiles for non-equilibrium plasmas diagnostics. *Spectrochimica Acta Part B: Atomic Spectroscopy*, 58(8):1489–1504.
- Gilmore, F. R., Laher, R. R., and Espy, P. J. (1992). Franck-Condon Factors, r-Centroids, Electronic Transition Moments, and Einstein Coefficients for Many Nitrogen and Oxygen Band Systems. *J. Phys. Chem. Ref. Data*, 21:1005.
- Godin, D. and Trépanier, J. Y. (2004). A robust and efficient method for the computation of equilibrium composition in gaseous mixtures. *Plasma chemistry and plasma processing*, 24(3):447–473.
- Gordillo-Vázquez, F. J., Luque, A., and Simek, M. (2012). Near infrared and ultraviolet spectra of tles. *Journal of Geophysical Research: Space Physics*, 117(A5).
- Gordillo-Vázquez, F. J., Passas, V. M., Luque, A., Sánchez, J., Velde, O. A., and Montanyá, J. (2018). High spectral resolution spectroscopy of sprites: A natural probe of the mesosphere. *Journal of Geophysical Research: Atmospheres*, 123(4):2336–2346.
- Gordillo-Vázquez, F. J. and Pérez-Invernón, F. J. (2021). A review of the impact of transient luminous events on the atmospheric chemistry: Past, present, and future. *Atmospheric Research*, page 105432.

- Gordillo-Vázquez, F. J., Pérez-Invernón, F. J., Huntrieser, H., and Smith, A. K. (2019). Comparison of six lightning parameterizations in CAM5 and the impact on global atmospheric chemistry. *Earth and Space Science*, 6(12):2317–2346.
- Griem, H. R. (1964). Plasma spectroscopy. *New York: McGraw-Hill*, 47.
- Griem, H. R. and Barr, W. L. (1975). Spectral line broadening by plasmas. *IEEE Transactions on Plasma Science*, 3(4):227–227.
- Guo, Y.-X., Yuan, P., Shen, X.-Z., and Wang, J. (2009). The electrical conductivity of a cloud-to-ground lightning discharge channel. *Physica Scripta*, 80(3):035901.
- Hampton, D. L., Heavner, M. J., Wescott, E. M., and Sentman, D. D. (1996). Optical spectral characteristics of sprites. *Geophys. Res. Lett.*, 23:89.
- Hornkohl, J. O., Fleischmann, J. P., Surnick, D. M., Witte, M. J., Swafford, L. D., Woods, A. C., and Parigger, C. G. (2014). Emission spectroscopy of nitric oxide in laser-induced plasma. In *Journal of Physics: Conference Series*, volume 548, page 012040. IOP Publishing.
- Israel, H. and Wurm, K. (1941). Das blitzspektrum. *Naturwissenschaften*, 52:778–779.
- Kadochnikov, I. N. and Arsentiev, I. V. (2018). Kinetics of nonequilibrium processes in air plasma formed behind shock waves: state-to-state consideration. *Journal of Physics D: Applied Physics*, 51(37):374001.
- Kanmae, T., Stenbaek-Nielsen, H. C., and McHarg, M. G. (2007). Altitude resolved sprite spectra with 3 ms temporal resolution. *Geophys. Res. Lett.*, 34:L07810.

- Kieu, T. N., Gordillo-Vázquez, F. J., Passas, V. M., Sánchez, J., and Pérez-Invernón, F. J. (2021). High-speed spectroscopy of lightning-like discharges: evidence of molecular optical emissions. *Journal of Geophysical Research: Atmospheres*, 126(11):e2021JD035016.
- Kieu, T. N., Gordillo-Vázquez, F. J., Passas, V. M., Sánchez, J., Pérez-Invernón, F. J., Luque, A., Montanyá, J., and Christian, H. (2020). Sub-microsecond spectroscopy of lightning-like discharges: exploring new time regimes. *Geophysical Research Letters*, 47(15):e2020GL088755.
- Kolmašová, I., Santolík, O., Kašpar, P., Popek, M., Pizzuti, A., Spurný, P., Borovička, J., Mlynarczyk, J., Manninen, J., Macotela, E. L., et al. (2021). First observations of elves and their causative very strong lightning discharges in an unusual small-scale continental spring-time thunderstorm. *Journal of Geophysical Research: Atmospheres*, 126(1):e2020JD032825.
- Kramida, A., Ralchenko, Y., Reader, J., and Team, N. (2015). Atomic spectra database. *NIST Atomic Spectra Database*, page 20899.
- Krider, E. P. (1965a). The design and testing of a photoelectric photometer for selected lines in the spectrum of lightning. *MS thesis*.
- Krider, E. P. (1965b). Time-resolved spectral emissions from individual return strokes in lightning discharges. *Journal of Geophysical Research*, 70(10):2459–2460.
- Krider, E. P. (1974). The relative light intensity produced by a lightning stepped leader. *Journal of Geophysical Research*, 79(30):4542–4544.
- Levine, J. S., Hughes, R. E., Chameides, W. L., and Howell, W. E. (1979). N₂O

- and CO production by electric discharge: Atmospheric implications. *Geophysical Research Letters*, 6(7):557–559.
- Little, C. E. and Browne, P. G. (1987). Origin of the high-pressure bands of C₂. *Chemical Physics Letters*, 134(6):560–564.
- Luque, A. and Gordillo-Vázquez, F. J. (2011). Modeling and analysis of N₂(B³Π_g) and N₂(C³Π_u) vibrational distributions in sprites. *J. Geophys. Res - Space Phys.*, 116(A2).
- Luque, A., Gordillo-Vázquez, F. J., Li, D., Malagón-Romero, A., Pérez-Invernón, F. J., Schmalzried, A., Soler, S., Chanrion, O., Heumesser, M., Neubert, T., et al. (2020). Modeling lightning observations from space-based platforms (cloudscat. jl 1.0). *Geoscientific Model Development*, 13(11):5549–5566.
- McEachron, K. B. and Hagenguth, J. H. (1942). Effect of lightning on thin metal surfaces. *Transactions of the American Institute of Electrical Engineers*, 61(8):559–564.
- Murray, L. T. (2016). Lightning NO_x and impacts on air quality. *Current Pollution Reports*, 2(2):115–133.
- Newman, M. M., Stahmann, J. R., Robb, J. D., Lewis, E. A., Martin, S. G., and Zinn, S. V. (1967). Triggered lightning strokes at very close range. *Journal of Geophysical Research*, 72(18):4761–4764.
- Nikiforov, A. Y., Leys, C., Gonzalez, M. A., and Walsh, J. L. (2015). Electron density measurement in atmospheric pressure plasma jets: Stark broadening of hydrogenated and non-hydrogenated lines. *Plasma Sources Science and Technology*, 24(3):034001.

- Offroy, M., Farges, T., Kuo, C. L., Chen, A. B.-C., Hsu, R.-R., Su, H.-T., Takahashi, Y., Mende, S. B., and Frey, H. U. (2015). Temporal and radiometric statistics on lightning flashes observed from space with the isual spectrophotometer. *Journal of Geophysical Research: Atmospheres*, 120(15):7586–7598.
- Orville, R. E. (1966a). High-speed, time-resolved spectrum of a lightning stroke. *Science*, 151(3709):451–452.
- Orville, R. E. (1966b). A spectral study of lightning return strokes. *Unpublished doc-477 total dissertation, PhD thesis, Univ. of Arizona, Tucson, Ariz*, 478.
- Orville, R. E. (1968a). A high-speed time-resolved spectroscopic study of the lightning return stroke: Part i. a qualitative analysis. *Journal of the Atmospheric Sciences*, 25(5):827–838.
- Orville, R. E. (1968b). A high-speed time-resolved spectroscopic study of the lightning return stroke: Part ii. a quantitative analysis. *Journal of the Atmospheric Sciences*, 25(5):839–851.
- Orville, R. E. (1968c). A high-speed time-resolved spectroscopic study of the lightning return stroke. part iii. a time-dependent model. *Journal of Atmospheric Sciences*, 25(5):852–856.
- Orville, R. E. (1968d). Spectrum of the lightning stepped leader. *Journal of Geophysical Research*, 73(22):6999–7008.
- Orville, R. E. (1975). Spectrum of the lightning dart leader. *Journal of Atmospheric Sciences*, 32(9):1829–1837.
- Orville, R. E. (1977). Lightning spectroscopy. *Lightning: Physics of Lightning, Volume 1 & 2*, 1:281.

- Orville, R. E. and Uman, M. A. (1965). The optical continuum of lightning. *Journal of Geophysical Research*, 70(2):279–282.
- Orville, R. E., Uman, M. A., and Sletten, A. M. (1967). Temperature and electron density in long air sparks. *Journal of Applied Physics*, 38(2):895–896.
- Parigger, C. G., Swafford, L. D., Surmick, D. M., Witte, M. J., Woods, A. C., and Gautam, G. (2014). Hydrogen alpha self-absorption effects in laser-induced air plasma. In *Journal of physics: Conference series*, volume 548, page 012043. IOP Publishing.
- Parra-Rojas, F. C., Luque, A., and Gordillo-Vázquez, F. J. (2015). Chemical and thermal impact of sprite streamers in the Earth mesosphere. *Journal of Geophysical Research: Space Physics*.
- Parra-Rojas, F. C., Passas, V. M., Carrasco, E., Luque, A., Tanarro, I., Simek, M., and Gordillo-Vázquez, F. J. (2013). Spectroscopic diagnosis of laboratory air plasmas as a benchmark for spectral diagnosis of TLEs. *Journal of Geophysical Research: Space Physics*, 118:4649–4661.
- Parra-Rojas, F. C., Passas, V. M., Carrasco, E., Luque, A., Tanarro, I., Simek, M., and Gordillo-Vázquez, F. J. (2013). Spectroscopic diagnostics of laboratory air plasmas as a benchmark for spectral rotational (gas) temperature determination in tles. *Journal of Geophysical Research: Space Physics*, 118(7):4649–4661.
- Passas, V. M., del Río, J. S., Luque, A., and Gordillo-Vázquez, F. J. (2014). Transient upper atmospheric plasmas: Sprites and halos. *IEEE Transactions on Plasma Science*, 42(10):2664–2665.
- Passas, V. M., Madiedo, J. M., and Gordillo-Vázquez, F. (2016a). High resolution spectroscopy of an orionid meteor from 700 to 800 nm. *Icarus*, 266:134–141.

- Passas, V. M., Sánchez, J., Kieu, T. N., Sánchez-Blanco, E., and Gordillo-Vázquez, F. J. (2019). Galius: an ultrafast imaging spectrograph for the study of lightning. *Applied optics*, 58(29):8002–8006.
- Passas, V. M., Sánchez, J., Sánchez-Blanco, E., Luque, A., and Gordillo-Vázquez, F. J. (2016b). Grassp: a spectrograph for the study of transient luminous events. *Applied optics*, 55(23):6436–6442.
- Pérez-Invernón, F. J., Luque, A., and Gordillo-Vázquez, F. J. (2018). Modeling the chemical impact and the optical emissions produced by lightning-induced electromagnetic fields in the upper atmosphere: the case of halos and elves triggered by different lightning discharges. *Journal of Geophysical Research: Atmospheres*, 123(14):7615–7641.
- Pickering, E. C. (1901). Spectrum of lightning. *Astronomische Nachrichten*, 157:207.
- Prueitt, M. L. (1963). The excitation temperature of lightning. *Journal of Geophysical Research*, 68(3):803–811.
- Raizer, Y. P. (1991). *Gas discharge physics. Fizika gazovogo razryada*. Springer, Berlin.
- Rakov, V. A. and Uman, M. A. (2003). *Lightning: physics and effects*. Cambridge university press.
- Ripoll, J.-F., Zinn, J., Jeffery, C. A., and Colestock, P. L. (2014). On the dynamics of hot air plasmas related to lightning discharges: 1. gas dynamics. *Journal of Geophysical Research: Atmospheres*, 119(15):9196–9217.

- Salanave, L. E. (1961). The optical spectrum of lightning. *Science*, 134(3488):1395–1399.
- Salanave, L. E. (1971). Lightning spectroscopy—photographic techniques. 2. *Applied optics*, 10(1):206–207.
- Salanave, L. E., Orville, R. E., and Richards, C. N. (1962). Slitless spectra of lightning in the region from 3850 to 6900 angstroms. *Journal of Geophysical Research*, 67(5):1877–1884.
- Schumann, U. and Huntrieser, H. (2007). The global lightning-induced nitrogen oxides source. *Atmospheric Chemistry and Physics*, 7(14):3823–3907.
- Slipher, V. M. (1917). The spectrum of lightning. *Lowell Observatory Bulletin*, 3:55–58.
- Soler, S., Pérez-Invernón, F. J., Gordillo-Vázquez, F. J., Luque, A., Li, D., Malagón-Romero, A., Neubert, T., Chanrion, O., Reglero, V., Navarro-Gonzalez, J., et al. (2020). Blue optical observations of narrow bipolar events by asim suggest corona streamer activity in thunderstorms. *Journal of Geophysical Research: Atmospheres*, 125(16):e2020JD032708.
- Teulet, P., Gonzalez, J. J., Mercado-Cabrera, A., Cressault, Y., and Gleizes, A. (2009). One-dimensional hydro-kinetic modelling of the decaying arc in air-pa66–copper mixtures: I. chemical kinetics, thermodynamics, transport and radiative properties. *Journal of Physics D: Applied Physics*, 42(17):175201.
- Tran, D. M. and Rakov, V. A. (2015). When does the lightning attachment process actually begin? *Journal of Geophysical Research: Atmospheres*, 120(14):6922–6936.

- Uman, M. A. (1963). The continuum spectrum of lightning. *Journal of Atmospheric and Terrestrial Physics*, 25(5):287–295.
- Uman, M. A. (1964). The peak temperature of lightning. *Journal of Atmospheric and Terrestrial Physics*, 26(1):123–128.
- Uman, M. A. (1969a). Determination of lightning temperature. *Journal of Geophysical Research*, 74(4):949–957.
- Uman, M. A. (1969b). Lightning, 264 pp. *McGraw-Hill, New York. Uman, MA, and DK McLain (1969), Magnetic field of lightning? return stroke, J. Geophys. Res*, 74(28):6899–6910.
- Uman, M. A. (2001). *The lightning discharge*. Courier Corporation.
- Uman, M. A. and Orville, R. E. (1964). Electron density measurement in lightning from stark-broadening of $h\alpha$. *Journal of Geophysical Research*, 69(24):5151–5154.
- Uman, M. A. and Orville, R. E. (1965). The opacity of lightning. *Journal of Geophysical Research*, 70(22):5491–5497.
- Uman, M. A., Orville, R. E., and Salanave, L. E. (1964). The density, pressure, and particle distribution in a lightning stroke near peak temperature. *Journal of the Atmospheric Sciences*, 21(3):306–310.
- Walker, T. D. (2015). *A 21st Century Investigation of the lightning spectrum*. University of Alabama in Huntsville.
- Walker, T. D. and Christian, H. J. (2017). Triggered lightning spectroscopy: Part 1. a qualitative analysis. *Journal of Geophysical Research: Atmospheres*, 122(15):8000–8011.

- Walker, T. D. and Christian, H. J. (2019). Triggered lightning spectroscopy: 2. a quantitative analysis. *Journal of Geophysical Research: Atmospheres*, 124(7):3930–3942.
- Wallace, L. (1960). Note on the spectrum of lightning in the region 3670 to 4280 a. *Journal of Geophysical Research*, 65(4):1211–1214.
- Wallace, L. (1964). The spectrum of lightning. *The Astrophysical Journal*, 139:994.
- Wang, X., Yuan, P., Cen, J., Liu, J., and Li, Y. (2014). The channel radius and energy of cloud-to-ground lightning discharge plasma with multiple return strokes. *Physics of Plasmas*, 21(3):033503.
- Warner, T. A., Orville, R. E., Marshall, J. L., and Huggins, K. (2011). Spectral (600–1050 nm) time exposures (99.6 μ s) of a lightning stepped leader. *Journal of Geophysical Research: Atmospheres*, 116(D12).
- Zahn, M., Forster, E. O., Kelley, E. F., and Hebner Jr, R. E. (1982). Hydrodynamic shock wave propagation after electrical breakdown. *Journal of Electrostatics*, 12:535–546.
- Zhang, N., Yuan, P., ting An, T., Zhang, M., and rong Chen, R. (2020). The conductivity and propagation property of lightning leader tip. *Atmospheric Research*, 245:105099.
- Zhivlyuk, Y. N. and Mandel'shtam, S. L. (1961). On the temperature of lightning and force of thunder. *Soviet Physics JETP*, 13(2):338.

Declaration

I herewith declare that I produced this thesis without the prohibited assistance of third parties and without making use of aids other than those specified; notions taken over directly or indirectly from other sources have been identified as such. This thesis has not previously been presented in identical or similar form to any other Spanish or foreign examination board. The thesis work was conducted from 2017 to 2021 under the supervision of Dr. Francisco J. Gordillo Vázquez and Dr. Alejandro Luque Estepa.

Granada, July 17th, 2021

Curriculum Vitae

Personal information

Full name : Thi Ny Kieu

Date of birth : 09th September 1987

Place of birth : Binh Thuan, Viet Nam

Education and employment

2017-2021 : Ph.D. student at Instituto de Astrofísica de Andalucía (IAA-CSIC)
University of Granada, Granada, Spain
Dissertation: “*Ultra-fast time-resolved spectroscopy for lightning-like discharges with GALIUS*”

2015-2017 : M. Sc. degree in Physique, Rayonnement, énergie, spectroscopies Parcours SPACE
Aix - Marseille Université, *Marseille, France*
Master thesis: “Analysis for white dwarfs spectra”

2010-2013 : M. Sc. degree in Theoretical and Computing Physics
Viet Nam National University, University of natural sciences
Ho Chi Minh City, Viet Nam
Master thesis: “The independent particle models of atom”

2009-2013 : High school physics teacher
Ho Chi Minh City, Viet Nam

2005-2009 : Bachelor degree in Physics for Education
Ho Chi Minh City University of Education
Ho Chi Minh City, Viet Nam

Scholarships

09/2015 - 07/2017 A†Midex SPaCE - Aix Marseille University

11/2017 – 05/2021 Marie Skłodowska - Curie Grant – H2020

Short stays

04 - 10/2019: Dena Desarrollos SL, Tarrasa, Barcelona, Spain.

Project: “Working with high voltage laboratory discharge spectroscopy”

Training schools

24/06 - 05/07/2019 2nd SAINT Summer School, Toulouse, France.

21/01 - 01/02/2019 2nd SAINT Winter School, Amsterdam, Netherland.

02/06 - 13/06/2018 1st SAINT Summer School, Barcelona, Spain.

15/01 - 19/01/2018 1st SAINT Winter School, Copenhagen, Denmark.

03/08 - 15/08/2014 The 20nd Vietnam school of physics: particle physics, Astro-particle physics and cosmology, Qui Nhon, Viet Nam.

18/07 - 25/07/2014 The 1st Hue Summer School in Particle and Astro-particle Physics, Hue, Viet Nam.

23/07 - 04/08/2012 The 18th Vietnam school of physics: particle physics, physics, Astro-physics and cosmology, Qui Nhon, Viet Nam.

Publications

Journal papers

1. **Kieu, T. N.**, Gordillo-Vázquez, F.J., Passas, M., Sánchez, J., Pérez - Invernón, **2021**. ‘High-speed spectroscopy of lightning-like discharges: evidence of molecular optical emissions’. *Journal of Geophysical Research: Atmospheres*. 126(11), e2021JD035016
2. **Kieu, T. N.**, Gordillo-Vázquez, F.J., Passas, M., Sánchez, J., Pérez-Invernón, F.J., Luque, A., Montanyá, J. and Christian, H., **2020**. ‘Sub-microsecond spectroscopy of lightning-like discharges: Exploring new time regimes’. *Geophysical Research Letters*, 47(15), p.e2020GL088755
3. Passas-Varo, M., Sánchez, J., **Kieu, T.N.**, Sánchez-Blanco, E. and Gordillo-Vázquez, F.J., **2019**. ‘GALIUS: an ultrafast imaging spectrograph for the study of lightning’. *Applied Optics*, 58(29), pp.8002-8006.
4. Rosato, J., **Kieu, T. N.**, Meireni, M., Koubiti, M., Marandet, Y., Stamm, R., Kovačević-Dojčinović, J., Dimitrijević, M.S., Popović, L.Č. and Simić, Z., **2019**, July. ‘A new analysis of spectral line shapes in white dwarf atmospheres’. In *Journal of Physics: Conference Series* (Vol. 1289, No. 1, p. 012006). IOP Publishing.
5. Rosato, J., **Kieu, T. N.**, Meireni, M., Sheeba, R., Koubiti, M., Marandet, Y., Stamm, R., Verhaegh, K., Duval, B., TCV team and MST1 team, **2018**. ‘Stark broadening of Balmer lines with low and moderate quantum number in dense divertor plasmas’. *Contributions to Plasma Physics*, 58(6-8), pp.578-582
6. **Kieu, T. N.**, Joël and Stamm, Roland and Kovačević-Dojčinović, Jelena and Dimitrijević, Milan S and Popović, Luka Č and Simić, Zoran, **2017**. ‘A New analysis of Stark and Zeeman effects on hydrogen lines in magnetized DA white dwarfs’. *Atoms*, 5(4), p.44.
7. Rosato, Joël and **Kieu, N.** and Hannachi, Ibtissem and Koubiti, Mohammed and Marandet, Yannick and Stamm, Roland and Dimitrijević, Milan S and Simić, Zoran, **2017**. ‘Stark-Zeeman Line Shape Modeling for Magnetic White Dwarf and Tokamak Edge Plasmas: Common Challenges’. *Atoms*, 5(4), p.36

Conference proceedings

1. **Kieu, T. N.**, Gordillo - Vázquez, F.J., Passas, M., Sánchez, J., **2018**. ‘*Preliminary GALIUS Spectra of sparks produced by a small electrostatic generator*’. The 16th International Conference on Atmospheric electricity (ICAE 2018), *Nara, Japan*. **Poster**.
2. **Kieu, T. N.**, Gordillo - Vázquez, F.J., Passas, M., Sánchez, J., **2018**. ‘*A quantitative analysis of high-speed time-resolved spectroscopy of sparks recorded by GALIUS*’. The 45th Annual European Meeting on Atmospheric Studies by Optical Methods, *Kiruna, Sweden*. **Poster**
3. **Kieu, T. N.**, Gordillo - Vázquez, F.J., Passas, M., Sánchez, J., **2019**. ‘*Ultra-high speed lightning and spark spectroscopy with GALIUS*’. EGU General Assembly 2019, *Vienna, Austria*. **Poster**
4. **Kieu, T. N.**, Gordillo - Vázquez, F.J., Passas, M., Sánchez, J., **2019**. ‘*Ultra-high speed spectroscopy of lightning-like discharges with GALIUS*’. AGU Fall meeting 2019, *San Francisco, USA*. **eLightning-Poster**

Presentations

1. **Kieu, T. N.**, Gordillo - Vázquez, F.J., Passas, M., Sánchez, J., (**02/06 - 13/06/2018**). ‘*Preliminary analyses of GALIUS spark spectra*’. 1st SAINT Summer School, *Barcelona, Spain* (Oral + Poster).
2. **Kieu, T. N.**, Gordillo - Vázquez, F.J., Passas, M., Sánchez, J., (**21/01 - 01/02/2019**). ‘*Ultra-high speed lightning and spark spectroscopy with GALIUS*’. 2nd SAINT Winter School, *Amsterdam, Netherland*, (Oral + Poster).
3. **Kieu, T. N.**, Gordillo - Vázquez, F.J., Passas, M., Sánchez, J., (**24/06 - 5/07/2019**). ‘*Ultra-high speed spectroscopy of lightning-like discharges with GALIUS*’. 2nd SAINT Summer School, *Toulouse, France*, (Oral + Poster).
4. **Kieu, T. N.**, Gordillo - Vázquez, F.J., Passas, M., Sánchez, J., (**22/10/2020**). ‘*Ultra-high speed spectroscopy of lightning-like discharges with GALIUS*’. SAINT meeting.